

UCLA

UCLA Electronic Theses and Dissertations

Title

Exploring Disease-Driven Biomarkers for Radio-Theranostic Targeting in Cancer

Permalink

<https://escholarship.org/uc/item/51c9j8t7>

Author

Storey, Claire Madeline

Publication Date

2024

Peer reviewed|Thesis/dissertation

UNIVERSITY OF CALIFORNIA

Los Angeles

Exploring Disease-Driven Biomarkers for Radio-Theranostic Targeting in Cancer

A dissertation submitted in satisfaction of the
requirements for the degree Doctor of Philosophy
in Molecular and Medical Pharmacology

by

Claire Madeline Storey

2025

© Copyright by
Claire Madeline Storey
2025

ABSTRACT OF THE DISSERTATION

Exploring Disease-Driven Biomarkers for Radio-Theranostic Targeting in Cancer

by

Claire Madeline Storey

Doctor of Philosophy in Molecular and Medical Pharmacology

University of California, Los Angeles, 2024

Professor H. David Ulmert, Chair

The field of radioimmunotheranostics (RIT) has emerged as a powerful strategy for targeted cancer treatment, combining the specificity of monoclonal antibodies with the cytotoxic effects of radionuclides. By leveraging tumor-associated antigens, RIT enables precise imaging, targeted radiotherapy, and immune modulation, offering a promising approach for overcoming therapeutic resistance in aggressive cancers. However, a key component to the success of RIT is in finding disease-driven biomarkers that are representative of the disease state and underlying signaling mechanisms. In prostate cancer (PCa), androgen receptor (AR) signaling remains a critical driver of disease progression and resistance. [⁸⁹Zr]11B6-PET, a novel imaging modality targeting AR-dependent, prostate-specific protein human kallikrein 2 (hK2), effectively assesses AR pathway activation and therapy-induced changes in PCa mouse models. Additionally, Leucine-rich repeat-containing protein 15 (LRRC15) has been identified as a key biomarker and therapeutic target in aggressive tumors. The humanized monoclonal antibody DUNP19, radiolabeled with Lutetium-177, enables precise imaging and radiotherapy of LRRC15-expressing tumors and cancer-associated fibroblasts (CAFs), leading to tumor suppression and immune reprogramming. Finally, the key pro-tumorigenic cytokine transforming growth factor beta, or TGF β , upregulates LRRC15 expression, contributing to immune evasion and metastasis. Integrative functional and genomic

analyses identify key regulators—MMP2, SPARC, TGF β R2, and WNT5B—governing TGF β -induced LRRC15 expression and immunotherapy resistance. These findings highlight the potential of RIT-based AR and LRRC15-targeted strategies in advancing precision oncology and improving patient outcomes.

The dissertation of Claire Madeline Storey is approved.

Harvey R. Herschman

Robert E. Reiter

Robert D. Damoiseaux

Hans David S. Ulmert, Committee Chair

University of California, Los Angeles

2025

Dedicated to my husband, family, friends, and my dog, who loyally sat by my side as I wrote.

TABLE OF CONTENTS

Abstract of Dissertation.....	ii
Committee Page.....	ix
Dedication Page.....	v
List of Figures and Tables.....	ix
Curriculum Vitae.....	x
Chapter 1. Introduction.....	1
1.1. Antibodies.....	1
1.2. Biomarkers and Therapeutic Targets.....	15
1.3. Technologies.....	21
1.4. Conclusion.....	28
1.5. References.....	29
Chapter 2. KLK2 as a radio-immunotherapeutic target in prostate cancer	38
2.1. Introduction.....	39
2.2. Materials and Methods	41
2.3. Changes in AR and AR-driven prostate cancer biomarkers in response to EBRT.....	45
2.4. EBRT increases AR activity in prostate cancer <i>in vivo</i>	48
2.5. [⁸⁹ Zr]11B6 uptake is an indicator of EBRT-induced AR activity.....	48
2.6. EBRT-induced AR activity can be monitored by [⁸⁹ Zr]11B6 PET/CT imaging	49
2.7. Discussion.....	51
2.8. References.....	55
Chapter 3. LRRC15 as a radio-immunotherapeutic target.....	60
3.1. Introduction.....	61
3.2. Materials and Methods	63

3.3. LRRC15 can be targeted utilizing the mAb DUNP19.....	76
3.4. DUNP19 <i>in vivo</i> PET can monitor tumor-associated LRRC15 expression.....	79
3.5. [¹⁷⁷ Lu]-DUNP19 exhibits a favorable biodistribution.....	81
3.6. [¹⁷⁷ Lu]-DUNP19 radioimmunotherapy (RIT) of aggressive osteosarcoma.....	83
3.7. [¹⁷⁷ Lu]-DUNP19 is effective across tumors with varying LRRC15 expression	88
3.8. LRRC15-targeted RIT depletes TGFβ-driven signature in tumors	90
3.9. Discussion	96
3.10. References	101
3.11. Supplementary Figures.....	105
Chapter 4. Uncovering Key Regulatory Elements of the TGFβ-LRRC15 Axis in Cancer with	
Single-Cell RNA Sequencing and Functional Molecular Screening	119
4.1. Introduction	120
4.2. Materials and Methods	122
4.3. LRRC15 expression is inducible by TGFβ	129
4.4. Single cell sequencing of TGFβ-inducible cell lines reveals distinct LRRC15-related	
signatures	134
4.5. Network analysis of TGFβ-responsive transcriptional signatures.....	137
4.6. Integrated high-throughput drug screening and scRNAseq data reveals converging	
molecular pathways involved in LRRC15's regulation	140
4.7. TGFβ-induced LRRC15 expression can be modulated by siRNA knockdown of candidate	
genes.....	145
4.8. Activators of LRRC15 expression correlate to immunotherapy response and tumor	
progression.....	147
4.9. Discussion	151
4.10. References	157

4.11. Supplementary Figures..... 163

Chapter 5. Conclusion..... 176

5.1. Future Directions 176

5.2. References..... 179

LIST OF FIGURES AND TABLES

Figure 1.1. Dissertation Overview.....	29
Figure 2.1. AR activity and gene expression after EBRT in LNCaP-AR and 22Rv1 xenografts.....	47
Figure 2.2. EBRT-induced transcriptomic changes in LNCaP-AR xenografts.....	48
Figure 2.3. [⁸⁹ Zr]11B6 localizes to PCa after irradiation.....	49
Figure 2.4. EBRT treatment of Hi- <i>Myc</i> x Pb- <i>KLK2</i> and Pb- <i>KLK2</i> mice.....	50
Figure 2.5. AR activity increase following EBRT visualized by [⁸⁹ Zr]11B6-PET/CT.....	51
Figure 3.1. <i>In vitro</i> evaluation of DUNP19's binding profile to LRRC15.....	78
Figure 3.2. Specificity and biodistribution of DUNP19 in multiple mouse models with LRRC15 expressing tumors.....	80
Figure 3.3. Evaluation of [¹⁷⁷ Lu]-DUNP19 therapy and monitoring in HuO9 osteosarcoma tumors.....	86
Figure 3.4. Therapeutic efficacy of [¹⁷⁷ Lu]-DUNP19 in LRRC15-expressing human xenograft models.....	89
Figure 3.5. [¹⁷⁷ Lu]-DUNP19 induced radioimmunotherapy signatures in LRRC15+ cancer cells.....	92
Figure 3.6. [¹⁷⁷ Lu]-DUNP19 therapy eradicates a LRRC15+ TGFβ signature associated with immunotherapy resistance.....	95
Supplemental Figure 3.1. DUNP19 binds to human and murine LRRC15 protein.....	105
Supplemental Figure 3.2. Live confocal microscopy-based assays to determine internalization kinetics of DUNP19 after chelator conjugation and in various cell types.....	106
Supplemental Figure 3.3. Expanded tumor biodistribution of [¹⁷⁷ Lu]-DUNP19.....	107
Supplemental Figure 3.4. IHC and IF analysis of <i>ex vivo</i> LRRC15+ tumor models.....	107
Supplemental Figure 3.5. Animal weights across tumor models.....	108

Supplemental Figure 3.6. Toxicity studies examining blood cell counts during treatment course across tumor models.....	109
Supplemental Figure 3.7. Principal component analysis (PCA) plots of whole transcriptome cancer cell reads.....	110
Supplemental Figure 3.8. Relative cell characterization of individual tumor samples using Syllogist.....	111
Supplemental Figure 3.9. Stromal cell expression of <i>Lrrc15</i> and <i>Tgfb1</i>	112
Figure 4.1. Dissection and modulation of the TGF β -LRRC15 axis in select cancer cell lines.....	133
Figure 4.2. ScRNAseq reveals distinct transcriptional signatures in TGF β -inducible cancer cell lines.....	136
Figure 4.3. Network analysis of TGF β -responsive transcriptional signatures.....	139
Figure 4.4. Integration of high-throughput drug screening and scRNAseq reveals converging molecular pathways regulating LRRC15 in TGF β -inducible cells.....	142
Figure 4.5. High expression of LRRC15 activating genes predicts immunotherapy resistance and tumor progression.....	150
Supplemental Figure 4.1. Compound screening controls.....	163
Supplemental Figure 4.2. Network Analysis.....	164
Supplemental Figure 4.3. scRNAseq quality control plots pre-filtering (left) and post-filtering (right).....	165
Supplemental Figure 4.4. Loss of gene expression in LRRC15 activators after LRRC15-targeted radioimmunotherapy.....	166
Supplemental Figure 4.5. LRRC15 expression activators predict survival in TCGA mesenchymal-derived tumors.....	167
Supplemental Figure 4.6. Survival and hazard ratios in tumors based on cell line models.....	168

Supplemental Figure 4.7. Correlation of LRRC15-associated genes with LRRC15 expression in TCGA tumor cohorts.....	169
Supplemental Figure 4.8. LRRC15 expression activators predict survival in patients with PD1 blockade.....	171
Supplemental Figure 4.9. Correlation between previously identified CAF LRRC15 signatures and our LRRC15 gene signatures.....	172
Table 3.1. Biodistribution in SAOS2 models.....	113
Table 3.2. Biodistribution in HuO9 models.....	114
Table 3.3. Biodistribution in U118MG models.....	115
Table 3.4. Biodistribution in K7M2 models.....	116
Supplemental Table 3.1. Gene set enrichment analysis of cancer cells.....	117
Supplemental Table 3.2. Gene set enrichment analysis of stromal cells.....	118
Table 4.1. Top gene candidates for modulating the TGF β -LRRC15 axis.....	144
Supplemental Table 4.1. Compound hits from LOPAC1280 screen across three cell lines. Hits are represented as normalized effect on LRRC15 expression.....	172

CURRICULUM VITAE

EDUCATION

University of California, Los Angeles, 2019 – exp. 2025
PhD Candidate, Molecular and Medical Pharmacology
Thesis: “Exploring Disease-Driven Biomarkers for Radio-Theranostic Targeting in Cancer”
- GPA: 3.9/4.0

University of North Carolina at Chapel Hill, B.S. Biology, Chemistry 2013 – 2017
- 2017 Carolina Research Scholar (awarded to 30 undergraduates in North Carolina)

RESEARCH EXPERIENCE

UCLA David Geffen School of Medicine – selected projects and collaborations 2019 – 2024
Radiopharm Theranostics, Collaborating Research Scientist

- Co-invented and patented a novel antibody-based therapeutic (DUNP19) for pediatric bone cancer.
- Led DUNP19 drug proof-of-concept and *in vitro* efficacy studies resulting in a licensing agreement and collaboration with Radiopharm Theranostics (Apr. 2022).
- Authored a project proposal that secured additional funding for ongoing research studies to find novel therapeutic targets at UCLA (Oct. 2022).
- Collaborated with three academic research teams in Lund (Sweden), Essen (Germany), and St. Louis, MO, hosting weekly meetings, presenting project summaries, and communicating with lead scientists.

Janssen Pharmaceuticals (Johnson & Johnson), Collaborating Research Scientist

- Led UCLA’s *in vitro* research team as part of a 5-year collaboration with Janssen Pharmaceuticals focused on identification of prostate cancer resistance mechanisms.
- Generated new experimental models using CRISPR-Cas9 technologies to support an ongoing Phase I clinical trial, summarizing progress in quarterly meetings with Janssen project leads.
- Consistently met Janssen’s project milestones and generated data that resulted in additional funding for UCLA’s prostate cancer research group.
- Published key research findings in *Molecular Cancer Research* (impact factor 6.33, Apr. 2023).

Stanford University School of Medicine – selected projects and collaborations 2017 – 2019
Division of Endocrinology, Research Scientist

- Developed a novel model of endocrine cancer, published in *Cell Reports* (impact factor 9.95, Mar. 2022) in collaboration with 3 research labs within Stanford Medicine and Stanford Engineering.
- Established tumor analysis pipeline for high-throughput processing, imaging, and data collection, uncovering metabolic alterations in neuroendocrine tumor formation.

PUBLICATIONS & CONFERENCE PRESENTATIONS

Storey CM, Altai M, Bicak M, Veach DR, Lückerrath K, Adrian G, McDevitt MR, Kalidindi T, Park JE, Herrmann K, Abou D, Zedan W, Peekhaus N, Klein RJ, Damoiseaux R, Larson SM, Lilja H, Thorek D, Ulmert D. Quantitative In Vivo Imaging of the Androgen Receptor Axis Reveals Degree of Prostate Cancer

Radiotherapy Response. *Mol Cancer Res.* 2023 Apr 1;21(4):307-315. doi: 10.1158/1541-7786.MCR-22-0736. PMID: 36608299.

Armstrong N, **Storey CM**, Noll SE, Margulis K, Soe MH, Xu H, Yeh B, Fishbein L, Kebebew E, Howitt BE, Zare RN, Sage J, Annes JP. SDHB knockout and succinate accumulation are insufficient for tumorigenesis but dual SDHB/NF1 loss yields SDHx-like pheochromocytomas. *Cell Rep.* 2022 Mar 1;38(9):110453. doi: 10.1016/j.celrep.2022.110453. PMID: 35235785; PMCID: PMC8939053.

Veach DR, **Storey CM**, Lückerath K, Braun K, von Bodman C, Lamminmäki U, Kalidindi T, Strand SE, Strand J, Altai M, Damoiseaux R, Zanzonico P, Benabdallah N, Pankov D, Scher HI, Scardino P, Larson SM, Lilja H, McDevitt MR, Thorek DLJ, Ulmert D. “PSA-Targeted Alpha-, Beta-, and Positron-Emitting Immunotheranostics in Murine Prostate Cancer Models and Nonhuman Primates.” *Clin Cancer Res.* 2021 Jan 13. Doi: 10.1158/1078-0432.CCR-20-3614. PMID: 33441295.

*Highlighted Feb. 2021 in *Nature Reviews Urology*, 18, 131 (2021)

Albright BH, **Storey CM**, Murlidharan G, Castellanos Rivera RM, Berry GE, Madigan VJ, Asokan A. “Mapping the Structural Determinants Required for AAVrh.10 Transport across the Blood-Brain Barrier.” *Mol Ther.* 2018 Feb 7;26(2):510-523. Doi: 10.1016/j.ymthe.2017.10.017. PMID: 29175157.

Storey CM, Albright BH, Asokan A. “Determining tropism of AAV constructs across the blood-brain barrier”. Carolina Research Symposium, April 2017.

HONORS & AWARDS

2021 UCLA Pharmacology Best Scientific Presentation

“Targeting LRRC15: A TGF- β Driven Biomarker in Mesenchymal Stem Cell-derived Cancers”

2017 Carolina Research Scholar

Awarded to 30 undergraduate students at UNC Chapel Hill who significantly contribute to the Carolina research community. Completed two years of independent research in the UNC School of Medicine, authored a peer-reviewed publication, presented at the Carolina Research Symposium, and participated in multi-disciplinary research-intensive courses.

2017 Buckley Public Service Scholar

Awarded to UNC Chapel Hill students who perform 300 hours of public service to North Carolina-based communities and organizations.

TEACHING & MENTORSHIP

Research Mentorship

2021 – 2024

- Mentorship of two UCLA undergraduate students (Julie Park, 4th year + Alexander Ridley, 1st year) participating in independent laboratory research. Teaching advanced lab techniques (cell culture, confocal microscopy, high-content screening) and experimental design.

Teaching Assistant

2014 – 2016

BIOL 101L, 102L - UNC Department of Biology

- Planned and taught introductory biology lab techniques including molecular biology, genetics, and anatomy to first year undergraduate students and provided weekly one-on-one tutoring and support for lab reports and coursework.

CHAPTER 1. INTRODUCTION

1.1 Antibodies

i. Antibody Structure and Function

Antibodies are an essential component of the adaptive immune system, aimed at detecting disease-causing foreign antigens. Their high specificity and affinity for a target antigen led to their description as “magic bullets” after their discovery in 1890. Monoclonal antibodies (mAbs) have emerged as a cornerstone of modern therapeutic strategies, offering highly specific interventions across a wide range of diseases, including cancer, autoimmune disorders, and infectious diseases. Their rapid rise to prominence is evidenced by the projected \$300 billion market value by 2025 [1]. This growth is driven by the unique ability of mAbs to target a variety of molecules, including cytokines, cell surface receptors, and immune checkpoint molecules, thus allowing for precision treatment of pathophysiological processes.

Y-shaped monoclonal antibody proteins have an approximate mass of 150 kDa and consist of four polypeptide subunits, each subunit contains two identical light and heavy chains interconnected by disulfide bonds. There are two antigen-binding domains forming the arms of the “Y” shape, called the Fab (Fragment, antigen-binding) regions. The tip of each Fab contains unique and variable regions that binds to its specific antigen. A constant subunit is located below the variable region and is used to classify antibodies by their isotype. A hinge region links the Fab regions with the crystallizable fragment (Fc) and facilitates interaction with cell surface Fc receptors. Specific motifs on the Fc trigger the activation of effector immune cells, leading to

antibody-dependent cellular cytotoxicity (ADCC), but can also regulate the classical complement pathway, controlling complement-dependent cytotoxicity (CDC).

The production of mAbs for clinical use relies on multiple expression systems, each with distinct advantages and limitations. Traditionally, hybridoma technology has been utilized, wherein B-cells are fused with myeloma cells to generate hybridomas that are then screened and cloned for monoclonal antibody production [2]. However, hybridomas produce murine antibodies, which can elicit immune responses in humans due to their non-human origin. To avoid activation of human antimouse antibody (HAMA) responses, new methods have been developed to humanize murine-derived antibodies. Chimeric antibodies utilize mouse variable domains with a human immunoglobulin (IgG) to replace the constant domain. Doing so successfully reduced immune reactions in patients [3, 4]. Further advancements in antibody technology were made with the introduction of humanized monoclonal antibodies that contained less non-human protein than their chimeric counterparts. Humanized antibodies were first accomplished by grafting a complementary-determining region, or CDR, onto a human IgG scaffold [5].

In parallel with the evolution of antibody generation techniques, significant advancements have been made in the optimization of expression systems. Cell lines such as Chinese Hamster Ovary (CHO) and HEK293 cells have emerged as the preferred platforms for mAb production due to their ability to introduce post-translational modifications, including glycosylation [2]. Glycosylation patterns, particularly in the Fc region of IgG molecules, are crucial for determining immune effector functions, such as ADCC and CDC. Human embryonic kidney cells, or HEK293 cells, are favored for their ability to mimic native human glycosylation, a critical factor in minimizing immunogenicity and maximizing therapeutic efficacy [2].

In the field of nuclear medicine, the Fc region has been viewed as redundant and various Fc-edited antibody-like platforms have been invented [6]. Omitting the Fc-region decreases the antibody's half-life, increases tissue penetrance and permits for renal clearance. However, the Fc region contains motifs for activation of both effector immune cells and the classical pathway of the complement (C1q) responsible, respectively, for ADCC and CDC. One of the most important breakthroughs in the field of immunology during the last two decades is the discovery and characterization of the Fc-portions interaction with Fc γ receptors (Fc γ R). Fc γ R are low affinity receptors found on the surface of leukocytes [7] which orchestrates ADCC through cytotoxic effects via agonistic and antagonistic binding. The specific Fc γ R engaged by a given Fc domain is dictated by Fc structure, which is determined by the IgG subclass. An example of the multifaceted therapeutic activity of Fc γ Rs is checkpoint-inhibitor mAbs (anti-CTLA4) that mediate antitumor activity by altering the composition and functional activity of leukocytes within the tumor microenvironment. However, the therapeutic action is also an effect of the mAb's capacity to activate Fc γ R expressing macrophages within the tumor microenvironment [8].

IgG subclasses differ in their binding profiles, half-lives, and Fc receptor binding and can mediate different therapeutic responses [9]. While most FDA-approved monoclonal antibodies are of the IgG1 subtype, IgG2, IgG3 and IgG4 mAbs are also in clinical use [10]. Several studies have compared the IgG subtypes and found varying results based on the target antigen and cell type [11]. A study targeting antigen CD146 in osteosarcoma xenograft models generated chimeric mAb variants with human IgG1 and IgG3 constant regions, finding that the two subtypes demonstrated similar antigen binding but different biodistribution profiles [11]. When

labeled with Iodine-125, the IgG1 chimeric mAb displayed higher tumor uptake than its IgG3 counterpart. This observation was replicated in biodistribution studies with [¹⁷⁷Lu]-labeled mAb, however, higher uptake was noted in the liver with the IgG1 subtype, alluding to the key clinical decision points to be made in therapeutic antibody development. In terms of size, the IgG3 subtype is 24kD larger than the other three IgG subtypes and certain allotypes have a significantly shorter half-life in the blood (7 days versus 20-21 days for the other IgGs) [10]. This shorter half-life is attributed to the lower affinity of IgG3 for the neonatal Fc receptor (FcRn) that protects antibodies from degradation and promotes transcytosis, internalization and recycling [12].

Over the past 50 years, essential Nobel Prize-winning advancements have propelled the field forward. Some of these findings include Edelman and Porter's discovery of the mAb structure, as well as Köhler and Milstein's hybridoma technology. Smith's invention of phage display and Winter's applications of the technology for engineering of mAbs further accelerated development of novel compounds [13]. These ground-breaking discoveries and innovations provided opportunities to utilize antibodies in cancer treatment, which was realized in 1980 when the first mAb human trial was designed to treat lymphoma.

ii. Clinical and Therapeutic Applications of mAbs

1. Naked Antibodies + Antibody-Drug Conjugates

Monoclonal antibodies have significantly advanced the field of targeted cancer therapy. Engineered to bind to specific antigens expressed by cancer cells, mAbs can circumvent the challenges of toxicity and off-target effects by taking advantage of protein targets that

exclusively appear on cancer cell surfaces. The clinical success of mAbs is best exemplified by drugs like Rituximab (Rituxan), which targets B-cell surface antigen CD20 for the treatment of non-Hodgkin's lymphoma. Other strategies have exploited the immune system's ability to target tumor cells with immune checkpoint inhibitors such as Nivolumab (OPDIVO) and Ipilimumab (Yervoy). These therapies are part of a growing list of mAbs approved for oncology and immunology, offering patients more effective and targeted treatments with fewer side effects than traditional chemotherapy or immunosuppressive drugs.

To improve the therapeutic potential of mAbs, various engineering strategies have been developed. One notable advancement has been the generation of antibody-drug conjugates (ADCs), involving the coupling of cytotoxic agents to mAbs. This allows for the targeted delivery of potent drugs directly to malignant cells, minimizing off-target effects. ADCs have shown remarkable efficacy, particularly in the treatment of HER2+ solid tumors, with the first Her2-targeted ADC using the already approved anti-HER2 mAb trastuzumab to deliver a topoisomerase I inhibitor [14].

2. Radioimmunotheranostics Applications

Theranostics combines a diagnostic agent and a therapeutic agent, either with a single radionuclide conjugate or two paired radionuclides, one for non-invasive imaging and one for therapeutic intent. Radioimmunotherapy (RIT) represents a powerful theranostic modality that integrates the specificity of monoclonal antibodies with the cytotoxic capabilities of radionuclides. This approach offers a highly targeted means of delivering radiation directly to malignant cells, thereby minimizing off-target effects and preserving healthy tissue. Cancer cells

emerge, in part, as a result of the accumulation of genetic mutations. These changes render them susceptible to death by ionizing radiation, making radiotherapy a pillar of cancer therapy. Once the mAbs bind to their target on cancer cells, the attached radioisotope decays, emitting ionizing radiation that directly interacts with the DNA or generates reactive oxygen species (ROS), leading to double-strand DNA (dsDNA) breaks (DSBs) and other forms of damage [15,16]. Double-stranded breaks can be particularly toxic as they damage both DNA strands, often leading to irreversible cell cycle arrest or mitotic catastrophe, especially in cancer cells with heavily mutated or defective DNA damage response (DDR) pathways. Cells unable to manage this stress may undergo programmed cell death or other forms of cell death, like necrosis or immunogenic cell death, which can further stimulate the body's immune system to attack the remaining tumor. In this way, RIT provides a dual mechanism: direct radiation-induced cytotoxicity and the potential to enhance the immune response through antigen release from dying cancer cells.

By exploiting tumor-associated antigens, RIT enables precise tumor targeting, making it an attractive option in cancers that are refractory to conventional therapies. The clinical success of RIT, however, is contingent upon the identification of robust, tumor-specific antigens that can serve as reliable targets for both therapeutic and diagnostic applications. Preclinical and clinical trials have demonstrated that successful target antigens for solid tumor RIT must be highly expressed on tumor tissue and that the most effective targets support tumor growth, maintenance, or survival [17]. Another critical challenge in optimizing RIT is understanding the underlying pathobiology and regulations of target antigens. Tumor heterogeneity, immune evasion, and therapy resistance are major obstacles to effective cancer treatment, underscoring the need to

elucidate the molecular pathways governing these processes and, in turn, tumor antigen expression.

In a seminal study from 1978 on tumor detection in humans using ¹³¹I-labeled anti-CEA antibodies, Goldenberg concluded that successful imaging primarily depends on the specific and sensitivity of the antibody [18]. The study was based on an affinity-purified goat antibody labeled with ¹³¹-Indium targeting carcinoembryonic antigen (CEA). Early imaging technologies to assess radiolabeled monoclonal antibody biodistribution were established using gamma cameras. Iodine-131 labeled anti-CD-37 and anti-CD-20 in B-cell lymphoma patients provided a foundation for the theranostic approach to evaluating RIT treatment response in patients [19,20], with the expansion of radioisotopes for labeling leading to the use of PET as a dose-planning tool for radioimmunotherapy. This was first demonstrated using Iodine-124 labeled anti-GD2 mAb 3F8 to target the surface of neuroblastoma cells to B7-H3 protein in neuroblastoma patients [21]. The approach used Iodine-124-labeled 3F8 as an imaging agent to determine candidates for ¹³¹I-3F8 radioimmunotherapy, guiding treatment measures based on the indicated dose and uptake by the ¹²⁴I-labeled mAb [21].

At the same time, hybridoma technologies were introduced which have since revolutionized our possibilities to develop highly specific monoclonal antibodies (mAbs) [22]. The first mAb (Muromonab) was approved 1986, and approximately 70 mAbs have since then been introduced for treatment or management of a variety of diseases use in humans. During the same time span, only three radiolabeled mAbs (⁹⁰Y]-Ibritumomab, [¹³¹I]-Tositumomab and [¹¹¹In]-Capromab) have reached FDA approval. Two of these RITs, [¹³¹I]-tositumomab (Bexxar) and [⁹⁰Y]-

Ibritumomab (Zevalin), target lymphocyte CD20 receptors for treatment of refractory B-cell non-Hodgkin's lymphoma [23]. Despite the success of Bexxar performing as well as Rituximab in B-cell non-hodgkins lymphoma (NHL), the therapy is not currently available [24]. Lagging FDA approval and the solidifying of Rituxan and chemotherapy (R-CHOP) for NHL as the standard of care kept use of Bexxar low. However, a study comparing Bexxar to the Rituxan regimen found no significant differences in toxicities, survival rates or disease progression, citing both treatments perform equally well in the treatment of NHL [25]. Anti-CD20 Zevalin is the only FDA-approved RIT currently available to B-cell NHL patients. Currently approved for refractory or low-grade NHL as well as patients with resistance to rituximab, Zevalin is being tested as a front-line therapy across B-cell lymphomas [26,27] as well as a trial using 18F-FDG-PET to direct treatment to either R-CHOP or RIT [28-31]. Lymphomas are particularly good candidates for radiotherapeutic approaches due to the specific and high expression of antigens on tumor cells, sensitivity to radiation therapy and well-incorporated nuclear imaging protocols. Expanding the field of oncology treatments to RIT should be at the forefront of the next generation of lymphoma treatments

iii. Therapeutic Radionuclides

RIT relies on delivering targeted doses of radiation directly to cancer cells using mAbs conjugated to radioactive isotopes. A critical component of RIT's efficacy is the development of appropriate dosing strategies and injected activity, ensuring that therapeutic radiation is delivered precisely to tumor tissues while minimizing exposure to healthy cells. The therapeutic window is often expanded by using isotopes with appropriate emission ranges. Beta-emitters like Yttrium-90 have a moderate tissue penetration range that is ideal for targeting larger tumors,

whereas alpha-emitters like Actinium-225 offer high linear energy transfer (LET) radiation that is extremely potent but limited in range, making them suitable for eradicating micrometastatic disease while sparing surrounding tissues.

Beta emitters are the most frequently utilized radionuclides in RIT due to their relatively moderate tissue penetration that can span several cell diameters (2.5mm-10mm) and widespread availability. Beta radionuclides can induce cellular damage to both the target cells expressing the target antigen as well as nearby cells within the emission path, known as the “crossfire effect.” This makes beta emitters particularly effective in treating larger or more heterogeneous tumors. Notable examples of beta radionuclides include Yttrium-90 [^{90}Y] and Lutetium-177 [^{177}Lu]. [^{90}Y], with a half-life of approximately 64 hours, emits high-energy beta particles (2.28 MeV) that penetrate up to 10 mm in tissue [32]. In contrast, [^{177}Lu] (half-life = ~6.6 days) emits both beta particles and low-energy gamma rays to allow for imaging but has a shorter tissue penetration range (~2 mm). Given the longer half-life and imaging capabilities, the radionuclide is a practical choice for small tumors for both diagnostic and therapeutic applications [33].

Alpha particles provide a more targeted approach due to their high linear energy transfer (LET) and short range in tissues (~50–100 micrometers). Alpha-emitting radionuclides such as Actinium-225 [^{225}Ac] and Radium-223 [^{223}Ra] release particles that densely ionize atoms along their path due to their larger mass and double positive charge [34]. This ionization induces multiple double-stranded DNA breaks that are more difficult for cells to repair, resulting in enhanced cytotoxicity per particle and increasing effectiveness for micrometastatic disease, with

the short range of alpha particles also reducing off-target toxicity, sparing surrounding healthy tissue.

Auger electrons represent a specialized class of radionuclides whose therapeutic potential is contingent on proximity to subcellular DNA. Auger electrons are low-energy with minimal tissue ranges of ~10-100nm [35]. Auger-emitting radionuclides such as Iodine-125 [¹²⁵I] or Indium-111 [¹¹¹In] must localize very closely to the cell nucleus [35]. When auger emitters are internalized into the cell and deposited near the DNA, they cause substantial DNA damage by generating complex double-strand breaks, effectively inducing cell death. Finally, gamma emitters play a dual role in radioimmunotherapy, often used in combination with other radionuclides to facilitate both therapeutic effects and imaging. Gamma rays, which have very low LET do not exhibit the same toxicity to the same extent as beta or alpha radiation. However, they are critical for diagnostic purposes for use in imaging modalities like SPECT or PET, allowing for non-invasive imaging of the radiolabeled antibody's distribution.

1. Radiolabeling Methods

Radiolabeling with metallic radionuclides require that the mAb is first conjugated with a chelator, forming a complex by providing donor atoms to saturate its coordination sphere and prevent hydrolysis [36]. Typically, chelators such as DFO, DTPA, or DOTA are used; one side can bind covalently to the mAb, while the other chelates the radionuclide [37]. A linker molecule can act as a spacer to ensure that the radionuclide remains conjugated to the mAb until it reaches target tissue and ensures that the radionuclide does not interfere with the pharmacokinetic properties of the antibody [38]. In standard practice, radioimmunoconjugates are synthesized by

random covalent bonds between the chelator and lysines on the antibody. Although simple and generally applicable, the method produces a complex assortment of radiolabeled mAbs that are poorly defined and heterogenous among different syntheses. Upon selection of an appropriate chelator and linker, the payload can be added to the antibody at the mAb's lysine or cysteine residues. Amine-reactive ester reactions on lysine residues are the most common methodology, but disulfide bond reduction on cysteine residues can also be used [39].

To improve upon stochastic labeling, the mAb structure can be engineered with specific sites containing 'unnatural amino acids', such as short peptide tags or glycans, which provide predetermined binding sites for the chelator. The first in-human trial of a site-specifically labeled [⁸⁹Zr]-DFO-Pertuzumab is currently in Phase I clinical trials for patients with HER2-positive metastatic breast cancer [40]. Some radionuclides, such as Iodine isotopes, can covalently bind to the mAb via iodination, eliminating the need for a chelating agent [41], however, this process can leave the isotope subject to dehalogenation in vivo, effectively reducing the circulating time and effective half-life [42,43]. It is also essential that the chelation chemistry does not significantly alter the mAb's binding qualities and stability, as the choice of radiolabeling method can have a significant impact on successful delivery of the radionuclide to target tissue [37]. Upon endocytosis of radiolabeled mAbs, chelate-based methods enable cytoplasmic entrapment of the radionuclides, while iodination generates low molecular weight radio-catabolites that escape the targeted cells by passive transport.

For radioimmunotherapeutic modalities to be most effective, differences in internalizing ability and half-life must be considered. For instance, certain radioisotopes with short path lengths such

as auger and alpha emitters are only effective when the radioimmuno-conjugate is internalized. In addition, given the long circulation time and tumor retention, full-size mAbs are highly suitable as carriers of radionuclides with long half-lives such as Zirconium-89 or Indium-111 for PET- or SPECT-imaging and Lutetium-177 or Actinium-225 for radiotherapy. Full-size antibodies with longer serum half-lives may require lower injected activities due to prolonged circulation, which provides more time for the radioconjugate to accumulate in the tumor. In contrast, smaller antibody fragments with shorter half-lives clear from the bloodstream more rapidly via renal clearance and may require higher injected activities to achieve effective tumor uptake [44].

Despite mAbs being relatively advantageous for RIT, there are drawbacks to utilizing mAbs as vehicles for radionuclides. The neonatal fc-receptor (FcRn) mediates temporary cellular internalization by binding to the fc portion, a process that protects IgGs from degradation and thus extends half-life [45]. In addition, FcRn functions as a receptor for transcytosis of IgGs across polarized membranes [46]. The prolonged blood circulation increases exposure to radiosensitive organs, which limits the therapeutic dose that can be given and delays the time to get an optimal image. Acute hematological toxicity is the most observed adverse event in radioimmunotherapy of solid tumors due to a low tumor-to-nontarget ratio and off-target radiation damage due to the prolonged circulation time of mAbs in the blood [47].

Full sized antibodies also lack the ability to naturally reach across barriers of non-fenestrated endothelial cells, such as glial processes in the brain and sertoli cells in the testis. Although preclinical manufacturing of mAbs are fairly simple and inexpensive, production under Current

Good Manufacturing Practices (CGMP) require substantial monetary assets, or production facilities that are rarely found at academic institutions. Large pharmaceutical companies are hesitant to take on products utilizing preclinical radiolabeled mAbs, especially compounds aimed for diagnostic imaging. Unfortunately, numerous very interesting and innovative mAb-based projects have stranded at this stage.

Successful radioimmunotherapy of solid tumors is uniquely challenging due to the decreased radio-sensitivity and high radiation dose requirements for efficacy. Bone marrow toxicity and low tumor-to-normal tissue targeting and heterogeneity in target expression are major complications for radioimmunotherapy of solid tumors. In addition, physical barriers such as the extracellular matrix, elevated interstitial fluid pressure and poor tumoral vascularization also contribute to RIT efficacy limitations [48,49].

2. SPECT, PET, and Theranostics

Antibody-based imaging in SPECT and PET represents a convergence of precision-targeted therapeutics and advanced diagnostic modalities, providing improved resolution in both tumor localization and real-time assessment of therapeutic response. PET imaging capitalizes on the use of positron-emitting radionuclides like Fluorine-18, Iodine-124, Zirconium-89, Copper-64, and Gallium-68, which each offering distinct advantages based on their half-lives, decay profiles, and compatibility with different antibodies. For instance, [⁸⁹Zr], with its longer half-life of 3.3 days, is particularly suitable for imaging slow biological processes such as the distribution of monoclonal antibodies in vivo, making it ideal for long-term tracking of therapeutic antibodies [50]. [⁸⁹Zr]-labeled trastuzumab, for example, is highly effective in

imaging HER2-positive tumors, allowing precise monitoring of receptor occupancy and response to HER2-targeted therapies. Similarly, SPECT imaging utilizes gamma-emitting radionuclides such as Indium-111 or Technetium-99. Although SPECT has lower spatial resolution compared to PET, it remains widely used due to its cost-effectiveness and availability [51].

Advancements in [⁸⁹Zr]-labeled PET tracers such as VEGF-targeting modality [⁸⁹Zr]-bevacizumab have broadened the scope of PET imaging, making it a versatile tool for monitoring anti-angiogenic therapies across a variety of solid tumors [52]. By visualizing VEGF expression and tracking the response to widely-used VEGF inhibitors such as Everolimus, clinicians can tailor treatments to individual patient profiles, visualize changes in VEGF signaling, and improve therapeutic efficacy.

1.2. Biomarkers and Therapeutic Targets

i. AR + KLK2

Biomarkers are understood as “a defined characteristic that is measured as an indicator of normal biological processes, pathogenic processes, or responses to an exposure or intervention, including therapeutic interventions” according to the NIH Biomarker Working Group [53]. Specific to oncology, biomarkers can be used to diagnose, stage, and stratify patients for treatment. In prostate cancer, for example, the androgen receptor (AR) pathway plays a pivotal role in tumor progression. Biomarkers that reflect the molecular activity downstream of the AR can offer important insights into the efficacy and resistance of pharmaceuticals designed to inhibit this central disease driver. Human kallikrein related peptidase 2 (hK2, KLK2) is an AR-

governed trypsin-like enzyme that is only expressed in prostate tissues. Both pre- and clinical studies of radio-conjugated anti-hK2 mAb hu11B6, which binds to a unique epitope in the catalytic cleft of hK2, have shown highly encouraging results. Findings based on hu11B6 have shown that positron emitter [^{89}Zr] can be used as a surrogate reporter for alpha emitter [^{225}Ac] with parallel pharmacokinetic profiles and organ uptake. A dosimetry study testing ^{111}In hu11B6 in mCRPC patients was the first hK2 targeting radioimmuno-theranostic approach in humans and found accumulation in bone and soft tissue metastases with minimal evidence of off-target effects or toxicity [54]. Multiple hu11B6-based compounds have since been initiated, including an [^{225}Ac]-labeled version, as well as non-radioactive alternatives like hK2-targeted T-cell engagers [55].

Imaging of androgen receptor signaling in prostate cancer nicely fits the theranostic approach. Because the AR pathway is a driver of disease, downstream signaling targets can provide a window into the efficacy of therapeutics and reactivation when resistance develops. Anti-hK2 mAb hu11B6 has demonstrated its potential in AR-dependent imaging and PCa treatment. Preclinical studies in mouse and nonhuman primates utilized Zirconium-89 and Actinium-225-conjugated hu11B6 to image and treat prostate cancer [56]. Positron emitter [^{89}Zr] acted as a surrogate reporter for alpha emitter [^{225}Ac] with parallel pharmacokinetic profiles and organ uptake. Additional preclinical studies using Indium-111 hu11B6 in AR-positive PCa xenografts led to a dosimetry trial in mCRPC patients, the first targeting hK2 with a radioimmuno-theranostic approach in humans [54,57].

ii. TGFB + LRRC15

Similar to AR, the transforming growth factor beta (TGF β) signaling pathway is recognized as a key driver of tumor progression, immune suppression, and metastatic potential across various cancer types. TGF β signaling is perhaps the most pervasive contributor to late-stage disease progression through suppression of anti-tumor immune responses. TGF β 's role as a pleiotropic cytokine modulates the differentiation, proliferation, migration, and survival of immune and non-immune cells within the tumor microenvironment to shield cancer cells from immune attack and further promote tumor growth [58-60]. Systemic pharmacological inhibition of TGF β activity through TGF β -blockade has been unsuccessful due to TGF β 's key functions in tissue healing and immune regulation of healthy tissue, often leading to accelerated disease progression followed by increased pro-tumorigenic TGF β signaling [61,62]. Thus, there is an unmet need for the selective inhibition of TGF β signaling in tumors that are resistant to immunotherapy, while sparing healthy tissue and normal physiological functions of TGF β .

Cancer-associated fibroblasts (CAFs) within the tumor microenvironment (TME) have impeded therapeutic strategies through their mechanical support of tumor cells, physical blockade of anti-tumor drugs, immunomodulation, and biochemical aid in tumor cell growth and survival [63-68]. CAF-rich tumors exhibit increased endurance to standard chemotherapy regimens used in the clinic [69,70] and have repeatedly failed small molecule trials due to the stroma's barrier to drug delivery and multitude of upregulated resistance mechanisms in response to therapeutics [71-73]. In addition, the tumor stroma heavily regulates immune cell infiltration and can limit anti-tumor immune response, thus weakening tumor response to immunotherapy [68].

Within this context, leucine-rich repeat-containing protein 15 (LRRC15) has emerged as a promising therapeutic target. LRRC15 is a transmembrane protein governed by TGF β and is upregulated in the tumor microenvironment of highly aggressive malignant lesions, particularly in stromal and fibrotic tissues, as well as malignancies originating from mesenchymal stem cells (MSCs) [74]. Studies conducted on murine cancer models and human tumor tissues have revealed that the presence of LRRC15+ CAFs, together with a panel of 10 other genes, make up nearly half of all CAFs within the tumor microenvironment [75]. Notably, LRRC15 expression is low in healthy tissues making the protein an excellent target for therapeutic intervention downstream of TGF β signaling. However, little is known regarding the proposed pathological role of LRRC15. Genetic ablation of LRRC15-expressing CAFs significantly reduces tumor growth in murine models of pancreatic cancer, as well as ameliorate the antitumor immune response after anti-PDL1 immunotherapy through enhanced CD8+ T cell function and infiltration [76]. In murine models, targeting LRRC15 in tumor stroma has proven to be efficacious for both reducing tumor volume and improving response to immune checkpoint blockade (ICB) [76]. However, the LRRC15-targeted antibody-drug conjugate ABBV-085 showed little reduction in tumor volume in sarcoma patients during a Phase I/II trial, likely due to the heterogeneity of LRRC15 expression [77,78].

Here, we propose LRRC15 as a theranostic target, both as a diagnostic marker for selecting patients with advanced disease as well as a radioimmunotherapeutic target. Even with heterogeneous LRRC15 expression, we demonstrate that targeting LRRC15 with a radionuclide-antibody conjugate can elicit antitumor effects such as the suppression of tumor growth, loss of TGF β -driven expression patterns, and enhanced survival across several models of aggressive

disease. Immunotherapy has revolutionized the treatment of hematological malignancies, demonstrating remarkable response rates and achievement of long-term survival in patients with otherwise incurable disease. However, the success of immunotherapy in solid tumors has been limited to a small percentage of patients. Non-responders are subject to a wide range of resistance mechanisms including immune cell exhaustion in larger solid tumors, physical barriers preventing immune infiltration, and cytokine-mediated signaling that hijack immune responses critical to successful treatment.

As mentioned, attempts have been made to exploit LRRC15's potential as a therapeutic target, including AbbVie's ABBV-085, a LRRC15-targeted antibody-drug conjugate. The compound employs an antimitotic drug, monomethyl auristatin E (MMAE), coupled to a LRRC15 antibody through a protease-cleavable valine-citrulline linker. Preclinical assessments of therapeutic efficacy displayed promising results in murine models of human tumors. However, the outcome of a Phase 1 study in a cohort of mixed malignancies did not suggest that further investigation of ABBV-085 would yield significant clinical benefits. We hypothesize that the ADC's success was hindered by two major factors, heterogeneity of LRRC15 tumor expression and characteristics of the antibody vehicle utilized by Abbvie for targeted delivery, including lack of internalization of the ADC into target cells and lack of selection for patients with LRRC15+ disease.

Given the lack of efficacy of Abbvie's LRRC15-targeted ADC, it is important to recognize the widely varied LRRC15 expression patterns observed across patients and indications. Tumors may express high LRRC15 in cancer cells, but do not express LRRC15 within the stroma. This

presents a challenge for LRRC15-targeted therapy on two levels- one being the need for an imaging agent that can guide therapeutic approaches, the other being the need to deliver a cytotoxic modality that can overcome this heterogeneous landscape. To test this hypothesis, we developed a LRRC15 humanized IgG1 monoclonal antibody, DUNP19. DUNP19 exhibits rapid internalization by target cells following binding to a phylogenetically conserved epitope on LRRC15 with picomolar affinity. The antibody's equimolar binding to murine LRRC15 provides valuable opportunities to explore off-target toxicity and therapeutic effects resulting from LRRC15+ CAF targeting within the tumor microenvironment [76].

Comparatively, ABBV-085 does not undergo endocytosis upon binding to LRRC15, and release of the cytotoxic payload relies on proteases present in the tumor microenvironment and the hydrophobic nature of monomethyl auristatin E (MMAE) to cross the cell membrane. With the use of an ADC, there is a potential risk of incomplete or inefficient cleavage of the protease-cleavable linker, leading to inadequate release of the cytotoxic payload at the target site and limitations on the maximum dose delivered to target tissue. Additionally, extra-tumoral release of cytotoxic payload may result in non-specific accumulation and toxicity in healthy tissues. As an alternative to an ADC-based approach and address the challenges encountered with ABBV-085, we opted to develop DUNP19 as a radio-immunotheranostic modality that could be used as a tool for non-invasive imaging as well as a therapeutic for delivering cytotoxic radionuclides. This innovative strategy enables non-invasive and image-driven selection of patients with LRRC15-expressing disease. Moreover, it offers the potential for individualized dose planning, thereby enhancing the likelihood of eradicating TGF β -driven disease associated with LRRC15 expression. We hypothesized that conjugation of the beta-emitting radionuclide Lutetium-177

to DUNP19 ($[^{177}\text{Lu}]\text{DUNP19}$) could not only induce DNA damage in LRRC15+ cells upon decay, but also in CAFs and LRRC15-negative cells in close proximity to the target cell. In this study, we present the precise molecular accumulation of $[^{177}\text{Lu}]\text{DUNP19}$ in tumor models with LRRC15+ cancer cells and CAFs, as well as in tumor models where LRRC15 expression was restricted to CAFs. We evaluated the therapeutic efficacy of $[^{177}\text{Lu}]\text{DUNP19}$ by monitoring volumetric changes over time and survival outcomes – a single dose of $[^{177}\text{Lu}]\text{DUNP19}$ exhibited significant yet transient therapeutic effects while stable tumor volumes were achieved after multiple doses administered across course of treatment. RNA-sequencing analysis of $[^{177}\text{Lu}]\text{DUNP19}$ -treated tumor tissues revealed substantial depletion of the TGF β -driven LRRC15+ genetic signature. In addition, treatment with our LRRC15-targeted radioimmunotherapy upregulated transcripts of critical immunotherapy signature response genes, including CXCL10, CCL5, and IRF1. Together, these findings highlight the promise of $[^{177}\text{Lu}]\text{DUNP19}$ as a standalone modality and its potential to expand existing immunotherapy applications across indications as an adjuvant therapy. Finally, multiomics evaluations of TGF β 's regulation of LRRC15 reveal key LRRC15-related genes that may help stratify patients for LRRC15-targeted therapy.

1.3. Technologies

i. Single Cell RNA Sequencing

Single-cell RNA sequencing (scRNA-seq) offers a detailed analysis of specific or rare cell populations, revealing unique characteristics often masked in bulk transcriptomics. In cancer research, scRNA-seq enables high-resolution exploration of tumor stroma and cellular compartments, helping to identify heterogeneous cell populations within tumor tissue. In cancer

research, the technology allows for high resolution analyses of tumor stroma, cellular compartments, and individual cell types. For example, the technology has also been used to investigate specific immune cell populations that influence patient responses to immunotherapy [79]. By leveraging scRNA-seq, researchers can map the tumor transcriptome in detail, facilitating a deeper understanding of cell-cell interactions and regulatory networks involved in tumor pathology.

To analyze transcriptomes at the single-cell level, individual cells are encapsulated in oil-based droplets, which are then merged with beads carrying unique barcodes that serve as cell identifiers [80]. These beads capture cellular mRNA and reverse transcription reactions are performed, followed by library generation and sequencing. The transcript reads are later matched to their corresponding barcoded beads, providing a comprehensive transcriptomic profile for each cell [81].

Typically, the number of genes detected in scRNA-seq is lower compared to bulk RNA sequencing due to high levels of technical noise, dropout events, and a phenomenon known as transcriptional bursting. Transcriptional bursting refers to the variability in gene transcription kinetics and periods of transcriptional silence that individual cells may undergo after periods of gene transcription [82,83]. At the single-cell level, the transcriptional bursting phenomenon is more likely to be observed, often resulting in low gene counts. Additionally, scRNA-seq is affected by high cell-to-cell variability, as transcript expression can fluctuate depending on cell cycle stage or the health of individual cells [83]. Despite these limitations in gene detection, scRNA-seq excels at capturing cellular heterogeneity, identifying different cellular states, and

revealing gene co-expression patterns within populations. It is for this reason that we opted to perform scRNAseq over bulk RNA transcriptomics, as identifying the genes that were uniquely co-expressed with LRRC15 in TGF β -responsive cell lines would help us construct LRRC15's regulatory network.

To construct co-expression networks, robust quantitative methodologies are essential to capture unique biological features within cells and account for gene interactions. In this study, we employed two such methods: high-dimensional weighted gene co-expression network analysis (hdWGCNA) [84] and Single Cell INtegrative Gene regulatory network inference (SCING) [85]. hdWGCNA is an unsupervised clustering technique that generates metacells to avoid issues due to cell sparsity within subsets [84]. These metacells are similar in their transcriptomes and are typically representative of a cellular state. Pairwise correlations between genes are then calculated to estimate the strength of co-expression across metacells. Topological overlaps are computed to identify genes that are co-expressed with two highly correlated genes, and those with similar expression patterns are clustered into modules, which often represent larger biological processes [84].

Comparatively, SCING preprocesses data to filter out genes with low expression variability, focusing instead on highly variable genes [85]. Cells are similarly grouped to reduce cell sparsity into supercells, and average gene expression values are calculated from these supercells for downstream analysis. SCING then applies gradient boosting regression, a machine learning technique, to predict gene regulatory relationships. For example, Gene A's expression is predicted based on the expression of potential upstream regulators, identified as the 100 nearest

genes in a principal component analysis. These regulatory elements are then placed into gene regulatory networks to identify broader biological processes [85].

Both methods offer novel insights into single-cell transcriptomics by placing genes within larger regulatory (SCING) or co-expression (hdWGCNA) networks, allowing researchers to observe key biological phenomena. hdWGCNA can uncover novel gene interactions through unsupervised clustering, while SCING can account for regulatory interactions between genes and capture gene effects within a pathway. In this study, we employed both methods in our initial exploratory analysis of the TGFB-LRRC15 pathway to discover novel gene interactors with LRRC15 and to identify the regulatory elements and pathways involved in the TGFB-LRRC15 axis.

ii. Chemical Genomics

Phenotypic screens provide a valuable layer of functional information that can inform cancer cell mechanisms, identify lead compounds for drug discovery, and help establish mechanisms of resistance. Chemical genomics, or chemogenomics, studies a biological or molecular system using a compound library or set of small molecules. This approach is typically applied to investigate molecular mechanisms, identify biological targets, or aid in drug discovery. Before compound screening became a widely utilized technique in biological research, efficiency and capacity for assays conducted with a laboratory setting was severely limited both by quantity of assays performed, and by reagent limitations due to the large-volume reactions that were being utilized within those assays [86]. One of the earliest screens conducted by Pfizer's Natural Products Screening Group paved a path for improved efficiency and output in biological

research; by miniaturizing reactions to fit within a 96-well plate volume (100uL), they could simultaneously conduct soil fermentations for antibiotic discovery [86]. While prototype screens took many years to perfect, the screening approach paved the way for discoveries in oncology, microbiology, and virology. Today, chemical genomics expands on the fundamentals established by Pfizer's Screening Group and others, adapting small molecule compound libraries to study biological systems in a high-capacity manner.

Compound libraries are critical to a screen's success. Compound libraries can span drug classes or specialize to include a specific drug class (for example, kinase inhibitor libraries) depending on the researcher's question. A well-designed compound library includes compounds with the same target and orthogonal mechanisms of action or distinct chemical structures. This ensures that any phenotypic or biological effects observed are a result of on-target activity, providing secondary confirmation of a hit compound's mechanism [87]. The Sigma-Aldrich LOPAC1280 library comprises 1,280 compounds that target critical biological mechanisms and receptors, such as ion channels, G-proteins, and glucocorticoid signaling [88]. The library contains clinically relevant drugs, many of which are FDA-approved or have been evaluated in clinical trials, alongside standard compounds commonly used in screening libraries. Numerous chemogenomic screens have been conducted using the LOPAC library, including the identification of bone morphogenetic protein activators in cervical carcinoma cells and the discovery of key mechanisms regulating cytokine production in dendritic cells, critical for autoimmune processes [89,90].

A typical chemogenomics screen utilizes a biological system that closely replicates disease biology, enabling more accurate estimates of phenotypic responses to screened compounds. Establishing proper positive and negative controls is critical for the success of such screens. To assess the statistical power of a screen, a Z-factor can be calculated, which accounts for the variation within conditions of a screening plate, as well as the overall mean of the controls [91]. Before any analysis of compound-treated conditions, the plate's positive and negative controls are used to calculate a Z-factor and determine adequate separation of control conditions. A standard Z-factor calculation is as follows, with "POS" denoting the positive control, and "NEG" denoting the negative control:

$$Z = 1 - \frac{(3\sigma_{\text{POS}} + 3\sigma_{\text{NEG}})}{|\mu_{\text{POS}} - \mu_{\text{NEG}}|}$$

Z-factors below 0 indicate a poorly run screen that will yield no significant results. This typically arises from either large deviations within the control conditions or a small separation between the positive and negative controls, leading to a narrow window for any variability to be introduced. While a Z-factor can never equal 1, an ideal Z-factor is greater than 0.5, signifying that the separation between the positive and negative controls is sufficiently large and that intra-control variation is minimal [91].

Compound hit analysis can be performed similarly by assigning a Z-prime score to each compound-treated well. This score provides a normalized measure for each condition or

compound within the screened plate. The Z-prime score is calculated using the following formula, where "COMPOUND" represents the readout from the well of interest, and "PLATE" represents all readouts from compound-treated wells:

$$Z' = 1 - \frac{(3\sigma_{\text{COMPOUND}} + 3\sigma_{\text{PLATE}})}{|\mu_{\text{COMPOUND}} - \mu_{\text{PLATE}}|}$$

Antagonist screens, or screens probing for inhibition of a biological phenomenon, typically classify hits as those with a score three or more standard deviations from the mean, reaching a 99.73% confidence limit. Although initial compound libraries may be tested at high concentrations (ranging anywhere from 1-10 μM , depending on the compound library), it is essential to conduct dose-response studies on identified hits to confirm the potency of the compounds.

Once a list of hit compounds is generated, it is critical to investigate the mechanisms of action and chemical identities of the compounds to identify potential genes or pathways of interest. This can be achieved through various methods, one of the most common being the integration of hit compounds with established datasets. The L1000 platform offers a powerful tool for this, combining chemogenomics with sequencing of 1,000 landmark genes to assess the effects of small molecules on the transcriptomes of cancer cells [92]. Using the L1000 database, researchers can query genes, gene signatures, or compounds to identify matching gene signatures or biological pathways, offering additional context to the findings from

chemogenomic screens. Since many compounds in screening libraries have loosely defined mechanisms of action, the L1000 database can provide insights into the broader biological perturbations induced by compound treatment [92].

Finally, chemogenomic screens can be integrated with functional genomics to further validate biological mechanisms. Genes of interest that arise from compound hits can be silenced or overexpressed by functional genomic approaches such as CRISPR/Cas9, silencing RNA, or overexpression by cDNA plasmids [93]. These technologies provide critical loss-of-function and gain-of-function evidence, helping to solidify any biological mechanisms identified and refine the list of key compound hits for future analysis.

1.4. Conclusion

The primary focus of this thesis is to target biomarkers that are regulated by disease-driving pathobiological mechanisms. We provide evidence for non-invasive monitoring of the androgen receptor pathway and AR's critical downstream signaling mechanisms that driven aggressive prostate cancer. On the other hand, we also investigate the molecular interplay between TGF β signaling and LRRC15 expression, as well as to assess the potential of LRRC15-targeted radioimmunotherapy to eliminate TGF β -driven tumor cell populations before exploring the genomic and tumor microenvironmental consequences of LRRC15-targeted therapy. Through a combination of high-content screening, single-cell RNA sequencing, and in vitro and in vivo studies, this work aims to identify key molecular drivers of LRRC15 overexpression and to evaluate the therapeutic impact of disrupting the TGF β -LRRC15 axis. By uncovering the

molecular signatures associated with therapeutic resistance and developing predictive gene signatures linked to patient outcomes, this research provides novel insights into how targeted radioimmunotherapy can be optimized for improved efficacy in TGF β -driven malignancies. Furthermore, these findings emphasize the broader significance of dissecting the molecular biology of therapeutic targets to enhance the precision and effectiveness of cancer treatments. By establishing the capability of RIT-based non-invasive monitoring of signaling pathways such as AR with conventional models of prostate cancer, we can extrapolate these techniques into future LRRC15-targeted treatment for monitoring TGF β -driven disease.

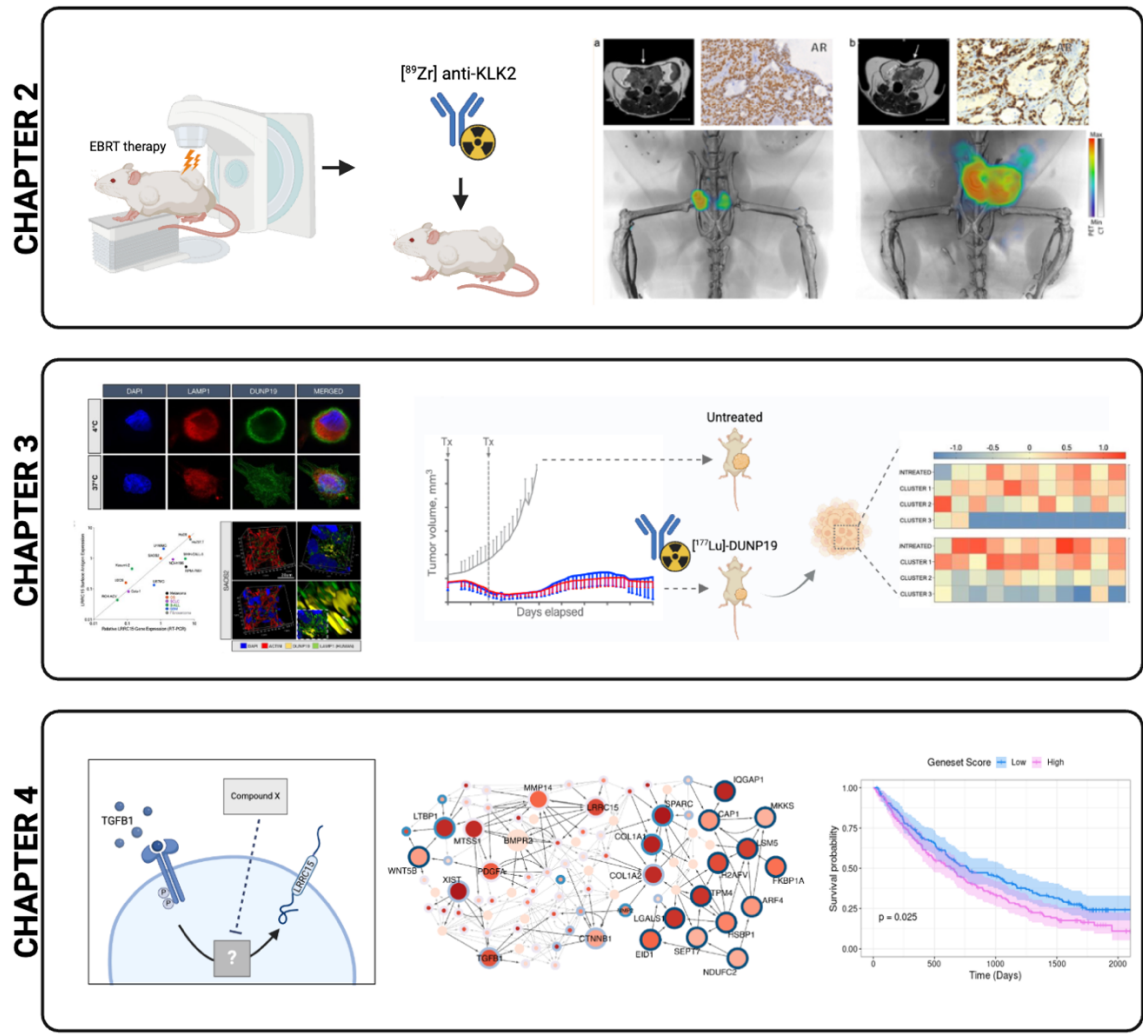


Figure 1. Dissertation Overview

1.5 References

1. Kothari M, Wanjari A, Acharya S, et al. A Comprehensive Review of Monoclonal Antibodies in Modern Medicine: Tracing the Evolution of a Revolutionary Therapeutic Approach. *Cureus*. 2024; 16(6):e61983.
2. Malm M, Kuo CC, Barzadd MM, et al. Harnessing secretory pathway differences between HEK293 and CHO to rescue production of difficult to express proteins. *Metab Eng*. 2022; 72:171-187.

3. Morrison SL, Johnson MJ, Herzenberg LA, Oi VT. Chimeric human antibody molecules: mouse antigen-binding domains with human constant region domains. *Proc Natl Acad Sci U S A*. 1984; 81(21):6851-5.
4. Hosono M, Endo K, Sakahara H, et al. Human/mouse chimeric antibodies show low reactivity with human anti-murine antibodies (HAMA). *Br J Cancer*. 1992; 65(2):197-200.
5. Jones PT, Dear PH, Foote J, Neuberger MS, Winter G. Replacing the complementarity-determining regions in a human antibody with those from a mouse. *Nature*. 1986; 321(6069):522-5.
6. Wu AM. Engineered antibodies for molecular imaging of cancer. *Methods*. 2014; 65(1):139-47.
7. Bournazos S, Wang TT, Dahan R, Maamary J, Ravetch JV. Signaling by Antibodies: Recent Progress. *Annu Rev Immunol*. 2017; 35:285-311.
8. Simpson TR, Li F, Montalvo-Ortiz W, et al. Fc-dependent depletion of tumor-infiltrating regulatory T cells co-defines the efficacy of anti-CTLA-4 therapy against melanoma. *J Exp Med*. 2013; 210(9):1695-710.
9. Vidarsson G, Dekkers G, Rispens T. IgG subclasses and allotypes: from structure to effector functions. *Front Immunol*. 2014; 5:520.
10. Keizer RJ, Huitema AD, Schellens JH, Beijnen JH. Clinical pharmacokinetics of therapeutic monoclonal antibodies. *Clin Pharmacokinet*. 2010; 49(8):493-507.
11. Westrøm S, Bønsdorff TB, Abbas N, et al. Evaluation of CD146 as Target for Radioimmunotherapy against Osteosarcoma. *PLoS One*. 2016; 11(10):e0165382.
12. Stapleton NM, Andersen JT, Stemerding AM, et al. Competition for FcRn-mediated transport gives rise to short half-life of human IgG3 and offers therapeutic potential. *Nat Commun*. 2011; 2:599.
13. Buss NA, Henderson SJ, McFarlane M, Shenton JM, de Haan L. Monoclonal antibody therapeutics: history and future. *Curr Opin Pharmacol*. 2012; 12(5):615-22.
14. Dumontet C, Reichert JM, Senter PD, Lambert JM, Beck A. Antibody-drug conjugates come of age in oncology. *Nat Rev Drug Discov*. 2023; 22(8):641-661.
15. Haefliger P, Agorastos N, Renard A, Giambonini-Brugnoli G, Marty C, Alberto R. Cell uptake and radiotoxicity studies of an nuclear localization signal peptide-

- intercalator conjugate labeled with $[^{99m}\text{Tc}(\text{CO})_3]^+$. *Bioconjug Chem.* 2005; 16(3):582-7.
16. Ismail IH, Nyström S, Nygren J, Hammarsten O. Activation of ataxia telangiectasia mutated by DNA strand break-inducing agents correlates closely with the number of DNA double strand breaks. *J Biol Chem.* 2005; 280(6):4649-55.
 17. Song H, Sgouros G. Radioimmunotherapy of solid tumors: searching for the right target. *Curr Drug Deliv.* 2011; 8(1):26-44.
 18. Goldenberg DM, DeLand F, Kim E, et al. Use of radiolabeled antibodies to carcinoembryonic antigen for the detection and localization of diverse cancers by external photoscanning. *N Engl J Med.* 1978; 298(25):1384-6.
 19. Press OW, Eary JF, Badger CC, et al. Treatment of refractory non-Hodgkin's lymphoma with radiolabeled MB-1 (anti-CD37) antibody. *J Clin Oncol.* 1989; 7(8):1027-38.
 20. Eary JF, Press OW, Badger CC, et al. Imaging and treatment of B-cell lymphoma. *J Nucl Med.* 1990; 31(8):1257-68.
 21. Larson SM, Pentlow KS, Volkow ND, et al. PET scanning of iodine-124-3F9 as an approach to tumor dosimetry during treatment planning for radioimmunotherapy in a child with neuroblastoma. *J Nucl Med.* 1992; 33(11):2020-3.
 22. Köhler G, Milstein C. Continuous cultures of fused cells secreting antibody of predefined specificity. *Nature.* 1975; 256(5517):495-7.
 23. Goldsmith SJ. Radioimmunotherapy of lymphoma: Bexxar and Zevalin. *Semin Nucl Med.* 2010; 40(2):122-35.
 24. Quackenbush RC, Horner TJ, Williams VC, Giampietro P, Lin TS. Patients with relapsed follicular lymphoma treated with rituximab versus tositumomab and iodine I-131 tositumomab. *Leuk Lymphoma.* 2015;56(3):779-781.
 25. Press OW, Unger JM, Rimsza LM, et al. Phase III randomized intergroup trial of CHOP plus rituximab compared with CHOP chemotherapy plus ^{131}I -tositumomab for previously untreated follicular non-Hodgkin lymphoma: SWOG S0016. *J Clin Oncol.* 2013; 31(3):314-20.

26. Response-Adapted Postinduction Strategy in Patients With Advanced-Stage Follicular Lymphoma: The FOLL12 Study. ClinicalTrials.gov identifier: NCT02063685
27. A Multicenter, Open Label, Phase II Study of Bendamustine and Rituximab followed by 90-yttrium (Y) Ibritumomab Tiuxetan for Untreated Follicular Lymphoma ClinicalTrials.gov identifier: NCT01234766
28. Positron Emission Tomography–Directed Therapy for Patients With Limited-Stage Diffuse Large B-Cell Lymphoma: Results of Intergroup National Clinical Trials Network Study S1001. ClinicalTrials.gov identifier: NCT01359592
29. Rizzieri D. Zevalin(®) (ibritumomab tiuxetan): After more than a decade of treatment experience, what have we learned? *Crit Rev Oncol Hematol.* 2016; 105:5-17.
30. Witzig TE, Gordon LI, Cabanillas F, et al. Randomized controlled trial of yttrium-90-labeled ibritumomab tiuxetan radioimmunotherapy versus rituximab immunotherapy for patients with relapsed or refractory low-grade, follicular, or transformed B-cell non-Hodgkin's lymphoma. *J Clin Oncol.* 2002; 20(10):2453-63.
31. Persky DO, Li H, Stephens DM, et al. Positron Emission Tomography-Directed Therapy for Patients With Limited-Stage Diffuse Large B-Cell Lymphoma: Results of Intergroup National Clinical Trials Network Study S1001. *J Clin Oncol.* 2020; 38(26):3003-3011.
32. Riaz A, Lewandowski RJ, Kulik LM, et al. Complications following radioembolization with yttrium-90 microspheres: a comprehensive literature review. *J Vasc Interv Radiol.* 2009; 20(9):1121-30; quiz 1131.
33. Ferreira CA, Fuscaldi LL, Townsend DM, Rubello D, Barros ALB. Radiolabeled bombesin derivatives for preclinical oncological imaging. *Biomed Pharmacother.* 2017;87:58-72. doi:10.1016/j.biopha.2016.12.083
34. ARPANSA. Alpha Particles. ARPANSA. Published May 23, 2019. <https://www.arpansa.gov.au/understanding-radiation/what-is-radiation/ionising-radiation/alpha-particles>
35. Ku A, Facca VJ, Cai Z, Reilly RM. Auger electrons for cancer therapy - a review. *EJNMMI Radiopharm Chem.* 2019; 4(1):27.

36. Bartholomä MD, Louie AS, Valliant JF, Zubieta J. Technetium and gallium derived radiopharmaceuticals: comparing and contrasting the chemistry of two important radiometals for the molecular imaging era. *Chem Rev.* 2010; 110(5):2903-20.
37. Chomet M, van Dongen GAMS, Vugts DJ. State of the Art in Radiolabeling of Antibodies with Common and Uncommon Radiometals for Preclinical and Clinical Immuno-PET. *Bioconjug Chem.* 2021; 32(7):1315-1330.
38. Sheyi R, de la Torre BG, Albericio F. Linkers: An Assurance for Controlled Delivery of Antibody-Drug Conjugate. *Pharmaceutics.* 2022; 14(2):.
39. Ducry L, Stump B. Antibody-drug conjugates: linking cytotoxic payloads to monoclonal antibodies. *Bioconjug Chem.* 2010; 21(1):5-13.
40. Testing a New Imaging Agent to Identify Cancer. *ClinicalTrials.gov* identifier: NCT04692831
41. Berg EA, Fishman JB. Iodination of Antibodies with Immobilized Iodogen. *Cold Spring Harb Protoc.* 2020; 2020(7):099341.
42. Goldenberg DM. *Cancer Therapy with Radiolabeled Antibodies.* Informa; 2018. doi:<https://doi.org/10.1201/9781351070409>
43. De Nardo GL, De Nardo SJ, Miyao NP, et al. Non-dehalogenation mechanisms for excretion of radioiodine after administration of labeled antibodies. *Int J Biol Markers.* 1988; 3(1):1-9.
44. Xenaki KT, Oliveira S, van Bergen En Henegouwen PMP. Antibody or Antibody Fragments: Implications for Molecular Imaging and Targeted Therapy of Solid Tumors. *Front Immunol.* 2017; 8:1287.
45. Roopenian DC, Akilesh S. FcRn: the neonatal Fc receptor comes of age. *Nat Rev Immunol.* 2007; 7(9):715-25.
46. Pyzik M, Sand KMK, Hubbard JJ, Andersen JT, Sandlie I, Blumberg RS. The Neonatal Fc Receptor (FcRn): A Misnomer? *Front Immunol.* 2019; 10:1540.
47. Walter RB, Press OW, Pagel JM. Pretargeted radioimmunotherapy for hematologic and other malignancies. *Cancer Biother Radiopharm.* 2010;25(2):125-142.
48. Navarro-Teulon I, Lozza C, Pèlerin A, Vivès E, Pouget JP. General overview of radioimmunotherapy of solid tumors. *Immunotherapy.* 2013; 5(5):467-87.

49. Larson SM, Carrasquillo JA, Cheung NK, Press OW. Radioimmunotherapy of human tumours. *Nat Rev Cancer*. 2015; 15(6):347-60.
50. Zhang Y, Hong H, Cai W. PET tracers based on Zirconium-89. *Curr Radiopharm*. 2011; 4(2):131-9.
51. Crişan G, Moldovean-Cioroianu NS, Timaru DG, Andrieş G, Căinap C, Chiş V. Radiopharmaceuticals for PET and SPECT Imaging: A Literature Review over the Last Decade. *Int J Mol Sci*. 2022; 23(9):.
52. van Es SC, Brouwers AH, Mahesh SVK, et al. (89)Zr-Bevacizumab PET: Potential Early Indicator of Everolimus Efficacy in Patients with Metastatic Renal Cell Carcinoma. *J Nucl Med*. 2017; 58(6):905-910.
53. Robb MA, McInnes PM, Califf RM. Biomarkers and Surrogate Endpoints: Developing Common Terminology and Definitions. *JAMA*. 2016; 315(11):1107-8.
54. Safety and Targeting of Anti-hk2 Antibody in mCRPC. *ClinicalTrials.gov* identifier: NCT04116164.
55. Martin FC, Dorff TB, Tran B. The new era of prostate-specific membrane antigen-directed immunotherapies and beyond in advanced prostate cancer: a review. *Ther Adv Med Oncol*. 2023; 15:17588359231170474.
56. McDevitt MR, Thorek DLJ, Hashimoto T, et al. Feed-forward alpha particle radiotherapy ablates androgen receptor-addicted prostate cancer. *Nat Commun*. 2018; 9(1):1629.
57. Timmermand OV, Ulmert D, Evans-Axelsson S, et al. Preclinical imaging of kallikrein-related peptidase 2 (hK2) in prostate cancer with a (111)In-radiolabelled monoclonal antibody, 11B6. *EJNMMI Res*. 2014; 4(1):51.
58. Bhowmick NA, Chytil A, Plieth D, et al. TGF-beta signaling in fibroblasts modulates the oncogenic potential of adjacent epithelia. *Science*. 2004; 303(5659):848-51.
59. Derynck R, Turley SJ, Akhurst RJ. TGFβ biology in cancer progression and immunotherapy. *Nat Rev Clin Oncol*. 2021; 18(1):9-34.
60. Massagué J. TGFbeta in Cancer. *Cell*. 2008; 134(2):215-30.
61. Biswas T, Gu X, Yang J, Ellies LG, Sun LZ. Attenuation of TGF-β signaling supports tumor progression of a mesenchymal-like mammary tumor cell line in a syngeneic murine model. *Cancer Lett*. 2014; 346(1):129-38.

62. Connolly EC, Saunier EF, Quigley D, et al. Outgrowth of drug-resistant carcinomas expressing markers of tumor aggression after long-term T β RI/II kinase inhibition with LY2109761. *Cancer Res.* 2011; 71(6):2339-49.
63. Orimo A, Gupta PB, Sgroi DC, et al. Stromal fibroblasts present in invasive human breast carcinomas promote tumor growth and angiogenesis through elevated SDF-1/CXCL12 secretion. *Cell.* 2005; 121(3):335-48.
64. Olumi AF, Grossfeld GD, Hayward SW, Carroll PR, Tlsty TD, Cunha GR. Carcinoma-associated fibroblasts direct tumor progression of initiated human prostatic epithelium. *Cancer Res.* 1999; 59(19):5002-11.
65. Quante M, Tu SP, Tomita H, et al. Bone marrow-derived myofibroblasts contribute to the mesenchymal stem cell niche and promote tumor growth. *Cancer Cell.* 2011; 19(2):257-72.
66. Zhang XH, Jin X, Malladi S, et al. Selection of bone metastasis seeds by mesenchymal signals in the primary tumor stroma. *Cell.* 2013; 154(5):1060-1073.
67. Mariathasan S, Turley SJ, Nickles D, et al. TGF β attenuates tumour response to PD-L1 blockade by contributing to exclusion of T cells. *Nature.* 2018; 554(7693):544-548.
68. Kraman M, Bambrough PJ, Arnold JN, et al. Suppression of antitumor immunity by stromal cells expressing fibroblast activation protein- α . *Science.* 2010; 330(6005):827-30.
69. Su S, Chen J, Yao H, et al. CD10(+)GPR77(+) Cancer-Associated Fibroblasts Promote Cancer Formation and Chemoresistance by Sustaining Cancer Stemness. *Cell.* 2018; 172(4):841-856.e16.
70. Ohuchida K, Mizumoto K, Murakami M, et al. Radiation to stromal fibroblasts increases invasiveness of pancreatic cancer cells through tumor-stromal interactions. *Cancer Res.* 2004; 64(9):3215-22.
71. Hirata E, Girotti MR, Viros A, et al. Intravital imaging reveals how BRAF inhibition generates drug-tolerant microenvironments with high integrin β 1/FAK signaling. *Cancer Cell.* 2015; 27(4):574-88.

72. Straussman R, Morikawa T, Shee K, et al. Tumour micro-environment elicits innate resistance to RAF inhibitors through HGF secretion. *Nature*. 2012; 487(7408):500-4.
73. Mueller KL, Madden JM, Zoratti GL, Kuperwasser C, List K, Boerner JL. Fibroblast-secreted hepatocyte growth factor mediates epidermal growth factor receptor tyrosine kinase inhibitor resistance in triple-negative breast cancers through paracrine activation of Met. *Breast Cancer Res*. 2012; 14(4):R104.
74. Purcell JW, Tanlimco SG, Hickson J, et al. LRRC15 Is a Novel Mesenchymal Protein and Stromal Target for Antibody-Drug Conjugates. *Cancer Res*. 2018; 78(14):4059-4072.
75. Dominguez CX, Müller S, Keerthivasan S, et al. Single-Cell RNA Sequencing Reveals Stromal Evolution into LRRC15(+) Myofibroblasts as a Determinant of Patient Response to Cancer Immunotherapy. *Cancer Discov*. 2020; 10(2):232-253.
76. Krishnamurty AT, Shyer JA, Thai M, et al. LRRC15(+) myofibroblasts dictate the stromal setpoint to suppress tumour immunity. *Nature*. 2022; 611(7934):148-154.
77. Hingorani P, Roth ME, Wang Y, et al. ABBV-085, Antibody-Drug Conjugate Targeting LRRC15, Is Effective in Osteosarcoma: A Report by the Pediatric Preclinical Testing Consortium. *Mol Cancer Ther*. 2021; 20(3):535-540.
78. Ben-Ami E, Perret R, Huang Y, et al. LRRC15 Targeting in Soft-Tissue Sarcomas: Biological and Clinical Implications. *Cancers (Basel)*. 2020; 12(3):
79. Zheng L, Qin S, Si W, et al. Pan-cancer single-cell landscape of tumor-infiltrating T cells. *Science*. 2021; 374(6574):abe6474.
80. Kim IS. Single-Cell Molecular Barcoding to Decode Multimodal Information Defining Cell States. *Mol Cells*. 2023; 46(2):74-85.
81. Macosko EZ, Basu A, Satija R, et al. Highly Parallel Genome-wide Expression Profiling of Individual Cells Using Nanoliter Droplets. *Cell*. 2015; 161(5):1202-1214.
82. Suter DM, Molina N, Gatfield D, Schneider K, Schibler U, Naef F. Mammalian genes are transcribed with widely different bursting kinetics. *Science*. 2011; 332(6028):472-4.

83. Haque A, Engel J, Teichmann SA, Lönnberg T. A practical guide to single-cell RNA-sequencing for biomedical research and clinical applications. *Genome Med.* 2017; 9(1):75.
84. Morabito S, Reese F, Rahimzadeh N, Miyoshi E, Swarup V. hdWGCNA identifies co-expression networks in high-dimensional transcriptomics data. *Cell Rep Methods.* 2023; 3(6):100498.
85. Littman R, Cheng M, Wang N, Peng C, Yang X. SCING: Inference of robust, interpretable gene regulatory networks from single cell and spatial transcriptomics. *iScience.* 2023; 26(7):107124.
86. Pereira DA, Williams JA. Origin and evolution of high throughput screening. *Br J Pharmacol.* 2007; 152(1):53-61.
87. Bunnage ME, Chekler EL, Jones LH. Target validation using chemical probes. *Nat Chem Biol.* 2013; 9(4):195-9.
88. Sigma Aldrich. Gold Nanoparticles: Properties and Applications. Merck. 2024;1(1). <https://www.sigmaaldrich.com/MX/en/technical-documents/technical-article/genomics/cloning-and-expression/blue-white-screening>
89. Vrijens K, Lin W, Cui J, et al. Identification of small molecule activators of BMP signaling. *PLoS One.* 2013; 8(3):e59045.
90. Chen S, Zhou J, Cai Y, et al. Discovery of BVDU as a promising Drug for autoimmune diseases Therapy by Dendritic-cell-based functional screening. *Sci Rep.* 2017; 7:43820.
91. Zhang JH, Chung TD, Oldenburg KR. A Simple Statistical Parameter for Use in Evaluation and Validation of High Throughput Screening Assays. *J Biomol Screen.* 1999; 4(2):67-73.
92. Subramanian A, Narayan R, Corsello SM, et al. A Next Generation Connectivity Map: L1000 Platform and the First 1,000,000 Profiles. *Cell.* 2017; 171(6):1437-1452.e17.
93. Boettcher M, McManus MT. Choosing the Right Tool for the Job: RNAi, TALEN, or CRISPR. *Mol Cell.* 2015; 58(4):575-85.

CHAPTER 2. KLK2 AS A PATHOBIOLOGICAL THERAPEUTIC TARGET IN PROSTATE CANCER

Non-invasive biomarkers for androgen receptor (AR) pathway activation are urgently needed to better monitor patient response to prostate cancer (PCa) therapies. AR is a critical driver and mediator of resistance of PCa but currently available non-invasive PCa biomarkers to monitor AR activity are discordant with downstream AR pathway activity. External beam radiotherapy (EBRT) remains a common treatment for all stages of PCa, and DNA damage induced by EBRT upregulates AR pathway activity to promote therapeutic resistance. [⁸⁹Zr]11B6-PET is a novel modality targeting prostate-specific protein human kallikrein 2 (hK2), which is a surrogate biomarker for AR activity. Here, we studied if [⁸⁹Zr]11B6-PET can accurately assess EBRT-induced AR activity. Genetic and human PCa mouse models received EBRT (2–50 Gy) and treatment response was monitored by [⁸⁹Zr]11B6-PET/CT. Radiotracer uptake and expression of AR and AR target genes was quantified in resected tissue. EBRT increased AR pathway activity and [⁸⁹Zr]11B6 uptake in LNCaP-AR and 22RV1 tumors. EBRT increased prostate-specific [⁸⁹Zr]11B6 uptake in PCa-bearing mice (Hi-Myc x Pb_KLK2) with no significant changes in uptake in healthy (Pb_KLK2) mice, and this correlated with hK2 protein levels.

Adapted from “Quantitative In Vivo Imaging of the Androgen Receptor Axis Reveals Degree of Prostate Cancer Radiotherapy Response”

Claire M Storey, Mohamed Altai, Mesude Bicak, Darren R Veach, Katharina Lückerrath, Gabriel Adrian, Michael R McDevitt, Teja Kalidindi, Julie E Park, Ken Herrmann, Diane Abou, Wahed Zedan, Norbert Peekhaus, Robert J Klein, Robert Damoiseaux, Steven M Larson, Hans Lilja, Daniel Thorek, David Ulmert

CMS, MA, MB, DRV, KL, DT, DU: writing, review and editing, formal analysis

MA, DRV, KL, DT, DU: data collection

GA, MRD, TK, JEP, KH, DA, WZ, NP, RJK, RD, SL, HL: review and editing

DT, DU: conceptualization

2.1 Introduction

External beam radiotherapy (EBRT), a mainstay in prostate cancer therapy, activates androgen receptor (AR); this increases the expression of DNA repair genes, which may promote radioresistance [1-4] and explain the synergy between ionizing radiation and AR signaling inhibitors (ARSI) [5,6]. Noninvasive biomarkers for monitoring DNA damage–induced AR activity may allow monitoring response to EBRT and early detection of treatment resistance, and thus, providing patients with prostate cancer with individualized treatment options. In the clinical setting, AR activity is currently monitored through the assessment of serum PSA (*KLK3*) levels over time [7]. However, measurements of serum kallikreins provide limited information as they reflect a global average of multiple heterogenic lesions in the metastatic setting with limited correlation to protein production [8]. The development of imaging-based response criteria [RECIST, positron emission tomography response criteria in solid tumors (PERCIST)] reflects this challenge; the increasing application of RECIST/PERCIST for assessing response (to radionuclide therapies)—for example in the VISION trial, in which blood PSA levels were a secondary endpoint only—supports the relevance of these criteria. The capacity to decipher which lesions at which anatomic sites respond and which do not respond would significantly augment future patient management.

Similar to PSA, human kallikrein 2 (hK2; *KLK2*) is a prostate gland-specific and cancer cell-specific trypsin-like serine protease that is tightly governed by the functional status of the AR hormone response circuit, and is elevated in the serum of >20% of patients following EBRT [9]. We previously developed 11B6, an IgG1 antibody with high selectivity and specificity for the active cleavage site of hK2. 11B6 uniquely binds to hK2 directly at the cell surface—that is, at the site of hK2 production and thus, AR activity—and avoids interaction with serum kallikreins. When derivatized with medically relevant radionuclides, this platform can be used for radioimmunotheranostics for detection, delineation, and treatment of diverse models of AR-expressing adenocarcinoma [10-12]. PET with [⁸⁹Zr]11B6 enables monitoring of prostate cancer growth and quantification of lesion-specific AR activity [10-12].

We hypothesize that [⁸⁹Zr]11B6-PET can be used to noninvasively monitor EBRT-induced changes in AR activity in individual prostate cancer lesions. Using quantitative imaging and genomic analyses of human xenograft and genetically engineered mouse models of prostate cancer, EBRT-induced AR activity was visualized and correlated to transcriptomic alterations following therapy with near-term implications for prostate cancer treatment paradigms.

2.2 Materials and Methods

2.2.1 Radiochemistry

Radiosynthesis of [⁸⁹Zr]-DFO-11B6 ([⁸⁹Zr]11B6) has been described previously [13]. 11B6 antibody was provided by Dr. Kim Pettersson, University of Turku, Turku, Finland. All labeling reactions achieved >99% radiochemical purity. Average specific activity of the final radiolabeled conjugate was 51.8 MBq/mg (1.4 mCi/mg).

2.2.2 Cell Lines

22Rv1 cells were purchased from ATCC. LNCaP-AR (LNCaP with overexpression of wildtype AR) was a kind gift from Charles Sawyers [14]. Cells were cultured according to the providers' instructions and frequently tested for *Mycoplasma* contamination. Cell lines were authenticated using GenePrint10 short tandem repeat analysis (Laragen Inc).

2.2.3 Mouse Models

All animal experiments were conducted in compliance with Memorial Sloan Kettering Cancer Center (MSKCC) guidelines, Institutional Animal Care and Use Committee-established guidelines, and RARC animal protocol (# 04-01-002). Xenografts were established in male athymic BALB/c (nu/nu) mice (6–8 weeks old, 20–25 g; Charles River) by subcutaneous injection of LNCaP-AR or 22Rv1 cells ($1-5 \times 10^6$ cells, 1:1 = media: Matrigel). Tumors developed after 3–7 weeks. The transgenic prostate cancer mouse models used, Hi-*Myc* × Pb-*KLK2* with prostate-specific AR-driven hK2 expression, as well as Pb-*KLK2* mice with abundant AR-driven hK2 expression specific to murine prostate tissue, have been reported previously [15]. Irradiated animals ranged from 35 to 42 weeks at study outset.

2.2.4 EBRT

Irradiation of disease sites was performed as described previously [15]. Briefly, a whole-body CT was acquired (XRad225Cx, Precision X-Ray, Inc.; dual focal spot x-ray tube at 45 kVp with a flat-panel amorphous silicon imager mounted on a C-arm gantry), tumor fields were identified and a treatment plan with >3 angles and a dose rate of approximately 3 Gy/minute (tube voltage, 225 kVp) was devised. Radiation dosimetry was performed using Gafchromic EBT film (ISP

Inc.); a clear film that polymerizes with increasing optical density to a degree linearly with dose. The Gafchromic film verified the targeting accuracy, the magnitude of dose delivered and the geometry of the planned dose plan.

2.2.5 MRI

Prostate tumor volumes were defined using T2-weighted MR scans (Bruker BioSpin 4.7 T). An interleaved T2-weighted turbo spin echo sequence (3,200/57.1) with 8 averages was used, with slice dimensions of $8.5 \times 3.99 \times 0.8$ cm. A total scan duration of 10 minutes, 14 seconds generated 220 and 800 μm in and out of plane slices, respectively. A trained reader calculated prostate volumes by segmenting the prostate (OsiriX, v8.1) [16].

2.2.6 Bioluminescence Imaging

Activity of the AR-dependent reporter construct expressed in LNCaP-AR tumors was quantified by bioluminescence imaging (Living Image 4.5.2) following retro-orbital injection of D-Luciferin (30 mg/mL, 10 μL ; exposure times 1, 5, 10, 20, and 40 seconds). Data were expressed as radiance (photons/second) divided by tumor volume measured by caliper ($V = \text{length} \times \text{width}^2$).

2.2.7 Impact of EBRT on [⁸⁹Zr]11B6 tumor uptake

Mice bearing LNCaP-AR and 22Rv1 xenografts, and Hi-*Myc* \times Pb-*KLK2* and Pb-*KLK2* mice, received [⁸⁹Zr]11B6 [3.7–5.55 MBq (100–150 μCi), 25 μg protein, i.v.; $t = 0$ hour], after EBRT ($n = 4\text{--}5/\text{group}$). To confirm specificity, a control group of mice with 22Rv1 tumors treated with 4×5 Gy was coinjected with 1 mg of unlabeled 11B6. [⁸⁹Zr] radioactivity in tumors and organs harvested 120 hours post-injection (p.i.) was quantified using a gamma-counter. Data were

background and decay corrected, and the percentage injected activity per gram tissue (%IA/g) was calculated.

2.2.8 Monitoring AR activity using PET/CT

PET/CT imaging (Inveon MM, IRW Acquisition software) was performed as described previously [19], at 120 hours p.i. with Hi-*Myc* × Pb-*KLK2* following administration of [⁸⁹Zr]11B6 [3.7–5.55 MBq (100–150 μCi), 25 μg of protein, i.v.]. Duration of PET scans were approximately 1 hour or until 20×10^6 coincident events were recorded. A three-dimensional maximum *a priori* reconstruction was used to generate tomographic datasets. Assessment of hK2 expression for correlation with [⁸⁹Zr]11B6 uptake was reported previously [17].

2.2.9 Histology

Prostate tissues of Hi-*Myc* × Pb-*KLK2* and Pb-*KLK2* mice harvested after EBRT (5×10 Gy) were fixed in 4% paraformaldehyde and cut into 15 μm sections before staining with hematoxylin and eosin. IHC for detection of AR and c-Myc was performed at the Molecular Cytology Core Facility (MSKCC) using a Discovery XT processor (Ventana Medical Systems). Sections were blocked in 10% normal goat serum in PBS for 30 minutes before staining with an anti-AR (N-20) antibody (1 μg/mL, 3 hours; Santa Cruz Biotechnology, #SC-816; secondary: biotinylated goat anti-rabbit IgG, 1:200, 16 minutes; Vector labs, #PK6101), or an anti-c-Myc antibody (1:100, 5 hours; Epitomics, #P01106; secondary: biotinylated goat anti-rabbit IgG, 1:200, 1 hour; Vector labs, #PK6101). Blocker D, Streptavidin-HRP, and DAB detection kit (Ventana Medical Systems) were used according to the manufacturer's instructions.

2.2.10 Gene Expression Analysis

RNA was purified using the RNeasy Mini Kit (Qiagen), and qPCR to determine expression of *KLK2*, *KLK3*, and *FOLH1* was performed as described previously.

For RNA sequencing, raw read count RNA-sequencing data were generated from untreated (NT; $n = 3$) LNCaP-AR tumor samples and 5×10 Gy ($n = 3$) treated samples. A total of 58,828 genes were acquired and analyzed as reported previously [17]. Both hierarchical clustering analysis (based on Euclidean distance) and multidimensional scaling plots demonstrated a clear division between the samples from the two cohorts (Supplementary Fig. S1 and S2). Differentially expressed genes (DEG) were defined at an adjusted $P < 0.001$ and an absolute value of \log_2 fold change >1 . A positive fold change represented upregulation and a negative fold change represented downregulation in EBRT-treated tumors. Pathway analysis was performed using enrichR [18] and the Kyoto Encyclopedia of Genes and Genomes 2021 database.

2.2.11 Statistical Analysis

Statistical significance was determined by unpaired two-tailed t test (two groups) or, for >2 groups, by one-way ANOVA followed by Dunnett test to correct for multiple comparisons and set to $P < 0.05$. Data are presented as mean \pm SD. Analysis was performed with GraphPad Prism Version 9.2.0. For RNA sequencing, differentially expressed genes were considered significant with an adjusted $P < 0.001$ and \log_2 fold change >1 as described previously [17].

2.2.12 Data Availability

The RNA-sequencing data reported in this article have been deposited in the Gene Expression Omnibus database, <https://www.ncbi.nlm.nih.gov/geo> (accession no. GSE206847). Other data generated in this study are available upon request from the corresponding author.

2.3 Changes in AR and AR-driven prostate cancer biomarkers in response to EBRT

PCR analysis of LNCaP-AR tumors treated with 1, 3, or 5 fractions of 2, 5, or 10 Gy EBRT revealed dose-dependent increases in *AR*, *KLK2*, and *KLK3* compared with nontreated (NT) controls (Fig. 1; Table 1). *FOLH1* expression after EBRT varied and remained unchanged under EBRT (Fig. 1B; Table 1). After three cycles of EBRT in 22Rv1 xenografts, *AR* gene expression was significantly increased along with *KLK2* and *KLK3*, while there were no significant changes in *FOLH1* expression (Fig. 1C; Table 1). The fold change of AR transcription was higher in 22Rv1 than LNCaP-AR tumors, which is likely an effect of lower baseline AR expression in the 22Rv1 model. This outcome corresponds with previously reported findings and provides additional support for the correlation between *KLK2* and *AR* expression when monitoring changes rendered by EBRT [9].

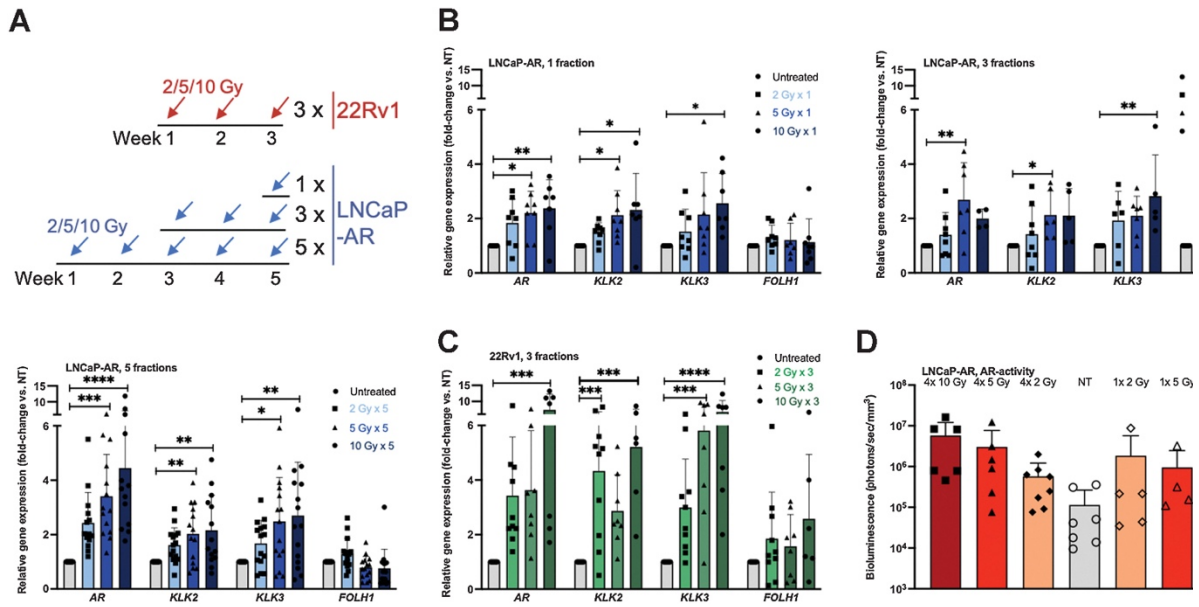
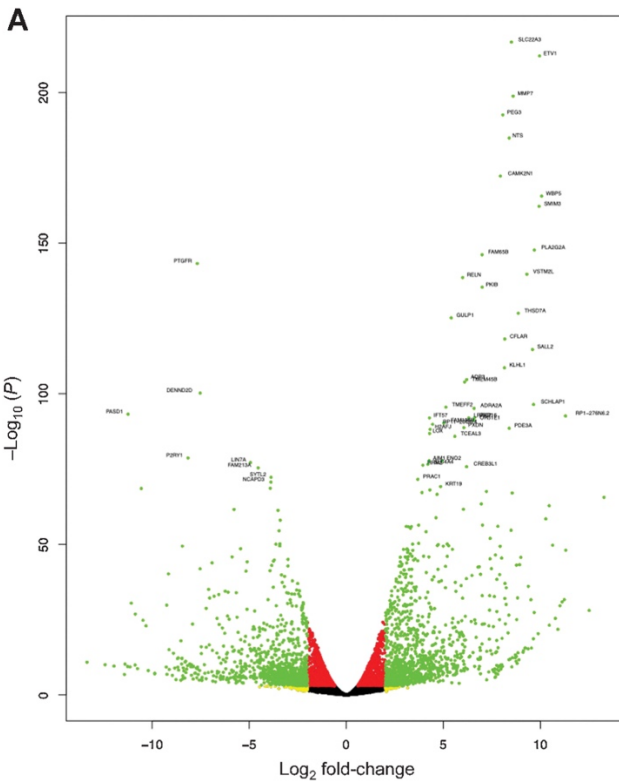


Figure 1. AR activity and gene expression after EBRT in LNCaP-AR and 22Rv1 xenografts. (A) Schematic of EBRT fractionation regimen. Gene expression analysis of LNCaP-AR (B) and 22Rv1 (C) xenografts after 1, 3, and 5 fractions of 2, 5 or 10 Gy EBRT revealed upregulation of *AR* and *KLK2/KLK3* in a dose-dependent manner. Data were normalized to NT. See Table 1 for mean and p-values. Bioluminescence imaging readout of AR activity in LNCaP-AR xenografts after 1 or 4 fractions of EBRT revealed dose-dependent increase in AR activity independent of fractionation (all p=not significant vs. NT). Mean \pm SD and individual values are given; statistical significance was calculated using one-way ANOVA and Dunnett's test for multiple comparisons.

Investigating EBRT-induced transcriptomic changes in an unbiased approach, 4,851 DEGs (8.2% of transcriptome gene set) were identified in LNCaP-AR tumors after EBRT (5 \times 10 Gy; vs. NT); 2,552 genes were upregulated and 2,299 were downregulated (Fig. 2). Upregulation of AR-regulated genes such as AR signaling coactivator *ETV1* (20), *KLK2*, and *KLK3* (log₂ fold

change = 10.01, 1.033, 1.882) indicated that AR signaling was increased after EBRT. Interestingly, other AR target genes, including *TMPRSS2* and *FKBP5*, were downregulated following treatment. Of the 144 previously established AR-associated DNA repair genes (21), 18 were DEGs with 8/18 upregulated (*CHEK1*, *FANCL*, *MAD2L1*, *MBM7*, *PARP1*, *RAD18*, *RAD21*, *RFC3*) [21,22]. *FOLH1* was also upregulated despite its inverse correlation to AR pathway activity, contrasting qPCR findings. Upregulated *Myc* expression in EBRT-treated tumors supports a role for Myc in AR-driven EBRT responses, and pathway analysis showed that the top DEGs converged on cell cycle and regulation of DNA replication, both of which are closely intertwined with AR through cyclins and changes in protein expression during replication [23,24], further supporting a role for AR signaling in prostate cancer response to EBRT.



B Top 10 downregulated genes

Gene ID	Name	log ₂ FC	P	FDR
<i>Ptgr</i>	Prostaglandin F receptor	-7.6236363	4.18E-131	3.08E-127
<i>Pasf1</i>	PAS domain containing repressor 1	-11.193393	1.92E-82	5.36E-79
<i>Dennd2d</i>	DENN domain containing 2D	-7.4705445	2.28E-68	4.46E-65
<i>Slc25a43</i>	Solute carrier family 25 member 43	-10.51026	6.77E-67	1.28E-63
<i>Ncapd3</i>	Non-SMC condensin II complex subunit D3	-3.8351107	3.74E-62	5.24E-59
<i>Fam213a</i>	Peroxisome oxidin like 2A protein coding gene	-4.4899341	1.55E-55	1.78E-52
<i>P2y1</i>	Purinergic receptor P2Y1	-8.0965825	4.02E-51	4.01E-48
<i>Linc01029</i>	Long intergenic non-protein coding RNA 1029	-8.3945845	1.17E-50	1.11E-47
<i>Page1</i>	PAGE family member 1	-5.73256	1.06E-49	9.86E-47
<i>Lin7a</i>	Lin-7 homolog A, crumbs cell polarity complex component	-4.8805976	1.93E-48	1.75E-45

Top 10 upregulated genes

Gene ID	Name	log ₂ FC	P	FDR
<i>Slc22a3</i>	Solute carrier family 22 member 3	8.5526013	2.26E-199	1.33E-194
<i>Etv1</i>	ETS variant transcription factor 1	10.0079367	6.25E-195	1.84E-190
<i>Peg3</i>	Paternally expressed 3	9.1093623	3.70E-182	7.26E-178
<i>Nts</i>	Neurotensin	8.44536161	3.92E-176	5.77E-172
<i>Mmp7</i>	Matrix metalloproteinase 7	8.63440849	6.91E-175	8.13E-171
<i>Camk2n1</i>	Calcium/calmodulin dependent protein kinase II inhibitor 1	7.98820904	1.02E-158	9.97E-155
<i>Pla2g2a</i>	Phospholipase A2 group IIA RHO family interacting cell polarization regulator 2	9.72403886	4.64E-140	3.90E-136
<i>Fam65b</i>	Protein coding gene	7.03750945	1.30E-127	8.50E-124
<i>Pkib</i>	cAMP-dependent protein kinase inhibitor beta	7.05084153	1.85E-123	1.09E-119
<i>Gulp</i>	GULP PTB domain containing engulfment adaptor 1	5.45729705	3.34E-113	1.79E-109

Figure 2. EBRT-induced transcriptomic changes in LNCaP-AR xenografts. (A) Volcano plot showing 4,851 (8.24%) DEGs (FDR=0.01) following EBRT. **(B)** Top 10 up- and downregulated genes (FDR=0.01). Green data points indicate significant genes.

2.4 EBRT increases AR activity in prostate cancer *in vivo*

To confirm EBRT-induced AR signaling *in vivo*, activation of an AR-reporter gene in LNCaP-AR tumors was assessed using bioluminescence imaging. EBRT increased mean AR activity without significant differences between 1 and 4 fractions (Fig. 1D).

2.5 [⁸⁹Zr]11B6 uptake is an indicator of EBRT-induced AR activity

[⁸⁹Zr]11B6 tissue uptake was assessed in 22Rv1 and LNCaP-AR tumors treated with 2, 5, or 10 Gy (1 or 4 fractions) EBRT or left untreated (Fig. 3). A total EBRT dose >10 Gy significantly increased uptake of [⁸⁹Zr]11B6 by LNCaP-AR tumors (38.61%–47.24%IA/g vs. 17.9%–28.3%IA/g in NT) and 22Rv1 xenografts (13.2%–62.6%IA/g, vs. 7.9%–11.2%IA/g NT). Coinjection of cold 11B6 significantly decreased [⁸⁹Zr]11B6 uptake by 22Rv1 tumors after 20 Gy EBRT (13.2%–21.9%IA/g vs. 2.1–13.2%IA/g blocked), confirming hK2 specificity (Fig. 3B).

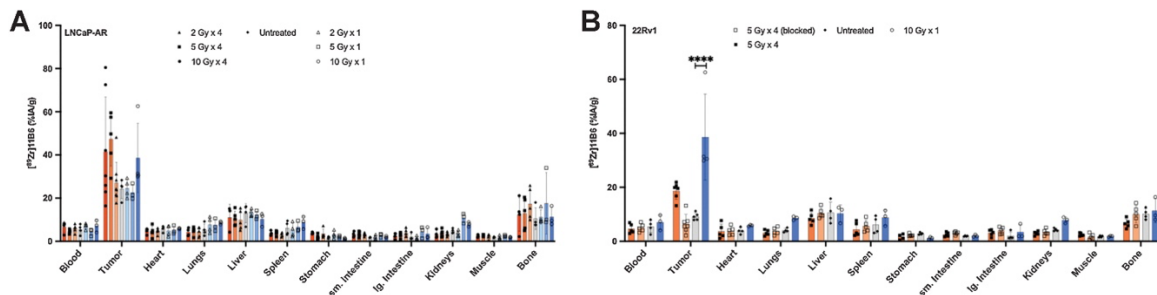


Figure 3. [⁸⁹Zr]11B6 localizes to PCa after irradiation. *Ex vivo* biodistribution of [⁸⁹Zr]11B6 in LNCaP-AR (A) and 22Rv1 (B) at 120h post-EBRT revealed higher uptake in irradiated tumors that received more than 8 Gy total dose of EBRT. Cold, unlabeled 11B6 confirmed specificity in 22Rv1. Mean ± SD and individual values are given; statistical significance was calculated for tumor uptake (NT vs. EBRT) using one-way ANOVA and Dunnett's test for multiple comparisons.

2.6 EBRT-induced AR activity in prostate cancer can be monitored by [⁸⁹Zr]11B6 PET/CT imaging

To confirm [⁸⁹Zr]11B6 uptake as a surrogate marker for EBRT-induced AR activity, [⁸⁹Zr]11B6 uptake was quantified *in vivo* and *ex vivo* in Pb_*KLK2* (nonmalignant) and Hi-*Myc* x Pb_*KLK2* (prostate cancer) mice after treatment with 5 fractions of 10 Gy. No significant volumetric changes were observed by MRI (Fig. 4A, B) after EBRT treatment of prostate cancer tissue. EBRT increased AR expression in prostate cancer (Hi-*Myc* x Pb-*KLK2*; Fig. 4C); this was paralleled by significantly higher [⁸⁹Zr]11B6 uptake after EBRT *in vivo* [before EBRT, 11.04% ± 4.42%; after EBRT (same cohort of mice), 20.23% ± 4.28%].

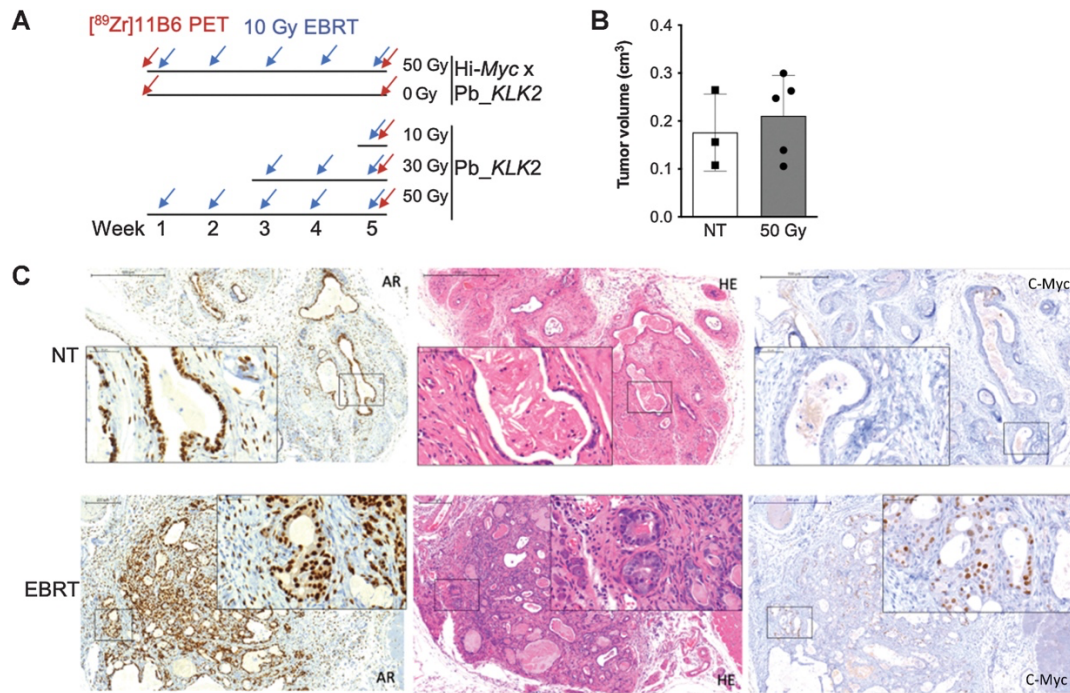


Figure 4. EBRT treatment of Hi-Myc x Pb_KLK2 and Pb_KLK2 mice. (A) EBRT and imaging schedule for PCa (Hi-Myc x Pb_KLK2) and healthy (Pb_KLK2) mice. **(B)** MR imaging revealed comparable PCa volumes \pm 50 Gy treatment. Mean \pm SD and individual values are given; statistical significance was calculated using unpaired two-tailed t-test ($p=0.5872$). **(C)** IHC of Hi-Myc x Pb-KLK2 tumors revealed increased intratumor AR and c-MYC expression after EBRT (magnification: overview 10x, insert 40x).

In contrast, EBRT did not impact uptake in Pb_KLK2 mice (Fig. 5A–C). Correlation of hK2 protein levels in tumors and $[^{89}\text{Zr}]11\text{B6}$ uptake further confirmed AR activity (Fig. 5D). Taken together, these results indicate that hK2-targeted $[^{89}\text{Zr}]11\text{B6}$ can noninvasively monitor increased AR signaling after radiotherapy in a Myc-driven model of prostate cancer.

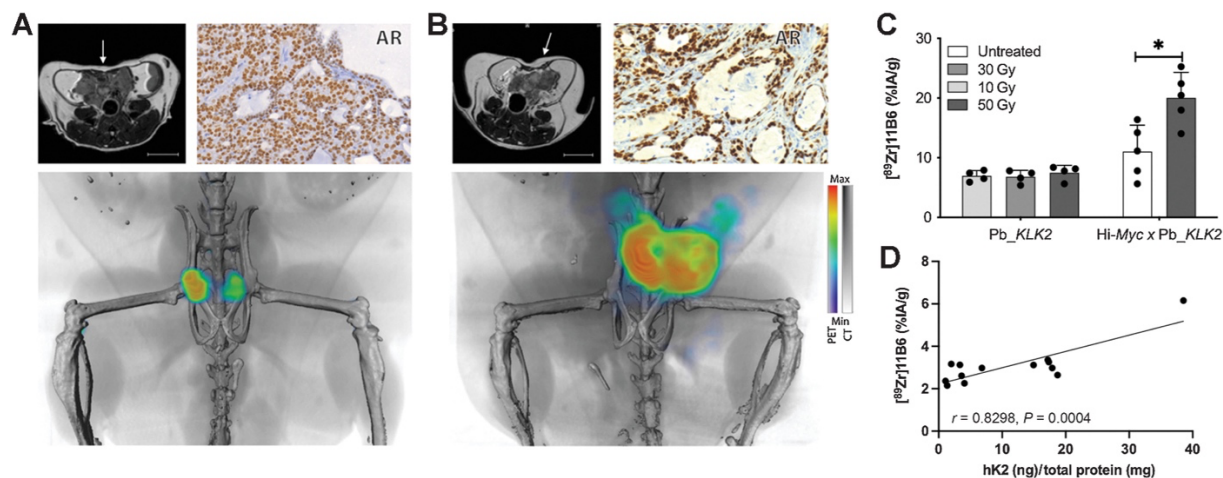


Figure 5. AR activity increase following EBRT visualized by $[^{89}\text{Zr}]11\text{B6}$ -PET/CT. Representative MR, IHC (40x magnification) and volume rendered PET/CT images before treatment (A) and after irradiation with 50 Gy (B) of a Hi-Myc x Pb_KLK2 mouse. White arrow indicates prostate location in MR images (scale: 0.5 cm). (C) Activity concentration of $[^{89}\text{Zr}]11\text{B6}$ increased following irradiation ($p < 0.05$). Mean \pm SD are given; statistical significance was calculated using unpaired two-tailed t-test. (D) PET signal from $[^{89}\text{Zr}]11\text{B6}$ corresponds with *ex vivo* hK2 expression.

2.7 Discussion

The current study demonstrates that EBRT-induced AR activity, which increases in a dose-dependent manner, can be monitored noninvasively using PET. Activation of AR signaling by EBRT may serve as prognostic biomarker and improve development of EBRT combination regimens. In a phase III clinical trial, the combination of EBRT with bicalutamide increased disease-free survival [25], and PSA decay rate during salvage radiotherapy has been identified as a predictor of progression-free survival [26]. EBRT-induced AR activity might thus negatively impact patient outcomes, and vice versa, inhibition of this response may improve

patient care. Attempts to monitor AR noninvasively have been made with [¹⁸F]FDHT, a radio-analog of testosterone [27]; however, [¹⁸F]FDHT reports AR levels rather than its functional signaling activity. To measure AR pathway activity, several AR target genes are utilized as biomarkers and therapeutic targets in prostate cancer, including prostate-specific membrane antigen (PSMA) and PSA. Recently, FDA-approved PSMA-PET has increased the ability to detect metastatic prostate cancer lesions and is considered as a strategy to monitor AR blockade by androgen deprivation therapy (ADT). Unfortunately, preclinical and clinical studies demonstrated that PSMA-PET is not an optimal tool for assessment of ADT efficacy [28-31]. We observed similar findings in our evaluation of PSMA levels after EBRT; *FOLH1* expression increased 2.5-fold in 22Rv1 but not in LNCaP-AR xenografts. Taken together, these results underline the complex links between AR activity, EBRT resistance, and AR pathway biomarkers. It should however be noted that resistance to EBRT may also be caused by non-AR-driven mechanisms.

KLK2 expression and corresponding hK2 protein levels are well established as biomarkers of AR pathway activity [9,10]. In line with a previous study [9], we showed that EBRT increases *KLK2* expression in a dose-dependent manner. To noninvasively target *KLK2*-expressing cells, we developed 11B6, an antibody that specifically internalizes into prostate cancer cells in response to AR activity by binding uncomplexed hK2 [10]. 11B6 can be exploited for PET, single photon emission tomography, intraoperative imaging [10,13], and radioimmunotherapy [18,26]. Studies in multiple rodent models and non-human primates showed that [⁸⁹Zr]11B6 rapidly accumulates in prostate cancer [11], and changes in prostate cancer [⁸⁹Zr]11B6 uptake correspond to both AR activity and hK2 protein levels [10]. We thus hypothesized that [⁸⁹Zr]11B6 could be used to monitor changes in AR activity during and after

EBRT. We confirmed relevance of [⁸⁹Zr]11B6 uptake as biomarker by correlating its tumor uptake with EBRT-induced expression of the canonical AR biomarker *KLK2*. Furthermore, EBRT did not increase [⁸⁹Zr]11B6 prostate uptake in healthy Pb_*KLK2* mice while uptake was significantly elevated in prostate cancer of Hi-*Myc* x Pb_*KLK2* mice; this suggests that EBRT-induced AR activation is a radiobiological response unique to malignant prostate tissues.

EBRT-induced AR activation exclusively in prostate cancer-bearing mice as well as elevated *Myc* levels in xenografts and c-*Myc* expression in the genetic prostate cancer model after EBRT support the known relationship between *Myc* and AR. *Myc* upregulation antagonizes AR signaling and AR target gene expression in patient samples [32] but has been positively correlated to AR variant expression in another study [33]. Upregulation of *Myc* may provide rationale for the use of cotreatment concepts using direct or indirect *Myc* inhibitors to block additional protumorigenic transcription factors that drive prostate cancer [34].

The difference in [⁸⁹Zr]11B6 uptake in the LNCaP-AR xenograft tumor model and the well-documented role of AR as a transcription factor led us to hypothesize that there would be a significant transcriptomic impact in the post-EBRT treatment setting. However, analysis of RNA sequencing of irradiated mice revealed a downregulation of AR, highlighting the variability in tissue response to EBRT. This result exemplifies the need for diagnostic agents that focus on assessing functional AR pathway activity rather than the number of available receptors or AR expression itself. Upregulation of AR pathway target genes *KLK2* and *KLK3* in our data clearly demonstrate that the AR pathway is being differentially activated in tumor-bearing mice after radiotherapy.

The transcriptional EBRT signature observed in the current study is in line with that reported for 11B6 alpha-radioimmunotherapy in Hi-*Myc* x Pb_*KLK2* mice [17]. Comparison of

the top 10 upregulated and downregulated DEGs revealed five common upregulated (*MMP7, ETV1, NTS, PLA2G2A, PEG3*) and downregulated DEGs (*PASDI, DENN2D, PTGFR, SLC25A43, FAM213A*); this similarity underscores the ability of [⁸⁹Zr]11B6-PET to reflect AR-driven therapeutic responses.

Overall, we demonstrated a highly specific and sensitive approach for noninvasive monitoring of functional AR activity under EBRT. We propose that a baseline hK2-PET would be utilized at the time of dose planning, with repeated imaging following treatment start to monitor AR signal. Exclusively in cancerous tissue, [⁸⁹Zr]11B6 tumor uptake correlated with AR pathway activation after irradiation. Changes in [⁸⁹Zr]11B6 prostate cancer uptake paralleled increases in *KLK2* and *AR* expression seen in qPCR analysis, as well as *ex vivo* hK2 protein concentrations and IHC staining. The significantly shorter circulation time of the 11B6 mAb construct in humans (and non-human primates) compared with mice supports feasibility of serial imaging [35] in patients.

Most patients receive cotreatment with pharmacologic compounds inhibiting the AR pathway. However, in some lesions, the AR pathway is still active to some degree due to insufficient dosing, and unknown resistance mechanisms and pathobiology. In this scenario, the molecularly specific and spatially defined signal of 11B6-PET may indicate areas that should receive increased radiation, or conversely, areas without remaining hK2-PET signal could be deescalated to reduce risk of radiation-induced toxicity to surrounding tissues. The notion that rodents have about 50-fold lower testosterone levels than humans, rather on par with castrated patients, underlines the utility of this molecular, lesion-specific, cancer imaging strategy.

There is no doubt that the cost of imaging is a contentious issue in modern patient management. However, the cost of a PET scan, or multiple scans, relative to the treatment planning scans and

daily radiation dosing is incremental—and the ability to capture personalized precision information of patient response (in particular, AR-active lesions that may be outside of the prescribed dose field) is capable of driving significant long-term cost savings. Therefore, hK2-PET/CT would facilitate a deeper understanding of response and resistance patterns of individual tumor lesions and patients and ultimately, of how to adjust treatment.

Thus, although clinical trials are needed, monitoring the AR-target gene hK2 in the treatment setting could allow patient stratification based on AR-pathway response and refinement of treatment and dosing strategies. For example, by selection of AR-targeted treatment combinations and allowing physicians to prescribe the lowest dose needed, monitoring hK2 may provide mechanistic insights into enhancement of EBRT in some patients with concurrent or adjuvant ARSI.

2.8 References

1. Arora, V. K. *et al.* Glucocorticoid receptor confers resistance to antiandrogens by bypassing androgen receptor blockade. *Cell* 155, 1309–1322 (2013).
2. Handle, F. *et al.* Drivers of AR indifferent anti-androgen resistance in prostate cancer cells. *Sci. Rep.* 9, 13786 (2019).
3. Antonarakis, E. S. *et al.* AR-V7 and resistance to enzalutamide and abiraterone in prostate cancer. *N. Engl. J. Med.* 371, 1028–1038 (2014).
4. Zhu, Y. *et al.* Role of androgen receptor splice variant-7 (AR-V7) in prostate cancer resistance to 2nd-generation androgen receptor signaling inhibitors. *Oncogene* 39, 6935–6949 (2020).

5. Bolla, M. *et al.* External irradiation with or without long-term androgen suppression for prostate cancer with high metastatic risk: 10-year results of an EORTC randomised study. *Lancet Oncol.* 11, 1066–1073 (2010).
6. Widmark, A. *et al.* Endocrine treatment, with or without radiotherapy, in locally advanced prostate cancer (SPCG-7/SFUO-3): an open randomised phase III trial. *Lancet* 373, 301–308 (2009).
7. Ulmert, D., O'Brien, M. F., Bjartell, A. S. & Lilja, H. Prostate kallikrein markers in diagnosis, risk stratification and prognosis. *Nat. Rev. Urol.* 6, 384–391 (2009).
8. Sävblom, C. *et al.* Blood levels of free-PSA but not complex-PSA significantly correlates to prostate release of PSA in semen in young men, while blood levels of complex-PSA, but not free-PSA increase with age. *Prostate* 65, 66–72 (2005).
9. Spratt, D. E. *et al.* Androgen Receptor Upregulation Mediates Radioresistance after Ionizing Radiation. *Cancer Res.* 75, 4688–4696 (2015).
10. Thorek, D. L. J. *et al.* Internalization of secreted antigen-targeted antibodies by the neonatal Fc receptor for precision imaging of the androgen receptor axis. *Sci. Transl. Med.* 8, 367ra167 (2016).
11. McDevitt, M. R. *et al.* Feed-forward alpha particle radiotherapy ablates androgen receptor-addicted prostate cancer. *Nat. Commun.* 9, 1629 (2018).
12. Thorek, D. L. J. *et al.* Harnessing Androgen Receptor Pathway Activation for Targeted Alpha Particle Radioimmunotherapy of Breast Cancer. *Clin. Cancer Res.* 25, 881–891 (2019).
13. Timmermand, O. V. *et al.* Preclinical imaging of kallikrein-related peptidase 2 (hK2) in prostate cancer with a (111)In-radiolabelled monoclonal antibody, 11B6. *EJNMMI Res.* 4, 51 (2014).

14. Chen, C. D. *et al.* Molecular determinants of resistance to antiandrogen therapy. *Nat. Med.* 10, 33–39 (2004).
15. Thorek, D. L. J. *et al.* Reverse-Contrast Imaging and Targeted Radiation Therapy of Advanced Pancreatic Cancer Models. *Int. J. Radiat. Oncol. Biol. Phys.* 93, 444–453 (2015).
16. Rosset, A., Spadola, L. & Ratib, O. OsiriX: an open-source software for navigating in multidimensional DICOM images. *J. Digit. Imaging* 17, 205–216 (2004).
17. Bicak, M. *et al.* Genetic signature of prostate cancer mouse models resistant to optimized hK2 targeted α -particle therapy. *Proc. Natl. Acad. Sci. U. S. A.* 117, 15172–15181 (2020).
18. Kuleshov, M. V. *et al.* Enrichr: a comprehensive gene set enrichment analysis web server 2016 update. *Nucleic Acids Res.* 44, W90-7 (2016).
19. Veach, D. R. *et al.* PSA-Targeted Alpha-, Beta-, and Positron-Emitting Immunotheranostics in Murine Prostate Cancer Models and Nonhuman Primates. *Clin. Cancer Res.* (2021).
20. Baena, E. *et al.* ETV1 directs androgen metabolism and confers aggressive prostate cancer in targeted mice and patients. *Genes Dev.* 27, 683–698 (2013).
21. Polkinghorn, W. R. *et al.* Androgen receptor signaling regulates DNA repair in prostate cancers. *Cancer Discov.* 3, 1245–1253 (2013).
22. Sharma, N. L. *et al.* The androgen receptor induces a distinct transcriptional program in castration-resistant prostate cancer in man. *Cancer Cell* 23, 35–47 (2013).
23. Litvinov, I. V. *et al.* Androgen receptor as a licensing factor for DNA replication in androgen-sensitive prostate cancer cells. *Proc. Natl. Acad. Sci. U. S. A.* 103, 15085–15090 (2006).

24. Schiewer, M. J. *et al.* Dual roles of PARP-1 promote cancer growth and progression. *Cancer Discov.* 2, 1134–1149 (2012).
25. Radiation Therapy With or Without Bicalutamide and Goserelin in Treating Patients With Prostate Cancer. *ClinicalTrials.gov identifier: NCT00021450* (2016).
26. Gunnlaugsson, A. *et al.* PSA decay during salvage radiotherapy for prostate cancer as a predictor of disease outcome - 5 year follow-up of a prospective observational study. *Clin Transl Radiat Oncol* 24, 23–28 (2020).
27. Beattie, B. J. *et al.* Pharmacokinetic assessment of the uptake of 16beta-18F-fluoro-5alpha-dihydrotestosterone (FDHT) in prostate tumors as measured by PET. *J. Nucl. Med.* 51, 183–192 (2010).
28. Enzalutamide With Lu PSMA-617 Versus Enzalutamide Alone in Men With Metastatic Castration-resistant Prostate Cancer (ENZA-p). *ClinicalTrials.gov Identifier: NCT04419402* (2022).
29. Lückerrath, K. *et al.* Preclinical evaluation of PSMA expression in response to androgen receptor blockade for theranostics in prostate cancer. *EJNMMI Res.* 8, 96 (2018).
30. Staniszevska, M. *et al.* Enzalutamide Enhances PSMA Expression of PSMA-Low Prostate Cancer. *Int. J. Mol. Sci.* 22, 7431 (2021).
31. Kuten, J., Sarid, D., Yossepowitch, O., Mabjeesh, N. J. & Even-Sapir, E. [68Ga]Ga-PSMA-11 PET/CT for monitoring response to treatment in metastatic prostate cancer: is there any added value over standard follow-up? *EJNMMI Res.* 9, 84 (2019).
32. Barfeld, S. J. *et al.* c-Myc Antagonises the Transcriptional Activity of the Androgen Receptor in Prostate Cancer Affecting Key Gene Networks. *EBioMedicine* 18, 83–93 (2017).

33. Bai, S. *et al.* A positive role of c-Myc in regulating androgen receptor and its splice variants in prostate cancer. *Oncogene* 38, 4977–4989 (2019).
34. Llombart, V. & Mansour, M. R. Therapeutic targeting of “undruggable” MYC. *EBioMedicine* 75, 103756 (2022).
35. Ober, R. J., Radu, C. G., Ghetie, V. & Ward, E. S. Differences in promiscuity for antibody-FcRn interactions across species: implications for therapeutic antibodies. *Int. Immunol.* 13, 1551–1559 (2001).

CHAPTER 3. LRRC15 AS A RADIOIMMUNOTHERAPEUTIC TARGET

Leucine-rich repeat containing 15 (LRRC15) has emerged as an attractive biomarker and target for cancer therapy. We have developed a humanized monoclonal antibody (mAb), DUNP19, that specifically binds to a phylogenetically conserved LRRC15 epitope and is internalized by target-expressing cancer and stromal cells. In xenograft mouse models, Lutetium-177 labeled DUNP19 ($[^{177}\text{Lu}]$ -DUNP19) enables non-invasive imaging and precise radiotherapy to LRRC15-expressing cancer cells and murine cancer-associated fibroblasts (CAFs), halting tumor progression and prolonging survival with minimal toxicity. Transcriptomic analyses of $[^{177}\text{Lu}]$ -DUNP19-treated tumors reveal a loss of pro-tumorigenic mechanisms, including a transforming growth factor beta (TGF β)-driven and LRRC15+ signature associated with immunotherapy resistance. Together, these results demonstrate that radio-theranostic targeting of LRRC15 with DUNP19 is a compelling precision medicine platform for image-guided diagnosis, eradication, and reprogramming of LRRC15+ tumor tissue that drives immunoresistance and aggressive disease.

Adapted from: “Development of a LRRC15-Targeted Radio-Immunotheranostic Approach to Deplete Pro-tumorigenic Mechanisms and Immunotherapy Resistance”

Claire M Storey, Mohamed Altai, Katharina Lückerrath, Wahed Zedan, Henan Zhu, Marija Trajkovic-Arsic, Julie Park, Norbert Peekhaus, Jens Siveke, Diane Abou, Haley Marks, Enna Ulmert, Hans Lilja, Alexander Ridley, Marcella Safi, Constance Yuen, Susanne Geres, Liqun

Mao, Michael Cheng, Johannes Czernin, Ken Herrmann, Laurent Bentolila, Xia Yang, Thomas Graeber, Kjell Sjöström, Robert Damoiseaux, Daniel Thorek, David Ulmert

CMS: writing-original draft, writing-review and editing, data collection, formal analysis

MA: writing-original draft, writing-review and editing, data collection, formal analysis, conceptualization

KL: writing-original draft, writing-review and editing, data collection

WZ, DA, HM, EU, MS, CY, SG, LM: data collection

HZ, MC, TG: formal analysis

MTA, LB: data collection, formal analysis

JP, XY: writing-review and editing, formal analysis

NP, JS, HL, AR, JC, KH, KS, RD: writing-review and editing

DT: investigation, data collection, writing-review and editing

DU: writing-original draft, writing-review and editing, conceptualization

3.1 Introduction

Advancements in the field of immuno-engineering have catalyzed the development of potent antibody-based treatments. However, these therapies are currently applicable towards a narrow subset of malignancies (1). A persistent challenge remains in identifying widely expressed surface antigens for therapy-resistant and metastasized solid tumors (2). The integration of antibodies targeting these biomarkers, alongside advancements in radiochemistry and non-invasive imaging technologies for visualization of radiolabeled antibody distribution, holds substantial promise. This synergy provides a basis for radio-theranostics; selecting patients via imaging that could benefit from treatment and using the same antibody armed with cytotoxic

radionuclides for therapy (3). Such an approach could revolutionize cancer treatment, expanding its reach to address a broader spectrum of therapy-resistant and disseminated cancers.

Leucine-Rich Repeat Containing 15 (LRRC15) is a transmembrane protein expressed in TGF β -driven cancer-associated fibroblasts (CAFs) and cancer cells of mesenchymal stem cell origin, including sarcomas and glioblastomas (4, 5). Although LRRC15 lacks an obvious intracellular signaling domain, recent evidence suggests a role in Wnt/ β -catenin signaling pathway activation to promote invasion and metastasis (6, 7). In tumor tissue, the presence of LRRC15+ cells correlates with resistance to immune checkpoint blockade, increased risk for metastasis, and lower survival rates, underscoring LRRC15's role as an immunomodulator governed by the TGF β pathway (4, 8-9). Notably, LRRC15 has little or no expression in healthy tissue, making the protein a highly promising target for therapeutic intervention.

Here, we describe the development of a highly specific monoclonal antibody (mAb) targeting LRRC15 (designated as DUNP19) that exhibits high specificity for a phylogenetically conserved epitope present on both human and murine LRRC15, and, upon binding to target cells, rapidly internalizes. We exploit DUNP19's rapid internalization profile by labeling the mAb with both diagnostic and cytotoxic radionuclides, transforming it into a dual-purpose agent for use in non-invasive imaging and in therapeutic applications. The potential of this technology extends to personalized treatment strategies and dose planning, maximizing the therapeutic index for individual patients.

For diagnostic and therapeutic purposes, we functionalized DUNP19 with positron emitting Copper-64 (diagnostic [^{64}Cu]-DUNP19) and beta particle emitting Lutetium-177 (therapeutic [^{177}Lu]-DUNP19). As a beta-particle emitter, Lutetium-177 has the potential to cause single-stranded DNA breaks across a span of 10-50 cell diameters. We hypothesized that

the crossfire irradiation by [¹⁷⁷Lu]-DUNP19 could address the challenges presented by the heterogeneous expression of LRRC15 within lesions, especially in larger solid tumors. Our studies, carried out in a range of tumor models with LRRC15+ cancer cells and LRRC15+ CAFs, and in models with LRRC15 expression restricted to CAFs, demonstrate that DUNP19 selectively accumulates in LRRC15+ cells after systemic injection.

Our approach also capitalizes on the deposition of radiation in LRRC15+ cells to eradicate adjacent LRRC15-null tumor tissue and is distinct from classical antibody-drug-conjugates for which target heterogeneity is a limitation. Importantly, systemic treatment with [¹⁷⁷Lu]-DUNP19 resulted in significant therapeutic efficacy and survival in tumor-bearing mice. In addition, transcriptomic profiling of [¹⁷⁷Lu]-DUNP19-treated tissues revealed progressive loss of TGFβ-driven genomic signatures associated with malignant disease aggressiveness and immunotherapy resistance. Taken together, these findings highlight the potential of DUNP19 as a radio-theranostic modality for non-invasive detection, targeting, and reprogramming of immuno-suppressive gene signatures within cancer cells and the tumor microenvironment.

3.2 Materials and Methods

3.2.1 Production and labeling of DUNP19

For DUNP19 production, HEK293 cells were cultured in a 2L suspension using FreeStyle 293 Expression Medium (Life Technologies, Carlsbad, CA, USA) with a cell density maintained at 1×10^6 cells/mL on the day of transfection. Expression plasmids harboring genes for DUNP19 heavy chain and light chain in human IgG1/kappa format were combined with the transfection agent and incubated for 10 min at room temperature. The transfected cell culture was then incubated at 37 °C, 8% CO₂ on an orbital shaker rotating at approximately 110 rpm

for seven days. Culture medium was collected, subjected to centrifugation, and filtered through 0.22 μm filter systems. Antibodies were isolated through Protein A chromatography, followed by buffer exchange to PBS (pH 7.4) via gel filtration. The concentration was calculated from absorbance measurement at 280 nm.

For labeling with Lutetium-177 and Copper-64, respectively, DUNP19 was functionalized with benzylisothiocyanate derivatives of the acyclic chelating agent CHX-A''-DTPA (p-SCN-CHX-A''-DTPA) or cyclic NOTA (p-SCN-NOTA), respectively, using amine-reactive chemistry. Radiolabeling was performed as previously described (see Supplementary Materials and Methods) (31). The average radiochemical yield was $95\pm 5\%$ with a radiochemical purity $>99\%$ and an average specific activity of 4 MBq/mg. Injection solutions of [^{177}Lu]-DUNP19 were formulated in 2% BSA/PBS containing 0.14 mM EDTA (100-fold molar excess). Binding affinity of the radio-conjugate to life cells was determined using Ligandtracer technology (32).

An amine-based protein labeling kit (Invitrogen, #A20173) was used for labeling DUNP19 with AlexaFluor-647 or AlexaFluor-594. Labeling was performed as described by the kit's recommended protocol. All buffers were treated with Chelex 100 resin (sodium form, Merck KGaA, Darmstadt, Germany) to remove any metal ions and filtered through a 0.22 μm filter before use. Prior to conjugation, DUNP19 was buffer exchanged using an AMICON Ultra-0.5-centrifugal filter device with a MWCO 30 kDa (Millipore, Burlington, MA, USA). DUNP19 (500 μg in 500 μl 0.07 M sodium borate, pH 9.3) was mixed with the bifunctional chelator p-SCN-CHX-A''-DTPA (Macrocyclics, Texas, USA) in a 6:1 molar ratio. The mixture was extensively vortexed and incubated overnight at 38°C. The reaction mixture was then

centrifuged for 10 minutes at 14000 x g using a 30 kDa filter to remove the excess non-bound chelator. The concentrate containing the CHX-A''-DTPA-DUNP19 conjugate was recovered, and the buffer was adjusted to 0.2 M ammonium acetate (pH 5.5). The conjugate was aliquoted and kept at -20 °C until labeling. For labeling with ¹⁷⁷Lu, 30-50 µg of the conjugate was mixed with 15-20 MBq ¹⁷⁷LuCl₃ (Curium, Sweden) and incubated at 38°C with continuous vortexing for 30 min. Thereafter the radiolabeled conjugate was purified, and buffer exchanged using AMICON 30 kDa filter. Radiochemical yield and purity of the radioconjugate were determined using silica-impregnated ITLC strips (150–771 DARK GREEN Tec-Control Chromatography strips, Biodex Medical Systems) eluted with 0.2 M citric acid and measured using the Cyclone Storage Phosphor System (PerkinElmer, Waltham, MA, USA). To reduce radiolysis, the final product was diluted with 2% BSA/PBS buffer (pH 7.4) and 100X molar excess of EDTA was added to scavenge any free metal ions.

To determine the maximal attainable specific activity for labeling DUNP19 with ¹⁷⁷Lu, decreasing amounts of CHX-A''-DTPA-DUNP19 (10, 5, and 2.5 g) were incubated at 38°C for 30 minutes with a fixed quantity of ¹⁷⁷LuCl₃ (10 MBq). The radiochemical yield was determined using SG-ITLC, as previously described. Conjugation of p-SCN-Bn-NOTA chelator to DUNP19 was performed in a manner similar to that used in the CHX-A''-DTPA conjugation described above. Copper-64 was produced at the Washington University in St. Louis School of Medicine Cyclotron facility. ⁶⁴CuCl₂ (20 mCi; 25 µL) was diluted with a 10-fold excess 0.1 M ammonium acetate (NH₄OAc), pH 5.5 and then added to NOTA-conjugated anti-LRRC15 antibody. After mixing for 30 min at room temperature, the antibody conjugate was purified by gel chromatography (PD10) into 0.1 M HEPES buffer in saline. Purity was assessed by radioITLC (Bioscan AR2000 using samples spotted on Whatman paper in a running buffer of

50 mM DTPA (pH 5.5). Quantitative labeling with >99% radiochemical purity was observed.

3.2.2 Cell Culture

U118MG (glioblastoma), U87MG (glioblastoma), RPMI7951 (melanoma), NCI-H196 (small cell lung cancer), HCC1954 (breast cancer), SAOS2 (osteosarcoma), U2OS (OS), Kasumi-2 (leukemia), Calu-1 (non-small-cell lung cancer), RCH-ACV (leukemia), MHH-Call-3 (leukemia), Hs737.T (giant cell sarcoma), HEK293T, LNCaP (prostate cancer), and K7M2 (murine osteosarcoma) were purchased from ATCC. HuO9 (osteosarcoma) was purchased from the Japanese Cancer Research Resources Bank (Tokyo, Japan). All cell lines were cultured according to the manufacturer's instructions and frequently tested for Mycoplasma.

To overexpress LRRC15, HEK293T and K7M2 cells were transduced with a pLenti-LRRC15-GFP-Puro vector (Origene, NM_130830) with a multiplicity of infection of 5. Optimal puromycin concentrations for stable selection of pLenti-LRRC15-GFP-Puro were determined by kill curves. Following selection with puromycin for 14 days, single cell clones were plated by serial dilution, expanded, and sorted for the top 1% of GFP+ cells.

3.2.3 *In Vitro* Studies

3.2.3.1 Pulldown Assay (Immunoprecipitation - Mass Spectrometry)

Pierce Protein G Magnetic Beads (ThermoFisher, #88847) were pre-incubated with 70 ug DUNP19 antibody or hIgG1 mAb in PBS at room temperature (RT) for 1 h. Bead-antibody conjugate was recovered using magnetic separation before adding 300 ug protein lysates

(isolated from U118MG cells) for 2 h on ice. Beads were washed with PBS and an on-bead digestion was performed with 0.25 % Trypsin for 16 h. MS-MS was run using the Agilent 6530 LC/MS in collaboration with the UCLA Molecular Instrumentation Center according to previously described protocols (33, 34).

3.2.3.2 Flow Cytometry

To assess the binding affinity of DUNP19, cells were blocked (10% normal goat serum in PBS, 15 minutes at RT) and incubated with serial dilutions of fluorophore-conjugated DUNP19 or hIgG1 mAb (0.051 – 1000 ng/mL) in triplicate for 1 h at RT. Cells were washed with 1% BSA in PBS (180 x g, 3 minutes) before adding viability dye per manufacturer's instructions (Invitrogen, #L34989). Antibody binding capacity of cells was assessed using 1 µg/mL DUNP19 and anti-human IgG Simply Cellular bead standards (Bangs Laboratories, #816). Quantity of LRRC15 surface antigens available for DUNP19 binding was normalized to cell surface area (determined experimentally by confocal microscopy). All flow cytometry experiments were run in collaboration with UCLA's Jonsson Comprehensive Cancer Center Flow Cytometry Shared Resource using an Attune NxT Flow Cytometer (Invitrogen). Flow cytometry data were analyzed using FlowJo (Version 10, BD Biosciences).

3.2.3.3 Reverse Transcriptase Polymerase Chain Reaction (RT-PCR)

Expression of *LRRC15* in cells was determined by Taqman qRT-PCR. Cells were lysed and one-step reverse transcription/quantitative PCR performed with Cells-to-CT Taqman kit

(A25603). *LRRC15* was probed with Applied Biosystems Taqman Assay probes (Assay ID Hs00370056_s1) and normalized using *GAPDH* housekeeping gene (Assay ID Hs02786624_g1). All qPCR assays were run using the ViiA 7 Real-Time PCR system (Applied Biosystems).

3.2.3.4 Confocal Microscopy of Cells

For immunocytochemistry, cells were blocked with 10% normal goat serum in PBS for 1 h at room temperature. Cells were stained with DUNP19 (20 ug/mL) and anti-PMCA1 antibody (Abcam, ab3528, 1:100). Primary antibodies were incubated overnight at 4 °C before washing and staining with goat anti-rabbit AlexaFluor647 (1:500, Invitrogen A21235) and goat anti-human AlexaFluor488 (1:500, Invitrogen A11013) secondary antibodies. Cells were fixed with 3.7% paraformaldehyde for 15 minutes at RT before washing and mounting cells with Vectashield mounting media with DAPI (H1200-10) onto slides for imaging with a Leica TCS SP8 Digital Microscope.

To confirm internalization, cells (0.0015×10^6 cells/well) were seeded in phenol red-free complete media in 384-well u-clear flat bottom black plates (Greiner, #781092) and stained with 1 ug/mL DUNP19-AF647, anti-huLAMP1-A488 antibody (1:250, Invitrogen, 53-1079-42) and Hoechst 33342 (1:2000 dilution, Invitrogen) at 4°C for 1 h to prevent antibody internalization while promoting surface binding. Unbound antibody was aspirated and replaced with phenol red-free complete media. Time-lapse confocal imaging was performed using a temperature controlled ImageXpress MicroXL High Content Imaging microscope (Molecular Devices). The microscope temperature was set to mimic cell culture conditions (37°C, 5% CO₂) and images

were taken at 10x magnification (4 sites per well) every 20 minutes for 6-12 h. The plasma membrane signal of DUNP19-AF647 relative to the cytosolic signal (LAMP1) at time 0 (directly after incubation at 4°C) was quantified to calculate the fraction of internalized antibodies over time.

3.2.4 *In Vivo* Studies

3.2.4.1 Animal Studies

All animal experiments were conducted in compliance with national legislation on laboratory animal protection and permitted by the local ethics committees for animal research at Washington University, Lund University, University of California, Los Angeles and University of Duisburg-Essen.

3.2.4.2 Subcutaneous Tumor Models

Athymic nude mice (BALB/cAnNRj-Foxn1 nu/nu; 6–8 weeks old, 20–25 g; Janvier) were inoculated with U118MG (5.8×10^6 cells), SAOS2 (6×10^6 cells), HuO9 (6×10^6 cells), HCC1954 (4.9×10^6 cells) or LNCaP (5×10^6 cells) cells in a 200 μ L (1:1 v/v) mixture of media with Matrigel via subcutaneous injection in the right flank. Tumors developed after 3 to 6 weeks. Tumor volume was estimated with caliper measurements twice weekly ($V \text{ (mm}^3\text{)} = 0.5 \times \text{length} \times \text{width}^2$).

3.2.4.3 Orthotopic Osteosarcoma Model

Nineteen athymic nude mice (BALB/cAnNRj-Foxn1 nu/nu; males, 6-8 weeks old, 24.2±1 g; Janvier) were anesthetized, and the tibia of the right hind limb was punctured. HuO9 cells (1.5×10^6 cells in 10 μ L media) were injected into the cavity using a microvolume syringe with a 27-gauge needle. Bone wax (Surgical Specialties Corporation, #903) was applied to seal the punctured area and prevent exodus of implanted cells before the area was washed with saline. Tumor development was confirmed using ultra-high-resolution CT and [^{177}Lu]-DUNP19 SPECT/CT imaging (nanoScan; Mediso, Budapest, Hungary).

3.2.4.4 Small-Animal Imaging

PET: Male mice (B6;129-Rag2tm1FwaII2rgtm1Rsky/DwIHsd) (n = 5) bearing s.c. SAOS2 xenografts were intravenously (i.v.) injected with [^{64}Cu]-DUNP19 (8.75 MBq, 100 μ g DUNP19 in 100 μ L 10 mM ammonium acetate). Dynamic PET images were acquired during the first hour post-injection (p.i.), followed by static scans (20 minutes each) at 12 h, 24 h, and 36 h using a microPET R4 rodent scanner (Siemens). To confirm specificity of the DUNP19 PET-signal, imaging with the bone-seeking PET-probe Fluorine 18-sodium fluoride ([^{18}F]-NaF; 10 MBq i.v.) was performed in mice bearing SAOS2 tumors. SPECT: Mice with intratibial HuO9 xenografts were i.v. injected with [^{177}Lu]-DUNP19 (20 MBq, 30 μ g). Mice were scanned for 50-60 minutes under anesthesia (2-3% isoflurane) using a SPECT/CT device (nanoScan Mediso, Budapest, Hungary). Details on PET, SPECT and CT acquisition are provided in the Supplementary Materials and Methods.

3.2.4.5 [¹⁷⁷Lu]-DUNP19 Biodistribution and Kinetics

To investigate the biodistribution of [¹⁷⁷Lu]-DUNP19, mice with s.c. SAOS2, HuO9, U118MG, HCC1954, or K7M2 tumors, respectively, received 0.5 MBq [¹⁷⁷Lu]-DUNP19 (SAOS2, U118MG, K7M2: 16 µg; HuO9, HCC1954: 30 µg) by i.v. injection and were sacrificed at predetermined time points (SAOS2: 6, 24, 48, 72, 168 and 336 hours p.i.; HuO9: 6, 24, 48, 72, 168 and 336 h p.i.; U118MG: 24, 48 and 72 hours p.i.; n=4 mice/time point, HCC1954 and K7M2: 72 h p.i.). To confirm targeting specificity, mice bearing both LRRC15+ U118MG (left flank) and LRRC15- LNCaP (right flank) xenografts were i.v. injected with either 0.5 MBq [¹⁷⁷Lu]-hIgG1 mAb or [¹⁷⁷Lu]-DUNP19 (n=4 mice) and sacrificed 48 hours later. To study the effect of the antibody mass amount on the biodistribution and tumor uptake, mice bearing HuO9 tumors (n=5 mice/group) were administered escalating DUNP19 doses (1, 10, 30, 100 and 300 µg/mouse at 0.5 MBq ¹⁷⁷Lu; i.v.) and euthanized 72 h p.i.. In all studies, blood, tumors, and several normal tissues were collected, dried and weighed. The radioactivity contained in the respective tissue and reference standards (0.5 MBq [¹⁷⁷Lu]-DUNP19) was quantified in a NaI(Tl) automated well counter (1480 WIZARD; Perkin Elmer). Decay-corrected data were expressed as percent injected activity per gram tissue (% IA/g).

3.2.4.6 Radiological Analysis of Tumor Calcification

Quantification of radiopacity was analyzed using ImageJ software (version 1.53). A brightness threshold of 41 was used to define the area of each tumor sample. The total area of

the tumor was then quantified using ImageJ's built-in area analysis program. Areas of calcification were defined by a brightness threshold of 81 and quantified in the same manner. Percent calcification was calculated by dividing the area of calcification over the area of the entire tumor.

3.2.4.7 Confocal Microscopy of Xenografts

Mice with HuO9, SAOS2 and HCC1954 tumors, respectively, were injected with 30 ug DUNP19-AF594 when tumor volume reached between 200-300 mm³. Sections were washed two times with PBS before permeabilization with 0.1 % Triton-X/ PBS and blocking for 1 h at RT with 10 % goat serum/ PBS. Sections were stained with an anti-LAMP1-A488 antibody (HuO9, SAOS2: anti-hLAMP1, 1:250, Invitrogen, #53-1079-42; HC1954: anti-mLAMP1, 1:250, Invitrogen, #53-1071-82, to detect the murine stroma) overnight at 4°C. The next day, slides were stained with Phalloidin-AF647 for 1 h at RT (1:2000, Invitrogen, #A22283) and mounted with Vectashield Antifade mounting media with DAPI (Vector Laboratories, H-2000-2). Confocal microscopy was done by the UCLA Advanced Light Microscopy and Spectroscopy Laboratory (ALMS) with a Leica TCS-SP8 microscope at 63x magnification and sequential imaging for far-red, orange, green and blue emitting dyes. Z-stack images were taken and Lightning deconvolution and 3D reconstruction (Leica Microsystems) were performed during post-processing.

3.2.4.8 Therapy Studies

Average tumor volume at the start of treatment was $181 \pm 20 \text{ mm}^3$ and the average animal weight was $25.2 \pm 0.7 \text{ g}$. Mice bearing s.c. HuO9 or U118MG xenografts with LRRC15 expression in both tumor cells as well as tumor stroma, and HCC1954 xenografts with LRRC15 expression only in the tumor stroma, were randomized into groups of 10-12 animals receiving either [^{177}Lu]-DUNP19 (16-30 μg , i.v.) or no treatment. HCC1954 model: Mice were treated with a single injection of either 10 MBq or 20 MBq [^{177}Lu]-DUNP19. HuO9 model: Animals received three fractionations [^{177}Lu]-DUNP19 at days 0, 32 and 75 resulting in a cumulative administered activity of 50 MBq (group 1: 10+20+10 MBq; group 2: 20+10+20 MBq). To investigate the impact of pre-therapeutic tumor volume on the efficacy of [^{177}Lu]-DUNP19 in the HuO9 model, mice (n=6-10 mice/group) were administered 30 MBq [^{177}Lu]-DUNP19 (30 μg , i.v.) when tumors reached a volume of $203 \pm 64 \text{ mm}^3$ (group 1) or $504 \pm 152 \text{ mm}^3$ (group 2). U118MG model: Mice were treated with two fractions [^{177}Lu]-DUNP19 at days 0 and 34 and a cumulative activity of 20 MBq (10+10 MBq) or 30 MBq (20+10 MBq). Treatment efficacy was assessed by measuring tumor growth and time to a humane endpoint. Mice survival was analyzed by using a log rank test in GraphPad Prism. P values <0.05 were considered significant statistically. Tumors from a subset of mice were harvested 90-120 days p.i. (except U118MG: day 155 p.i.) and processed for RNA-sequencing (see below).

To evaluate the efficacy of [^{177}Lu]-DUNP19 in a clinically relevant orthotopic osteosarcoma model, mice with intratibial HuO9 tumors were randomized (23 days post-tumor engraftment) to receive 20 MBq [^{177}Lu]-DUNP19 (30 μg , i.v.; n=12) or PBS (n=7). Four days after treatment, [^{177}Lu]-DUNP19 tumor uptake and presence of viable HuO9 tumor was assessed by SPECT/CT imaging. At day 163 post-first injection, mice received an additional 20 MBq

[¹⁷⁷Lu]-DUNP19 and were re-scanned to detect residual viable HuO9 tumor tissue. Mice were followed up for 190 days after the first [¹⁷⁷Lu]-DUNP19 injection.

3.2.4.9 Toxicity of [¹⁷⁷Lu]-DUNP19

Body weights and hematological toxicity and recovery were monitored in mice treated with [¹⁷⁷Lu]-DUNP19. Blood samples were taken before and weekly after injection of [¹⁷⁷Lu]-DUNP19 for 4 weeks p.i.. Samples (20 µL) were collected from the tail vein of awake, immobilized mice by piercing the vein with a needle (27G) and collecting blood in a K2EDTA-coated plastic micropipette. Blood cell counts were obtained using an Exigo Veterinary Hematology Analyzer (Boule Medical, Stockholm, Sweden).

3.2.4.10 Immunohistochemistry

LRRC15 expression was analyzed on formalin-fixed, paraffin embedded sections using the Dako REAL Peroxidase Detection System (Dako) according to the manufacturer's instructions. Antigen retrieval was performed by heat-induced epitope retrieval using Tris/EDTA (pH 8.1). Sections were incubated with anti-hLRRC15 antibody [EPR8188(2)] (1:100; #ab150376, Abcam) for 1 h at room temperature.

3.2.5 Gene Expression Analysis

For RNA-sequencing, tumor tissues were harvested at 90-120 days (HuO9, HCC1954) or 155 days (U118MG) post-treatment, apart from untreated mice (harvested when tumor

volume measured greater than 1000 mm³, in accordance with established endpoint protocols). Tumor tissue was preserved in *RNAlater* stabilization solution (Invitrogen, AM7020) before RNA isolation with the Qiagen RNeasy kit (#74004). RNA quality control was assayed via TapeStation (Agilent) and stranded mRNA library preparation performed in accordance with Illumina protocols. Samples were sequenced on Illumina's Novaseq platform to generate 50bp paired-end reads. Library preparation and sequencing was done with the help of UCLA's Technology Center for Genomics and Bioinformatics (TCGB).

Raw read count RNA-sequencing data were generated from untreated and [¹⁷⁷Lu]-DUNP19 treated HuO9 (untreated n=6, treated n=16), U118MG (untreated n=8, treated n=16) and HCC1954 (untreated n=8, treated n=10) tumors. Paired-end reads were aligned to either human (Hg38) or murine (Mm19) genome using the STAR method, as previously described (35). Ambiguous reads were discarded and FastQC analysis was utilized to confirm sequence quality. Low read count filtering was used to remove transcriptomic features for which fewer than 4 samples had at least 5 read counts of a gene, as described by the EdgeR differential analysis user guide (36). For each tumor model, principal component analysis based on log₂ counts in RStudio Version 2023.06.1 was plotted. K-Clustering and heat maps were generated on log₂-transformed read counts to visualize gene signatures in treated versus untreated samples. Differential expression analysis to identify differentially expressed genes was performed using EdgeR (Bioconductor, Version 3.40.2) using quasi-likelihood F-tests within the EdgeR program. A false discovery rate of 0.05 (adjusted using Benjamini-Hochburg methodology) and absolute log₂-fold change >1 were selected as the cutoff for DEGs within this analysis. A positive fold-change represented upregulation and a negative fold change represented downregulation of gene expression in treated tumors. For comparison and visualization of gene expression between

clustered samples, z-scores were calculated per gene. Pathway analysis was performed using gene set enrichment analysis and molecular signatures defined using the human and murine Molecular Signature Database Hallmark pathways (37). Additional analysis was performed using Gene Ontology (GO) Biological Pathways. For cell classification and identification, Syllolist (22) was used to identify signatures present from 43 cell types within normalized gene expression matrices. For murine cell classification, murine orthologs were matched to Syllolist cell signatures using g:Profiler.

3.2.6 Statistical Analysis

Statistical analyses were conducted using Graphpad Prism software (Version 9.5.1). Data are expressed as mean and standard deviation. Statistical comparisons were performed using one-way ANOVA with Tukey multi-comparison tests and unpaired Student's t-tests. A P-value of less than 0.05 was considered statistically significant. RNA-sequencing data are available from the Gene Expression Omnibus NCBI database upon publication (cite).

3.3 LRRC15 can be Targeted Utilizing the mAb DUNP19

Our initial investigations tested the specificity of DUNP19 and demonstrated binding to both human and murine recombinant LRRC15 with high affinity (Supp. Fig. 1A). Specific interaction of DUNP19 with LRRC15 was further substantiated by immunoprecipitation of the LRRC15 protein from glioblastoma (U118MG) cell lysates with DUNP19-coated magnetic beads (Supp. Fig. 1B). We next characterized the binding of DUNP19 to LRRC15 across a wide range of

cancer cell lines from a range of lineages including melanoma (RPMI7951), glioblastoma (U118MG) and osteosarcoma (HuO9, SAOS2), selecting cell lines based on *LRRC15* gene expression data in publicly available databases: the EMBL-EBI expression atlas, Harmonizome 3.0, COSMIC, and the Cancer Cell Line Encyclopedia (CCLE) database (10). Despite selecting cell lines that exhibited high *LRRC15* expression at the RNA level, not all were found to have detectable protein on the cell surface. Among those that did, DUNP19 retained picomolar affinity for cell-surface target antigen ($EC_{50} = 0.83 - 222.22$ pM) (Fig. 1A). In addition, a positive correlation was noted between the number of *LRRC15* molecules on the cell surface and *LRRC15* mRNA levels ($R^2 = 0.567$) (Fig. 1B). Specific binding to *LRRC15* on the cell surface was further confirmed by confocal microscopy of AF647-labeled DUNP19 (Fig. 1C). Next, we studied cellular internalization of DUNP19. Antibody internalization enhances the retention time of the delivered radionuclide, thereby increasing both image contrast and absorbed doses of therapeutic radiation (11). Confocal microscopy studies illustrated that DUNP19 is rapidly internalized by *LRRC15* expressing cells (Fig. 1D,E). Interestingly, internalization rates for DUNP19 were contingent on the quantity of available molecules; faster kinetics were observed in cells with a higher abundance of *LRRC15* molecules (HuO9: 1284.74 ± 63.17 molecules per μm^2 , 132.06 \pm 10.14 minutes; SAOS2: 684.89 ± 100.67 molecules per μm^2 , 145.62 \pm 15.18 minutes; Fig. 1D). Conjugation chemistry did not impact DUNP19; the internalization rate of the chelate-conjugated antibody (CHX-A''-DTPA-DUNP19) was analogous to that of the unconjugated antibody (Supp. Fig. 2A). Furthermore, time-resolved cellular assays indicated that ^{177}Lu -radiolabeling did not affect affinity (U118MG: $K_d = 301 \pm 39$ pM; HuO9: 117 ± 46 pM; SAOS2: 56 ± 27 pM; RPMI-7951: 25 ± 0.1 pM; Fig. 1F).

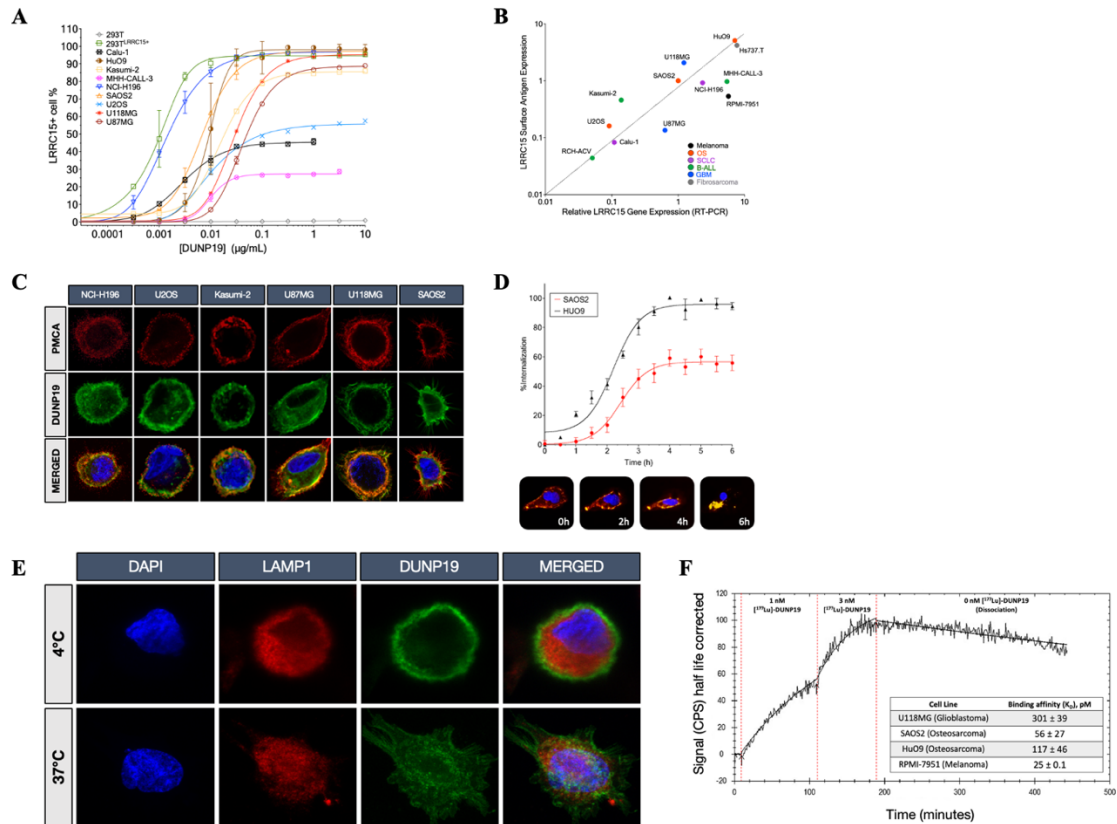


Figure 1. *In vitro* evaluation of DUNP19's binding profile to LRRRC15. **A.** Flow cytometry demonstrates that DUNP19 binds with picomolar affinity to LRRRC15 molecules on various cell lines, exhibiting distinct expression levels and tissue origins. Detection of LRRRC15 was based on the assessment of antigen-antibody equilibrium. **B.** Analysis across a diverse range of cell lines unveils correlations between *LRRRC15* mRNA expression and the abundance of LRRRC15 molecules bound by DUNP19. **C.** Confocal microscopy of various cell lines incubated with AlexaFluor647-labeled DUNP19 at room temperature, followed by staining for plasma membrane-associated calcium ATPase (PCMA) and DNA (DAPI). Images reveal that DUNP19 binding corresponds with LRRRC15 expression levels and co-localizes with LRRRC15. **D.** Internalization rates of AlexaFluor647-labeled DUNP19 at 37°C were examined in LRRRC15-

expressing HuO9 and SAOS2 cells using live confocal microscopy. The endocytic process of DUNP19 is accelerated in cells with higher LRRC15 abundance. **E.** Confocal microscopy of SAOS2 cells incubated with AlexaFluor647-labeled DUNP19 at 4°C or 37°C, co-stained for lysosomes (LAMP1) and DNA (DAPI). DUNP19 is exclusively found in the plasma membrane at the lower temperature demonstrating that the rapid endocytosis after binding to LRRC15 is an active, energy-requiring process. **F.** LigandTracer sensorgram of [¹⁷⁷Lu]-DUNP19 binding to LRRC15-expressing HuO9 cells, measured at 1 nM and 3 nM concentrations. Cell-bound activity, presented as CPS, was used to determine association, dissociation rates, and equilibrium dissociation constants (K_D). The table shows K_D values for various LRRC15-expressing cell lines.

3.4 DUNP19 *In Vivo* PET Can Monitor Tumor-Associated LRRC15 Expression

To evaluate *in vivo* kinetics of DUNP19 in healthy organs and LRRC15-expressing tumors, sequential PET images were acquired of subcutaneous (s.c.) osteosarcoma (SAOS2) bearing mice after intravenous (i.v.) administration of a ⁶⁴Cu-labeled version of the mAb ([⁶⁴Cu]-DUNP19). Tumor accumulation was compared to the clinical bone scanning agent [¹⁸F]-NaF. Rapid [⁶⁴Cu]-DUNP19 uptake *in vivo* recapitulated *in vitro* internalization, selectivity, and retention in malignant tissue. In contrast, [¹⁸F]-NaF exhibited limited accumulation in osteogenic tumors, with the bladder showing the highest activity due to urinary excretion (Fig. 2A). These findings suggest that DUNP19-PET can be utilized to noninvasively determine LRRC15 expression and select patients for treatment, improving upon existing FDA-approved PET tracers for bone cancer lesions.

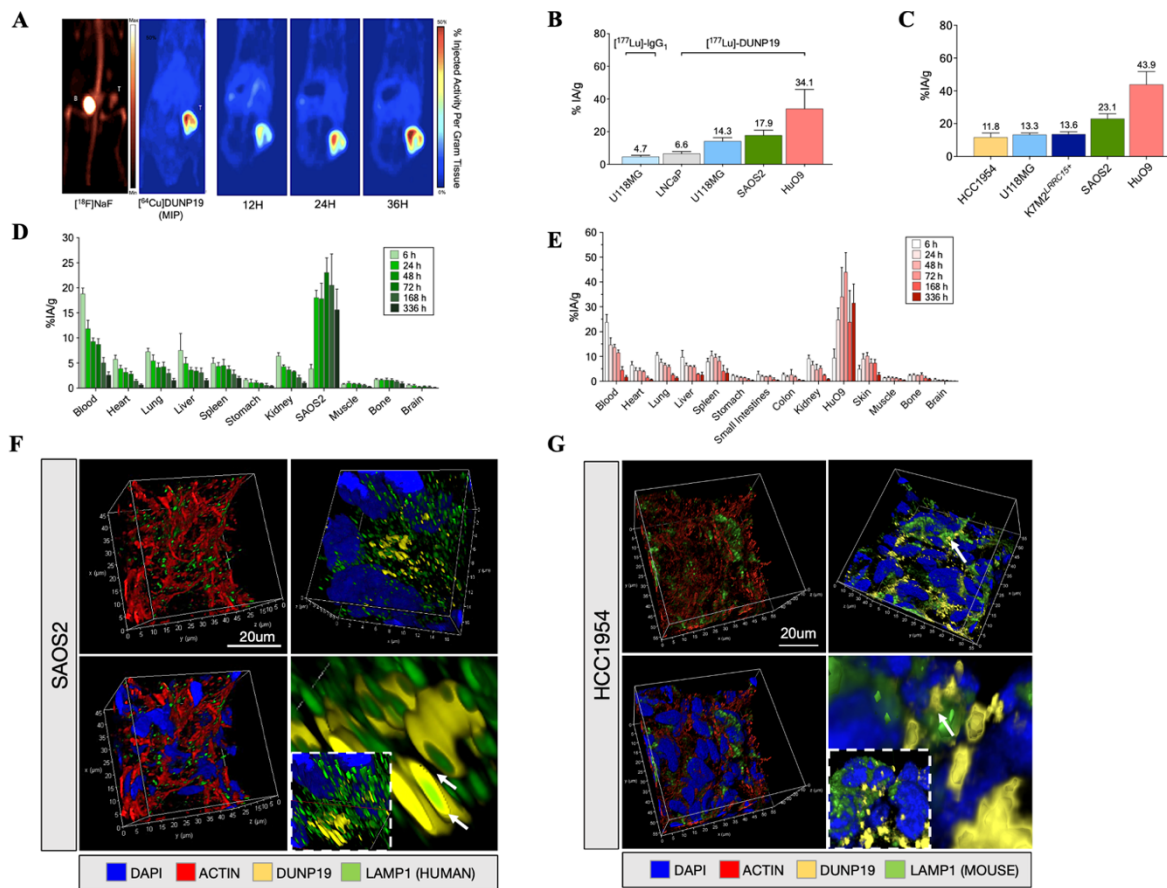


Figure 2. Specificity and biodistribution of DUNP19 in multiple mouse models with LRRC15 expressing tumors. **A.** Representative PET images of s.c. SAOS2 osteosarcoma xenografts obtained at different time points post i.v. administration of $[^{64}\text{Cu}]\text{-DUNP19}$, highlighting significant tumor-specific uptake with minimal accumulation in normal tissues. In contrast, PET with the clinical bone scanning agent $[^{18}\text{F}]\text{-NaF}$ showed low activity in tumor tissue, with the majority of the tracer dose observed in bone (Bn) and bladder (Bl). **B.** *In vivo* assessment of LRRC15 targeting specificity by $[^{177}\text{Lu}]\text{-DUNP19}$. At 48 h post i.v. injection, $[^{177}\text{Lu}]\text{-DUNP19}$ displayed significantly higher uptake ($p < 0.001$) in LRRC15+ U118MG (blue bar) and HuO9 (red bar) tumors compared to LRRC15- LNCaP tumors (light gray bar). The accumulation of non-specific $[^{177}\text{Lu}]\text{-IgG1}$ in LRRC15+ U118MG tumors (dark gray bar) was

significantly lower than that of [^{177}Lu]-DUNP19. **C.** [^{177}Lu]-DUNP19 tumor uptake in multiple s.c. tumor models at 72 h p.i., correlating with the LRRC15 expression level in the respective model. **D. + E.** Kinetics of [^{177}Lu]-DUNP19 in healthy organs and LRRC15+ SAOS2 and HuO9 osteosarcoma lesions. *Ex vivo* tissue biodistributions of [^{177}Lu]-DUNP19 obtained at multiple time points after i.v. injection showed a continuous decline in activity levels in healthy organs, but sustained uptake by malignant lesions. **F. + G.** Microanatomy of tumor tissues obtained from animals treated with fluorescently labeled DUNP19. Confocal images of s.c. SAOS2 (LRRC15+ cancer cells / LRRC15+ CAF) and HCC1954 (LRRC15- cancer cells / LRRC15+ CAF) tumors harvested at 72 h post- i.v. injection of AF594-DUNP19 (yellow). Tumor sections were co-stained for Actin (red), DNA (DAPI, blue) and LAMP1 (lysosomal marker, green). Images show that DUNP19 accumulates in the cellular cytoplasm and co-localized with LAMP1 indicating intracellular trafficking of the mAb to the lysosomal compartments (arrow) after binding membranous LRRC15.

3.5 [^{177}Lu]-DUNP19 Exhibits a Favorable Biodistribution

^{177}Lu is a clinically relevant beta particle emitter with a half-life of 6.7 days and maximum tissue penetration range of 1.5 mm. Because of the radionuclide's long path length, ^{177}Lu can be used to deliver ionizing radiation to target cells and to target-null cells in close proximity via a crossfire effect (12). Given these characteristics, we hypothesized that [^{177}Lu]-DUNP19 could overcome the heterogeneous expression of LRRC15 observed across tumor tissue and stroma (5). First, we evaluated the influence of antibody carrier mass on the biodistribution of [^{177}Lu]-DUNP19 in s.c. osteosarcoma (HuO9) tumors. We found that an injected antibody mass of 15-

30 µg yielded the optimal tumor-to-normal tissue radioactivity uptake ratios. Next, we systematically examined the biodistribution and pharmacokinetic profile of [¹⁷⁷Lu]-DUNP19 in a variety of s.c. tumor models originating from diverse malignant tissues. These studies evaluated multiple cancer lineages with various levels of LRRC15 expression and with target expression in distinct tumoral compartments. Tumor models with LRRC15+ cancer cells and CAFs included K7M2^{LRRC15+}, HuO9 and SAOS2 osteosarcomas (OS) and U118MG glioblastoma (GBM). We also assessed [¹⁷⁷Lu]-DUNP19 uptake in the HCC1954 breast cancer model, characterized by high LRRC15 expression in CAFs and LRRC15-null cancer cells. (Fig. 2, Supp. Fig. 3, 4).

The accumulation of [¹⁷⁷Lu]-DUNP19 in tumors peaked at 72 h post-injection (p.i.) (HCC1954: 12.5 ± 2.8 %IA/g [percent injected activity per gram tissue], U118MG: 13.3 ± 1.1 %IA/g, K7M2^{LRRC15+}: 13.6 ± 1.5 %IA/g, SAOS2: 23.1 ± 2.9 %IA/g, HuO9: 43.9 ± 7.9 %IA/g) and remained consistently elevated at all studied time points throughout the time course, out to 336 h p.i. (Fig. 2B). Retention of [¹⁷⁷Lu]-DUNP19 steadily decreased in blood and healthy organs after injection, and [¹⁷⁷Lu]-DUNP19 in blood reflected the expected half-life of a human IgG₁ in mice, indicating interaction with the murine neonatal fragment crystallizable (Fc) region receptor (FcRn) (13, 14). Retention of [¹⁷⁷Lu]-DUNP19 in the liver was representative of typical blood volume and metabolic elimination of antibodies. Taken together, these data indicate a favorable biodistribution profile of [¹⁷⁷Lu]-DUNP19 (Fig. 2D,E).

LRRC15 targeting specificity *in vivo* was further addressed in the s.c. LRRC15+ glioblastoma tumor model, U118MG. Uptake of [¹⁷⁷Lu]-DUNP19 was compared to nonspecific [¹⁷⁷Lu]-huIgG₁, a human IgG₁ with non-binding complementary-determining regions (CDRs)

that had been radiolabeled with ^{177}Lu . At 48 h post- i.v. administration, tumor uptake of [^{177}Lu]-DUNP19 was significantly higher than [^{177}Lu]-huIgG₁ (14.31 ± 2.01 vs. 4.72 ± 0.82 %IA/g, respectively). Additionally, in LRRC15- s.c. LNCaP tumors, which lack relevant amounts of murine LRRC15 expressing stroma but are highly vascularized, systemic injection of [^{177}Lu]-DUNP19 resulted in tumor retention of 6.57 ± 1.28 %IA/g at 48 h p.i. (Fig. 2B). These findings indicate that DUNP19 specifically targets LRRC15-expressing tumor tissue with minimal off-target retention *in vivo*. Accumulation of [^{177}Lu]-DUNP19 in LRRC15- LNCaP tumors is likely due to the enhanced permeability and retention effect. This pathophysiological mechanism involves the entrapment of macromolecules >45 kDa by the tumor vasculature, exhibiting a pronounced non-specific uptake of compounds in small animal xenograft tumor models as opposed to malignant lesions observed in humans (14, 15).

Next, we investigated the subcellular localization of DUNP19 in human osteosarcoma (SAOS2 and HuO9), and breast cancer (HCC1954) tumor models following systemic administration. Sections from s.c. tumors collected 72 h after i.v. injection of AlexaFluor647-labeled DUNP19 were co-stained for DNA, actin, and lysosomes (LAMP1) and analyzed by confocal microscopy (Fig. 2F,G, Supp. Fig. 4). Consistent with our *in vitro* findings, DUNP19 co-localized with murine LAMP1 in HCC1954 tumors, and with human LAMP1 in HuO9 and SAOS2 tumors. This co-localization suggests cellular internalization of the antibody after binding with LRRC15 on the plasma membrane of both cancer and stromal cells.

3.6 [^{177}Lu]-DUNP19 Radioimmunotherapy (RIT) of Aggressive Osteosarcoma

We then investigated the impact of [¹⁷⁷Lu]-DUNP19 radioimmunotherapy (RIT) on tumor volume and overall survival in mice bearing HuO9 osteosarcoma tumors. Following a single systemic administration of 30 MBq [¹⁷⁷Lu]-DUNP19, tumor growth was significantly inhibited ($P < 0.005$, Fig 3A_I). All mice treated with a single administration of 30 MBq [¹⁷⁷Lu]-DUNP19 survived through the entirety of the observation period (126 days) for initial tumor volumes in the 150-200 mm³ range. Infiltrative and bulky osteosarcoma have poorer prognoses and reduced treatment options. To test the impact of a larger tumor burden, a second group of animals with greater tumor volume (500-600 mm³) were treated with a single administration of 30 MBq [¹⁷⁷Lu]-DUNP19. Disease progression was again delayed relative to control, and overall survival was also improved to 115 days (67-126 days). All untreated animals succumbed by day 65 days (range: 58-69 days) (Fig 3A_{II}). Thus, irrespective of initial tumor volume, treatment with [¹⁷⁷Lu]-DUNP19 RIT was effective at significantly reducing disease progression and improving overall survival.

To investigate the efficacy of [¹⁷⁷Lu]-DUNP19 dosing regimens on tumor growth and survival, we conducted therapeutic fractionated dosing studies. From a translational perspective, this approach is commonly utilized in clinical settings to optimize maximum tolerated dose while reducing dose-limiting toxicities (16-18). Fractionation is also recommended to compensate for the anticipated heterogeneity in RIT dose distribution, particularly in large poorly vascularized tumors with regions of hypoxia (19). Rather than adhering to a predetermined activity and treatment schedule, additional therapeutic doses were given based on recovery from bone marrow toxicity determined by measuring differential blood counts, regrowth of tumor volume, and their effect on animal overall weight (Supp. Fig. 5,6). Mice bearing subcutaneous HuO9 tumors (150-200 mm³) were administered a cumulative activity of

50 MBq in three fractions over a span of 88 days (Fig. 3C_I). Continuous progression-free survival was sustained in treated animals throughout the study duration, contrasting to untreated animals which exhibited a median survival of 47 days (Fig. 3C_{II}).

We further studied LRRC15-targeted radio-theranostics in a translationally relevant orthotopic osteosarcoma model (Fig. 3B-D). HuO9 cells were injected into the left tibia of Balb/c mice and half of the subjects were randomly selected for systemic injection with 30 MBq of [¹⁷⁷Lu]-DUNP19 23 days after inoculation. Imaging by SPECT at 72 h post- [¹⁷⁷Lu]-DUNP19 administration revealed LRRC15-specific accumulation of activity at the tumor site (Fig. 3B). Of treated animals, 9 of 10 survived to study endpoint (190 d), while all untreated animals succumbed due to disease-related endpoints (Fig. 3B_I). Follow-up imaging with [¹⁷⁷Lu]-DUNP19 was acquired at 163 days after treatment and revealed no accumulation of the theranostic agent at the site of HuO9 tumor inoculation or at other anatomical locations (Fig. 3B_{II}). Based on these results, we concluded that the previously detected LRRC15+ tissue had been eradicated.

Radiation is widely known to induce calcifications in sarcomatous processes (20). To investigate this phenomenon in animals bearing HuO9 lesions, we quantified tumor radiopacity and uptake of tumor-associated [¹⁷⁷Lu]-DUNP19 using SPECT/CT and gamma-spectrometry. Animals treated with [¹⁷⁷Lu]-DUNP19 and untreated mice received an imaging dose of 3.5 MBq [¹⁷⁷Lu]-DUNP19 and tumors were harvested 72 hours after injection. Treated tumors exhibited significantly lower tumor-associated [¹⁷⁷Lu]-DUNP19 activity, coupled with higher levels of tumor calcification (Fig. 3C_{III-V}).

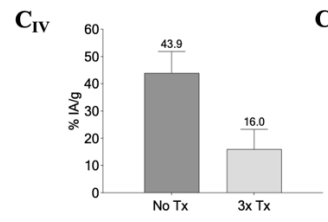
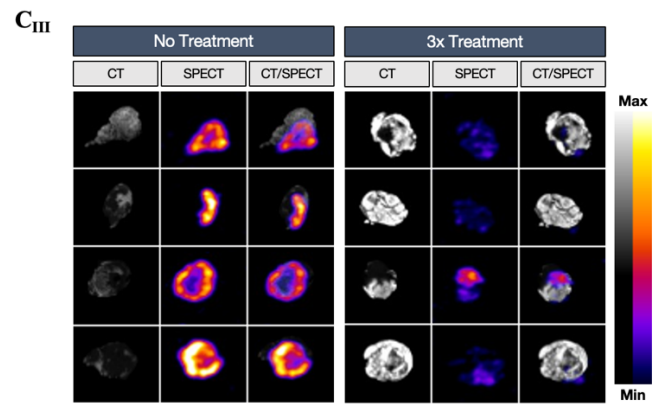
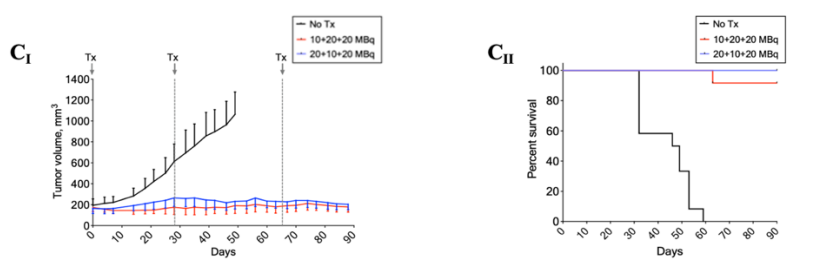
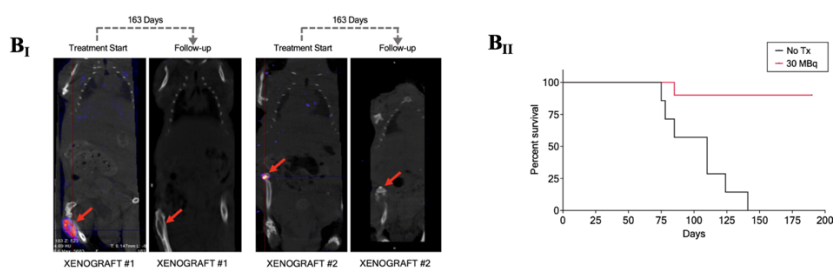
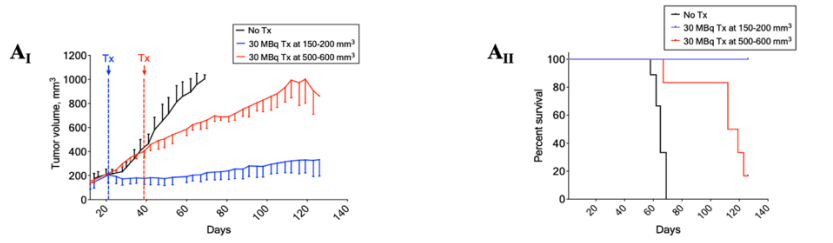


Figure 3. Evaluation of [¹⁷⁷Lu]-DUNP19 therapy and monitoring in HuO9 osteosarcoma tumors. **A_{I-II}.** Tumor volumes in mice bearing s.c. HuO9 xenografts (n=10 per arm) were randomized for a single i.v. administration of 30 MBq [¹⁷⁷Lu]-DUNP19 when tumors reached 203±64 mm³ (blue line; day 21) or 504±152 mm³ (red line; day 39) or received no treatment (black line). The results demonstrated a significant delay in disease progression, with treatment efficacy being influenced by tumor volume (**A_I**). Kaplan-Meier survival analysis revealed that [¹⁷⁷Lu]-DUNP19 extended survival, with the impact varying based on the timing of intervention (**A_{II}**). **B_{I-II}.** Representative coronal SPECT/CT images showing orthotopic HuO9 osteosarcoma tumors (indicated by arrow) after initial (left) and follow-up (right) i.v. administrations of 20 MBq [¹⁷⁷Lu]-DUNP19. In all treated mice (right) (n=10), no tumor associated uptake was observed at 163 days after treatment (**B_I**). Kaplan-Meier survival analysis revealed a significant increase in survival for the [¹⁷⁷Lu]-DUNP19 treated group during the observed 190-days period (**B_{II}**). **C_{I-V}.** Mice with s.c. HuO9 osteosarcoma xenografts (n=12 per arm) were randomized for three treatment cycles (red: 10+20+10 MBq; blue: 20+10+20 MBq) of i.v. [¹⁷⁷Lu]-DUNP19 (at day 0, 32, and 75), resulting in a total administered activity of 50 MBq, or no treatment (black; n=12). Assessment of tumor volumes demonstrated that repeated cycles of LRRC15-RIT effectively inhibit tumor growth (**C_I**). Kaplan-Meier survival analysis confirmed significantly improved survival for mice randomized for [¹⁷⁷Lu]-DUNP19 over no treatment (**C_{II}**). Four tumors from the treatment and control (non-treatment) arm, harvested 72 hours after administration of an imaging dose of [¹⁷⁷Lu]-DUNP19 (3 MBq), were imaged ex vivo by SPECT and CT (**C_{III}**). Tissue activity levels (%IA/g), assessed by gamma counter and normalized to tissue weight, revealed significantly lower uptake of the antibody in treated vs. non-treated tumors (p < 0.001), reflecting reduction in total LRRC15-expressing cells post-treatment (**C_{IV}**).

Quantification of radiopacity in CT images showed significantly higher ossification levels in treated vs. non-treated tumor tissues ($p < 0.001$) (Cv). Together, these findings illustrate that repeated cycles of [^{177}Lu]-DUNP19 effectively reduce tissue viability and calcification.

3.7 [^{177}Lu]-DUNP19 Therapy is Effective Across a Range of Tumors with Varying LRRC15 Expression Patterns

Given the high expression of LRRC15 on HuO9 osteosarcoma cells (Fig. 1), we also sought to understand how the effects of [^{177}Lu]-DUNP19 therapy would change in a tumor of different tissue origin and with lower LRRC15 expression. Mice bearing s.c. tumors from glioblastoma U118MG cells were treated with a cumulative activity of 20 MBq or 30 MBq [^{177}Lu]-DUNP19 in two fractions. [^{177}Lu]-DUNP19 treatment significantly extended survival ($p < 0.0001$), and therapy prevented further tumor growth as tumor volumes reached a plateau phase around 100-200 mm³. All untreated mice succumbed due to disease-related endpoints by 78 days, whereas 11/12 mice (91.67 %) and 12/12 mice (100%) were alive at the end of the observation period in the 20 MBq and 30 MBq treatment groups, respectively (Fig. 4A, B).

Finally, we evaluated the therapeutic efficacy of [^{177}Lu]-DUNP19 in aggressive breast cancer tumors comprising LRRC15- HCC1954 cancer cells and LRRC15+ murine CAFs. Despite LRRC15 expression in stroma only, a single systemic injection of 20 MBq [^{177}Lu]-DUNP19 effectively suppressed HCC1954 tumor growth and significantly prolonged median survival compared to untreated mice, where median survival was 30.5 days ($p = 0.0005$; median survival not reached in treated animals). Notably, 80% of the treated mice (8 out of 10) survived until the end of the observation period (Fig. 4C, D). Given the lack of target expressing cancer

cells, the response of HCC1954 tumors to [¹⁷⁷Lu]-DUNP19 is reliant on targeting of LRRC15+ murine CAFs. We presume that the therapeutic impact results from the synergy of two components: the direct induction of DNA damage by beta-particles, affecting both stromal and cancer cells, as well as the ablation of tumor-supporting stromal tissue on which cancer cells depend for growth and survival.

Throughout all studies, treatment was well-tolerated as indicated by stable body weights (Supp. Fig. 5). Administration of [¹⁷⁷Lu]-DUNP19 resulted in a transient bone marrow suppression, which recovered to baseline levels within 21 days (Supp. Fig. 6).

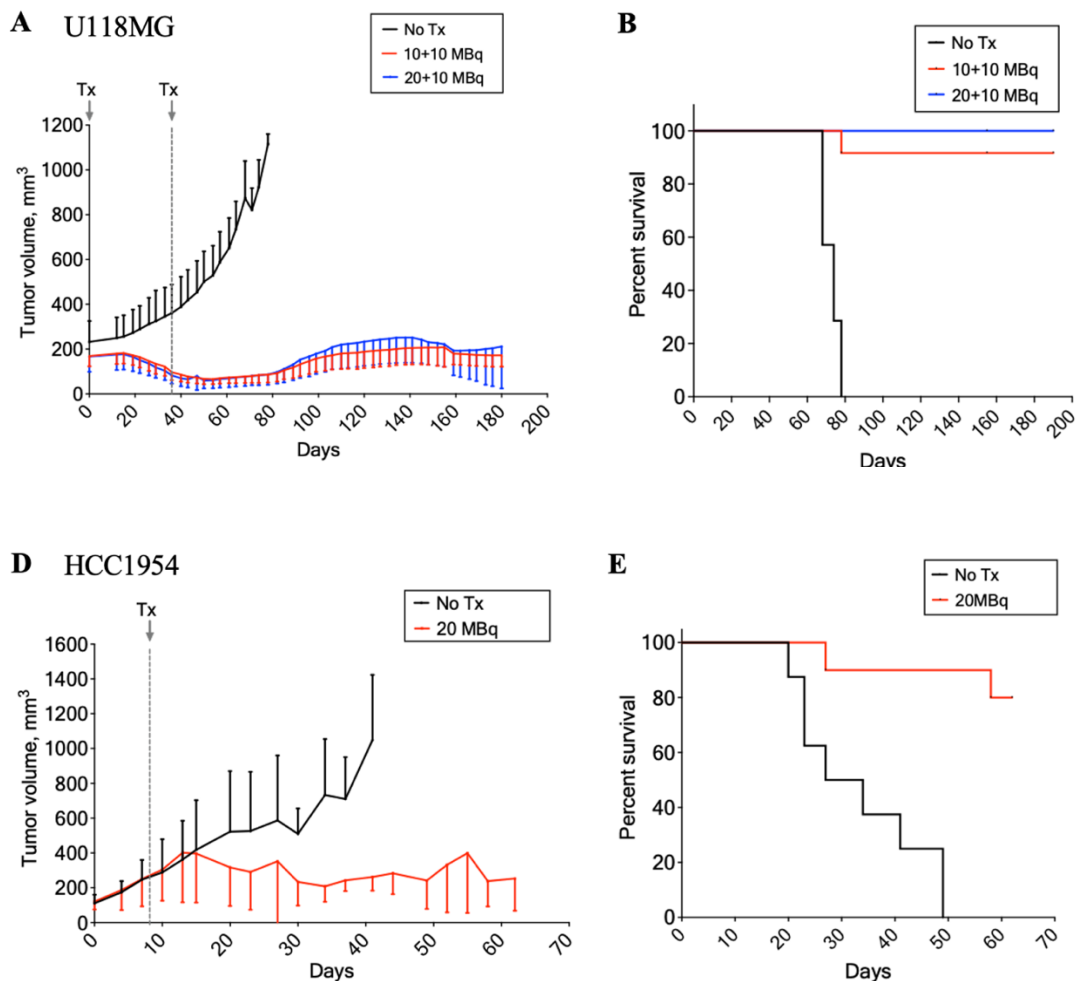


Figure 4. Therapeutic efficacy of [¹⁷⁷Lu]-DUNP19 in LRRC15-expressing human xenograft models. **A, B.** [¹⁷⁷Lu]-DUNP19 demonstrates antitumor activity in other cancer indications. BALB/c nude mice bearing s.c. U118MG glioblastoma xenografts (were treated with two fractions of [¹⁷⁷Lu]-DUNP19 at days 0 and 34 for a cumulative activity of 20 MBq (10+10 MBq, red, n=12) or 30 MBq (20+10 MBq, blue, n=11). Despite lower LRRC15 expression by U118MG tumors, treatment with [¹⁷⁷Lu]-DUNP19 significantly controlled tumor growth and prolonged survival in both [¹⁷⁷Lu]-DUNP19 doses (median survival; untreated = 74 days, 20 MBq = not reached, 30 MBq = not reached, $p < 0.001$). **C, D.** [¹⁷⁷Lu]-DUNP19 is effective in HCC1954 breast cancer models (LRRC15- cancer cells, LRRC15+ stroma). Results demonstrate delayed s.c. HCC1954 growth in female mice intravenously administered a single dose of [¹⁷⁷Lu]-DUNP19 (20 MBq; day 7, n=10). **D.** Median survival was not reached for the treated group by the end of the observation period (day 62), while median survival of treated mice was 30.5 days ($p < 0.005$).

3.8 LRRC15-targeted RIT Depletes TGF β -Driven Signature in Tumors

Having demonstrated the significant therapeutic potential of our radio-immunotheranostic platform, we sought to understand the molecular effects of LRRC15-targeted RIT on cancer cells and the tumor microenvironment. Transcripts of bulk RNA-sequencing of tumors harvested at 90-155 days after [¹⁷⁷Lu]-DUNP19 treatment were aligned to human and murine genomes to identify the transcriptomic profiles of human cancer cells and murine stromal cells. Ambiguous reads were subsequently removed (Fig. 5A).

Due to the fractionated dosing regimens utilized in our therapeutic studies (Fig. 3, 4), our first objective was to determine whether there were significant differences in tumor gene signatures when comparing [¹⁷⁷Lu]-DUNP19 dosing regimens. However, we did not find gene signatures that were associated with the [¹⁷⁷Lu]-DUNP19 radiation dose received. Therefore, tumor samples were not separated by [¹⁷⁷Lu]-DUNP19 radiation dose received in subsequent analyses and for each model, [¹⁷⁷Lu]-DUNP19-treated tumors were compared to untreated tumors.

In human cancer cells, RNA-sequencing analysis identified 19,578 protein-coding genes, of which 1,985 (HuO9), 1,043 (U118MG), and 23 (HCC1954) were differentially expressed genes (DEGs) after [¹⁷⁷Lu]-DUNP19 therapy. In [¹⁷⁷Lu]-DUNP19-treated murine stroma, 663 (HuO9), 319 (U118MG), and 73 (HCC1954) DEGs were identified compared to untreated controls (Fig. 5B). In U118MG tumors, the most upregulated genes included bone morphogenic protein (*BMP2*) and inhibin subunit beta A (*INHBA*), two modulators of TGFβ signaling and epithelial-mesenchymal transition (Fig. 5B). In HuO9 tumors, epigenetic modulators such as *HINFP* and *H4C11* were upregulated, while anti-apoptotic genes (*HRK*) and genes in the canonical pro-tumorigenic WNT and RAS pathways were among the most significantly downregulated genes after DUNP19 RIT (Fig. 5B).

To gain a sense of the biological pathways altered by DUNP19 RIT, gene ontology analysis of DEGs from tumors containing LRRC15+ cancer cells (U118MG, HuO9) was performed (Fig. 5C,D). In treated U118MG tumors, gene ontology terms were immune- and epithelial-mesenchymal transition related (response to cortisol, myeloid leukocyte mediated immunity, anatomical structural development) (Fig. 5C). Further analysis using gene set enrichment

analysis (GSEA) of genes ranked by fold-change (\log_2FC) revealed enrichment of myogenesis (myoblast stem cell differentiation) and a downregulation of MYC target genes (Fig. 5C, Supp. Table 1). In contrast, GSEA and gene ontology analysis of treated HuO9 tumors revealed alterations in metabolic and cell cycle-related pathways, as indicated by negative enrichment of E2F cell cycle transcription factors, as well as alterations in nitrate metabolism, lipoprotein homeostasis, and response to stress (Fig. 5F, Supp. Table 1). Despite differences in the biological pathways involved in DUNP19 RIT response, 40 genes were differentially expressed in both U118MG and HuO9 treated tumors (Fig. 5E,F). This was surprising given the different origins and different cell lineages of the two models. Of the 40 shared genes, several had functions similar to the hypothesized roles of *LRRC15* (cell migration, invasion, and adhesion) or had been shown to be co-expressed with *LRRC15*, including *COL11A1*, *FGF13*, and *CXCL14* (Fig. 5E,F) (8, 21).

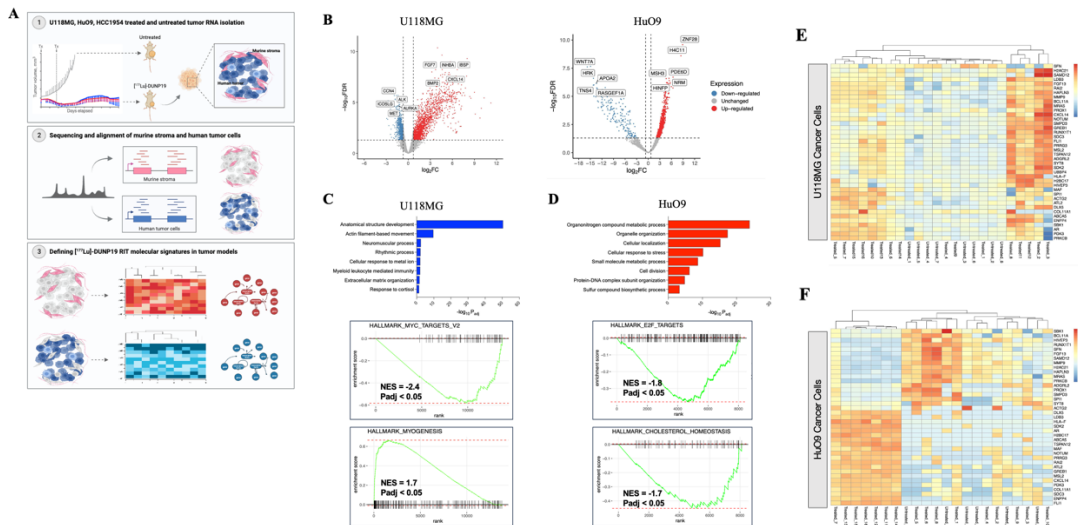


Figure 5. $[^{177}\text{Lu}]$ -DUNP19 induced radioimmunotherapy signatures in *LRRC15*+ cancer cells. A. Schematic of transcriptomic analysis of HuO9, U118MG, and HCC1954 tumors after

[¹⁷⁷Lu]-DUNP19 treatment. Treated or untreated tumor samples were harvested for RNA isolation, before sequencing and alignment to either murine or human genomes. Overlapping or ambiguous reads were discarded. **B.** Volcano plot of the top up- (red) and downregulated (blue) DEGs after treatment with [¹⁷⁷Lu]-DUNP19 in U118MG (left) and HuO9 (right) cancer cells (FDR < 0.05). DEGs were ranked by fold-change. The top and bottom genes were labeled. **C,** **D.** Gene ontology (GO) biological pathway enrichment analysis of DEGs in treated (**C**) U118MG and (**D**) HuO9 cancer cells (adjusted p-value < 0.05). Enriched biological pathways with more than 10 overlapping terms (genes) were plotted by Padj value to indicate processes most significantly enriched after [¹⁷⁷Lu]-DUNP19 RIT. **E, F.** Overlapping differentially expressed genes (40 genes, FDR < 0.05, FC > 1) in (**E**) U118MG and (**F**) HuO9 cancer cells after [¹⁷⁷Lu]-DUNP19 treatment were plotted for visualization of [¹⁷⁷Lu]-DUNP19-induced changes. Relative expression per gene was plotted to indicate up- (in red) or downregulated (blue) genes by Z-score normalization.

To complement our understanding of transcriptomic responses by DUNP19 RIT in the tumor microenvironment, we also conducted a comprehensive analysis of the murine stroma in HuO9, U118MG, and HCC1954 tumors. In all three models, RIT induced changes in pathways related to immune activation, including the upregulation of *Gzmk*, *Cxcr6*, and *Lck* (Fig. 6A-C). Whole transcriptome principal component analysis identified three distinct transcriptional clusters for treated cancer cells in the HuO9 and U118MG models and two clusters in HCC1954 (Supp. Fig. 7). Based on these results, we studied whether these changes could be explained by an overall shift in cell types present within the [¹⁷⁷Lu]-DUNP19 treated tumor samples (i.e. loss of

mesenchymal phenotypes). We employed Syllolist to further assess the proportional distribution of cell types in treated tumors compared to untreated samples (22). In accordance with the expression of *LRRC15* in cancer cells originating from mesenchymal stem cells, HuO9 and U118MG tumors displayed a notable overrepresentation of mesenchymal cells across all examined samples, with a significant loss of the mesenchymal cell phenotype in DUNP19-treated HuO9 cancer cells (Supp. Fig 8). No discernible alterations in relative cell composition were observed following treatment with [¹⁷⁷Lu]-DUNP19 in other tumor models. Additionally, our observations revealed that HCC1954 tumor cells predominantly maintained an epithelial phenotype, consistent with the absence of *LRRC15* expression in the cancer cells (Supp. Fig 8).

Overall, and in line with plasma membrane associated LRRC15 protein levels (Fig. 1B,C), *LRRC15* expression was higher in HuO9 than in U118MG cancer cells, and not quantifiable in HCC1954 cancer cells. In contrast, stromal *Lrrc15* expression was 3- and 4-fold higher in HCC1954 tumors than in U118MG and HUO9 tumors, respectively (Supp. Fig. 9). Comparison of *LRRC15/Lrrc15* expression in cancer cells and stroma of HuO9 and U118MG tumors across clusters showed a trend of decreased expression with increasing cluster distance from untreated samples in both cancer cells and stroma (Fig. 6D); the expression of *TGFBI*, a known regulator of LRRC15 expression, mirrored the *LRRC15/Lrrc15* expression pattern (Fig. 6D). Interestingly, *Lrrc15* and *Tgfb1* levels in HCC1954 stroma remained constant, while *TGFBI* expression was increased in treated LRRC15-null HCC1954 cancer cells.

Further analysis of LRRC15+ clusters showed that treatment with [¹⁷⁷Lu]-DUNP19 resulted in the progressive loss of a gene signature associated with immune cell exclusion and poor response to immune checkpoint blockade in TGFβ-driven, LRRC15+ CAFs (4, 8) (Fig. 6E,F).

therapy. HuO9 transcripts are plotted in red (left), U118MG in blue (middle), and HCC1954 in black (right). Samples were separated by transcript signature based on PCA plots and hierarchical clustering (Supp. Fig. 7) into 2 (HCC1954) or 3 (U118MG, HuO9) clusters. Expression of *LRRC15* and *TGFBI* in treated samples from cluster 3 are significantly ($p < 0.005$) decreased in U118MG and HuO9, while no changes are observed in the LRRC15- HCC1954 cancer cells. **E, F.** Transcript data from clustered (Supp. Fig. 7) cancer cells (**E**) or tumor stroma (**F**) show decreased expression of the LRRC15+ TGF β signature. **E.** Untreated U118MG (top) and HuO9 (middle) cancer cells lose expression of the LRRC15+ TGF β signature after [^{177}Lu]-DUNP19 treatment (red = high, blue = low expression). **F.** Loss of the LRRC15+ TGF β signature is observed across all tumor stroma after [^{177}Lu]-DUNP19 RIT (green = high, orange = low expression) **G.** HCC1954 tumors that were resistant to [^{177}Lu]-DUNP19 treatment (defined as reaching 1000m³ endpoint before conclusion of study) had no significant reduction of the 11-gene LRRC15+ TGF β signature within tumor stroma.

3.9 Discussion

LRRC15 has emerged as a promising TGF β -driven biomarker expressed on the cell membrane of cancer cells derived from mesenchymal stem cells and on a subset of cancer-associated fibroblasts within the tumor microenvironment (4, 8). Studies evaluating genes associated with metastatic progression have characterized LRRC15's role in metastases to bone in breast cancer and to bowel in ovarian cancer, while LRRC15 knockdown by siRNA significantly inhibits tumor progression in preclinical models (23). Furthermore, a retrospective

study assessing primary osteosarcoma lesions identified a correlation between LRRC15 expression, aggressive disease, and shorter overall survival (9).

The novel technology presented here harnesses the unique characteristics of a humanized IgG₁ antibody, DUNP19, to specifically bind to a phylogenetically stable epitope of LRRC15. The rapid cellular internalization of DUNP19 exhibited by LRRC15-expressing cells provides an optimal foundation for leveraging DUNP19 as an effective vehicle for delivery of radionuclides to target cells. In this investigation, we have also substantiated DUNP19's versatility by demonstrating its functionalization with both diagnostic and therapeutic radioisotopes. The radiolabeled modality facilitates identification of patients harboring LRRC15+ lesions, allowing for precise therapeutic intervention via molecularly specific PET or SPECT imaging. Subsequently, patients with LRRC15+ tissues can be selected for personalized therapeutic dosing, delivering tumor-specific ionizing radiation with minimal off-target effects. A similar approach is currently used in clinical practice, with examples including the application of radioactive iodine in thyroid cancer therapy and the use of radioligands binding to specific membrane antigens, such as [¹⁷⁷Lu]-PSMA-617 for prostate-specific membrane antigen and [¹⁷⁷Lu]-DOTATATE for somatostatin receptors. Patients exhibiting high tumoral uptake of the diagnostic radioligand on PET/CT imaging, reflecting elevated target expression and successful drug delivery, are deemed eligible for treatment with these therapeutic radioligands.

Our LRRC15-RIT approach exhibited effective targeting across various cancer models, including models of breast cancer, osteosarcoma, and glioblastoma, all representing highly lethal cancers with distinct tumor biology and LRRC15 expression patterns. Notably, the specific depletion of LRRC15+ cancer and stromal cells through a single systemic administration of

[¹⁷⁷Lu]-DUNP19 significantly slowed tumor progression and conferred a survival benefit in all models. These outcomes align with previous observations where the genetic ablation of LRRC15⁺ CAFs in murine models of pancreatic adenocarcinoma significantly reduced tumor volume and slowed tumor growth (8). Moreover, our findings underscore the practicality of directing therapeutic efforts towards LRRC15-deficient tumor cells via the crossfire phenomenon. Upon binding of [¹⁷⁷Lu]-DUNP19 with adjacent LRRC15-expressing CAFs, the decay of ¹⁷⁷Lu can instigate DNA breaks spanning multiple cell diameters. These crossfire effects can significantly improve responses in tumors with low or heterogeneous target expression (24, 25). The strategic application of a ¹⁷⁷Lu antibody-conjugate addresses the challenge of heterogeneous LRRC15 expression within tumor tissue, thereby enhancing the therapeutic efficacy of the treatment. DUNP19 also binds to an epitope shared by human and murine LRRC15 and we do not expect the antibody to demonstrate vastly different biodistribution upon translation to patients. Moreover, *in vivo* cellular internalization, as observed for the DUNP19-based radioconjugate, has been reported to enhance radioisotope retention and reduce extracellular shedding of the radioisotope (26). In agreement with other beta-emitting RIT, we noted a decrease in white and red blood cells after administration of [¹⁷⁷Lu]-DUNP19 (27). However, the bone marrow recovered within an expected time frame after treatment injection, allowing for serial dosing.

The LRRC15 protein is representative of a distinct set of TGFβ-driven genes that are predictors of immune checkpoint blockade resistance and unfavorable tumor evolution (4, 8). Given LRRC15's known association with TGFβ, immunosuppression, and the observed potential immunomodulatory effects of RIT (28), our second aim was to explore whether the anti-tumor activity induced by [¹⁷⁷Lu]-DUNP19 could reverse the signaling profile associated

with immunosuppression and resistance to immunotherapy. To target tumor-supporting immunosuppressive stroma, many investigations have focused on fibroblast activation protein- α (FAP), a membrane bound serine protease overexpressed by CAFs (29). However, normal tissues and healthy activated fibroblasts also express FAP during wound healing, such as the activation of myofibroblasts post-myocardial infarction. While both LRRC15 and FAP have been shown to be upregulated by TGF β (30), recent studies revealed a unique subset of TGF β -driven CAFs that express LRRC15 and are negative for FAP expression (4, 8), and that these LRRC15+ CAFs are associated with CD8+ T-cell exclusion (8). During our therapeutic studies, a notable observation emerged: LRRC15+ tumors exhibited a concurrent reduction in both growth and the TGF β –LRRC15 gene signature upon exposure to RIT. However, within a small subset (2 out of 12) of LRRC15- breast cancer (HCC1954) cases, tumor volumes did not decrease following the administration of [¹⁷⁷Lu]-DUNP19. Moreover, this subset exhibited a persistent TGF β –LRRC15 signature, suggesting a nuanced response within this specific context.

We also show that LRRC15-targeted RIT leads to differential expression of genes in stromal cells related to immune cell function, including genes indicative of activation and proliferation of T-cells (*Cd3*, *Cd8*, *Gimap7*, *Gzmk*, *Lat*, *Lck*, *Eomes*) and natural killer cells (*Cxcr6*, *Eomes*, *Prf1*). In the stroma of U118MG tumors, the T-cell suppressor gene encoding PD-1 was downregulated, suggesting that [¹⁷⁷Lu]-DUNP19 may contribute to relief of immune cell suppression and T-cell exclusion, and that immune-based adjuvant therapies may be complementary to LRRC15-RIT. The transcriptomic remodeling of immune-related signaling pathways and expression of immune activating cytokines after RIT may increase immune cell activation and infiltration in previously immunologically “cold” tumors. Additionally, ablation of radio-resistant stroma may further increase immune cell invasion and help amplify the anti-

tumor immune response, but future studies in immunocompetent mouse models will be required to investigate [¹⁷⁷Lu]-DUNP19 RIT's effects on the adaptive immune system and potential synergies with immunotherapies.

In the broader context of cancer treatment, our findings provide a novel technique for non-invasive imaging and treatment of a wide range of aggressive tumors with limited options for targeted therapy. Critically, we demonstrate that [¹⁷⁷Lu]-DUNP19 therapy can be effective despite heterogeneous LRRC15 expression within tumor tissue and that targeted radiation by [¹⁷⁷Lu]-DUNP19 treatment is not limited to LRRC15+ tumor cells, taking advantage of the crossfire effects of beta-radioimmunotherapy. In addition, LRRC15's regulation by TGFβ allows for successful targeting of pro-tumorigenic TGFβ signaling mechanisms that have been shown to contribute to immunotherapy resistance and poor prognosis. We show, at a transcriptomic level, that these TGFβ-LRRC15 signatures are largely erased in [¹⁷⁷Lu]-DUNP19-treated tumors and expression of other anti-tumor immune pathways increases. Based on these observations, we hypothesize that the eradication of this TGFβ-LRRC15 signature in tumor cells would be synergistic with existing immunotherapies and allow for immune cell infiltration, as demonstrated by Krishnamurty et al (8). However, this remains an open question, as more advanced syngeneic models will be required to answer questions about immune functionality after LRRC15-targeted RIT. In summary, we propose targeting LRRC15+ cells with [¹⁷⁷Lu]-DUNP19 as a novel theranostic strategy that provides sustained tumor control across models of LRRC15+ disease, improves survival, and reprograms the transcriptomic landscape of pro-tumorigenic and immunosuppressive mechanisms within the TME, all with minimal side effects.

3.10 References

1. Jin S, Sun Y, Liang X, Gu X, Ning J, et al. Emerging new therapeutic antibody derivatives for cancer treatment. *Signal Transduct Target Ther* 2022;7:39
2. Bejarano L, Jordão MJC, Joyce JA. Therapeutic Targeting of the Tumor Microenvironment. *Cancer Discov* 2021;11:933-959
3. Van der Heide CD, Dalm SU. Radionuclide imaging and therapy directed towards the tumor microenvironment: a multi-cancer approach for personalized medicine. *EJNMMI* 2022;49:4616-4641
4. Dominguez CX, Muller S, Keerthivasan S, Koeppen H, Hung J, Gierke S, et al. Single-Cell RNA Sequencing Reveals Stromal Evolution into LRRC15(+) Myofibroblasts as a Determinant of Patient Response to Cancer Immunotherapy. *Cancer Discov* 2020;10:232-53
5. Purcell JW, Tanlimco SG, Hickson J, Fox M, Sho M, Durkin L, et al. LRRC15 Is a Novel Mesenchymal Protein and Stromal Target for Antibody-Drug Conjugates. *Cancer Res* 2018;78:4059-72
6. Wang Y, Liu Y, Zhang M, Lv L, Zhang X, Zhang P, Zhou Y. LRRC15 promotes osteogenic differentiation of mesenchymal stem cells by modulating p65 cytoplasmic/nuclear translocation. *Stem Cell Res Ther* 2018;9:65
7. Yang Y, Wu H, Fan S, Bi Y, Hao M, Shang J. Cancer-associated fibroblast-derived LRRC15 promotes the migration and invasion of triple-negative breast cancer cells via Wnt/beta-catenin signalling pathway regulation. *Mol Med Rep* 2022;25
8. Krishnamurty AT, Shyer JA, Thai M, Gandham V, Buechler MB, Yang YA, et al. LRRC15(+) myofibroblasts dictate the stromal setpoint to suppress tumour immunity. *Nature* 2022;611:148-54

9. Cui J, Dean D, Wei R, Hornicek FJ, Ulmert D, Duan Z. Expression and clinical implications of leucine-rich repeat containing 15 (LRRC15) in osteosarcoma. *J Orthop Res* 2020;38:2362-72
10. Ghandi, M., Huang, F.W., Jané-Valbuena, J. et al. Next-generation characterization of the Cancer Cell Line Encyclopedia. *Nature* 2019;569, 503-08
11. McDevitt MR, Thorek DLJ, Hashimoto T, Gondo T, Veach DR, Sharma SK, et al. Feed-forward alpha particle radiotherapy ablates androgen receptor-addicted prostate cancer. *Nat Commun* 2018;9:1629
12. Kurth J, Krause BJ, Schwarzenbock SM, Stegger L, Schafers M, Rahbar K. External radiation exposure, excretion, and effective half-life in (177)Lu-PSMA-targeted therapies. *EJNMMI Res* 2018;8:32
13. Deng R, Meng YG, Hoyte K, Lutman J, Lu Y, Iyer S, et al. Subcutaneous bioavailability of therapeutic antibodies as a function of FcRn binding affinity in mice. *MAbs* 2012;4:101-9
14. Thorek DLJ, Watson PA, Lee SG, Ku AT, Bournazos S, et al. Internalization of secreted antigen-targeted antibodies by the neonatal Fc receptor for precision imaging of the androgen receptor axis. *Sci Transl Med* 2016;8:367
15. Shi Y, van der Meel R, Chen X, Lammers T. The EPR effect and beyond: Strategies to improve tumor targeting and cancer nanomedicine treatment efficacy. *Theranostics* 2020;10:7921-7924
16. Illidge TM, Bayne M, Brown NS, Chilton S, Cragg MS, Glennie MJ, et al. Phase 1/2 study of fractionated (131)I-rituximab in low-grade B-cell lymphoma: the effect of prior rituximab dosing and tumor burden on subsequent radioimmunotherapy. *Blood* 2009;113:1412-21
17. Schlom J, Molinolo A, Simpson JF, Siler K, Roselli M, Hinkle G, et al. Advantage of dose fractionation in monoclonal antibody-targeted radioimmunotherapy. *J Natl Cancer Inst* 1990;82:763-71
18. Linden O, Hindorf C, Cavallin-Stahl E, Wegener WA, Goldenberg DM, Horne H, et al. Dose-fractionated radioimmunotherapy in non-Hodgkin's lymphoma using DOTA-conjugated,

90Y-radiolabeled, humanized anti-CD22 monoclonal antibody, epratuzumab. *Clin Cancer Res* 2005;11:5215-22

19. DeNardo GL, Schlom J, Buchsbaum DJ, Meredith RF, O'Donoghue JA, Sgouros G, et al. Rationales, evidence, and design considerations for fractionated radioimmunotherapy. *Cancer* 2002;94:1332-48

20. Kreel L, Bydder G. Tumor calcification after radiotherapy demonstrated by computed tomography. *J Comput Tomogr* 1980;4:245-9

21. Guderian RH, Chico ME, Rogers MD, Pattishall KM, Grogl M, Berman JD. Placebo controlled treatment of Ecuadorian cutaneous leishmaniasis. *Am J Trop Med Hyg* 1991;45:92-7

22. Lu IN, Dobersalske C, Rauschenbach L, Teuber-Hanselmann S, Steinbach A, et al. Tumor-associated hematopoietic stem and progenitor cells positively linked to glioblastoma progression. *Nat Commun* 2021;12(1):3895

23. Mariani A, Wang C, Oberg AL, Riska SM, Torres M, Kumka J, et al. Genes associated with bowel metastases in ovarian cancer. *Gynecol Oncol* 2019;154:495-504

24. Irvani A, Violet J, Azad A, Hofman MS. Lutetium-177 prostate-specific membrane antigen (PSMA) theranostics: practical nuances and intricacies. *Prostate Cancer Prostatic Dis* 2020;23:38-52

25. Seifert R, Kessel K, Schlack K, Weckesser M, Kersting D, et al. Total tumor volume reduction and low PSMA expression in patients receiving Lu-PSMA therapy. *Theranostics* 2021;11:8143-51

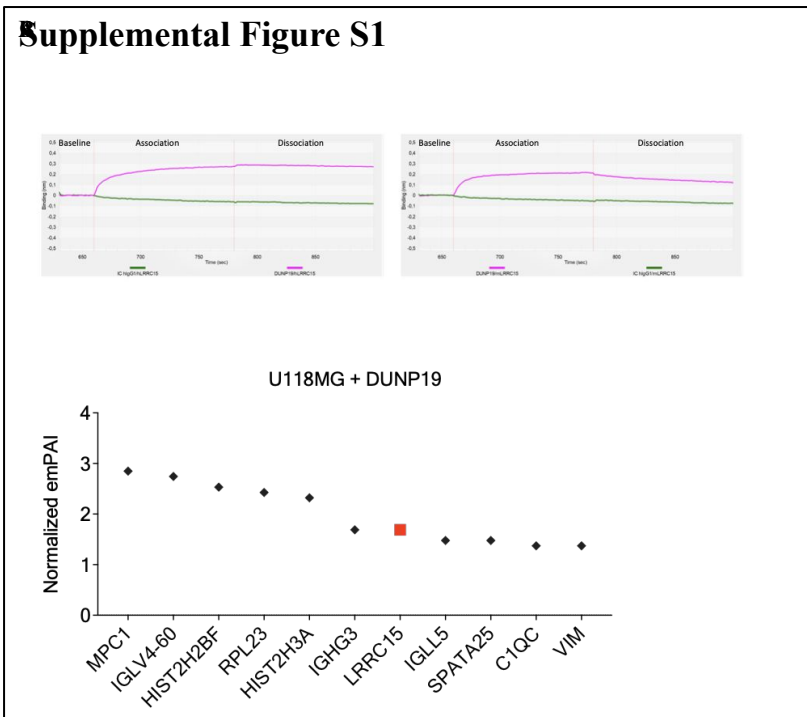
26. Edwards WB, Xu B, Akers W, Cheney PP, Liang K, Rogers BE, et al. Agonist-antagonist dilemma in molecular imaging: evaluation of a monomolecular multimodal imaging agent for the somatostatin receptor. *Bioconjug Chem* 2008;19:192-200

27. Bodei L, Kidd M, Paganelli G, Grana CM, Drozdov I, Cremonesi M, et al. Long-term tolerability of PRRT in 807 patients with neuroendocrine tumours: the value and limitations of clinical factors. *Eur J Nucl Med Mol Imaging* 2015;42:5-19
28. Kleinendorst SC, Oosterwijk E, Bussink J, Westdorp H, Konijnenberg MW, Heskamp S. Combining Targeted Radionuclide Therapy and Immune Checkpoint Inhibition for Cancer Treatment. *Clin Cancer Res* 2022;28:3652-7
29. Hofheinz RD, al-Batran SE, Hartmann F, Hartung G, Jager D, Renner C, et al. Stromal antigen targeting by a humanised monoclonal antibody: an early phase II trial of sibrotuzumab in patients with metastatic colorectal cancer. *Onkologie* 2003;26:44-8
30. Juillerat-Jeanneret L, Tafelmeyer P, Golshayan D. Regulation of Fibroblast Activation Protein- α Expression: Focus on Intracellular Protein Interactions. *J Med Chem* 2021;64(19):14028-14045
31. Westerlund K, Altai M, Mitran B, Konijnenberg M, Oroujeni M, Atterby C, et al. Radionuclide Therapy of HER2-Expressing Human Xenografts Using Affibody-Based Peptide Nucleic Acid-Mediated Pretargeting: In Vivo Proof of Principle. *J Nucl Med* 2018;59:1092-8
32. Bondza S, Foy E, Brooks J, Andersson K, Robinson J, Richalet P, Buijs J. Real-time Characterization of Antibody Binding to Receptors on Living Immune Cells. *Front Immunol* 2017;8:455
33. Have S, Boulon S, Ahmad Y, Lamond AI. Mass spectrometry-based immuno-precipitation proteomics - the user's guide. *Proteomics* 2011;11:1153-9
34. Lagundzin D, Krieger KL, Law HC, Woods NT. An optimized co-immunoprecipitation protocol for the analysis of endogenous protein-protein interactions in cell lines using mass spectrometry. *STAR Protoc* 2022;3:101234
35. Dobin A, Davis CA, Schlesinger F, Drenkow J, Zaleski C et al. STAR: ultrafast universal RNA-seq aligner. *Bioinformatics* 2013;29:15–21

36. Robinson MD, McCarthy DJ, Smyth GK. edgeR: a Bioconductor package for differential expression analysis of digital gene expression data. *Bioinformatics* 2010;26:139-40

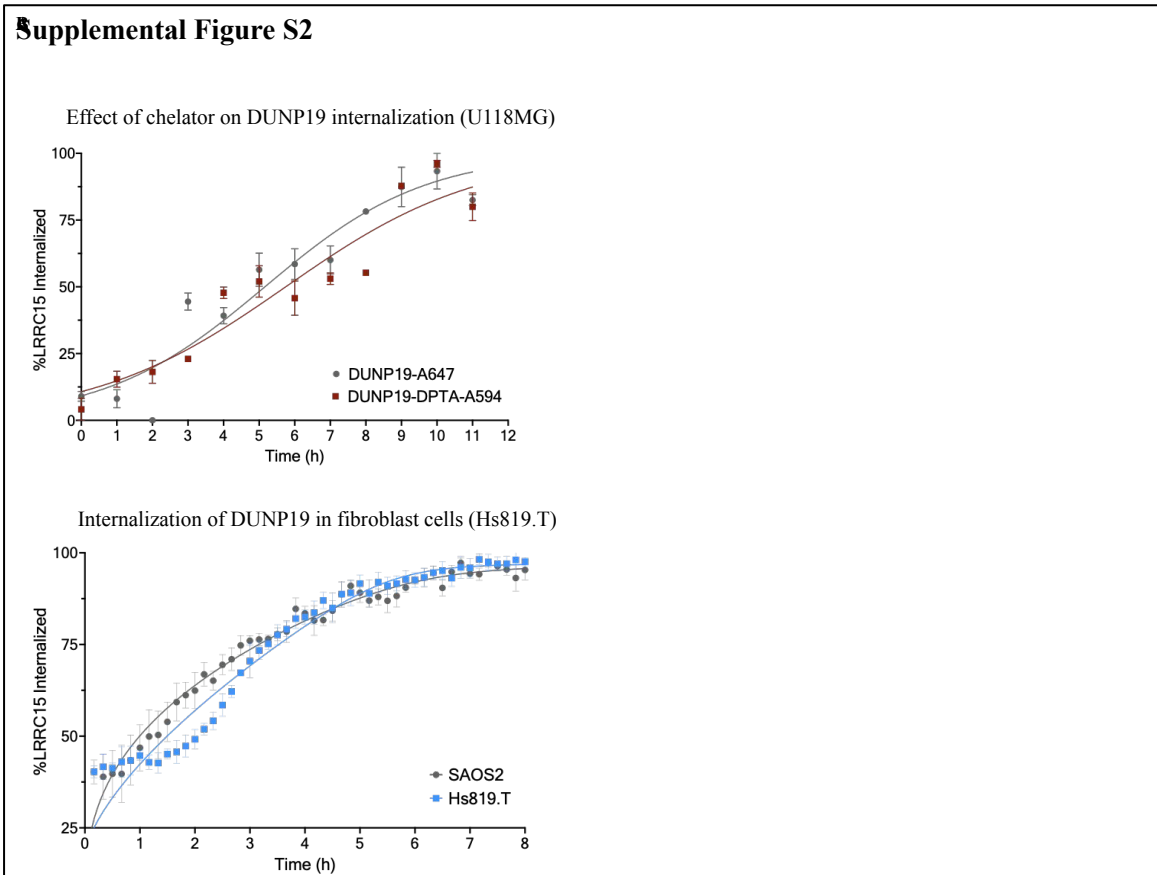
37. Liberzon A, Birger C, Thorvaldsdottir H, Ghandi M, Mesirov JP, Tamayo P. The Molecular Signatures Database (MSigDB) hallmark gene set collection. *Cell Syst* 2015;1:417-25

3.11 Supplementary Figures



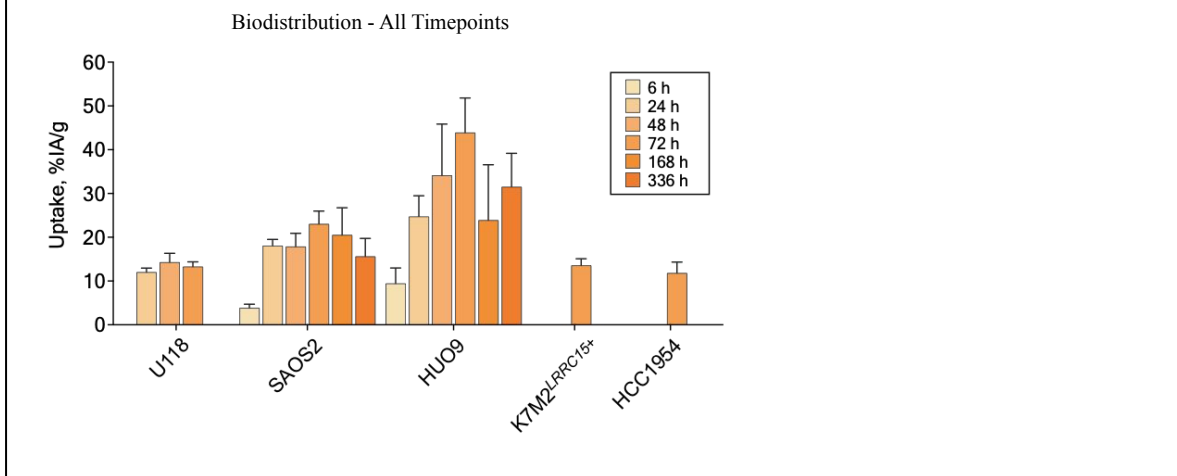
Supplemental Figure 1. DUNP19 binds to human and murine LRRC15 protein. **A.** DUNP19 binding kinetics to human (left) and murine (right) LRRC15 recombinant protein using the Bio-Layer Interferometry Octet system. Association of 100ug/mL DUNP19 (pink trace) or 100ug/mL IgG1 isotype control (green trace) are shown in real time over 850 s. Association and dissociation of DUNP19 to hLRRC15 or mLRRC15 is measured by binding rate (nm). **B.** The 11 unique proteins present after an immunoprecipitation-mass spectrometry (IP-MS) analysis of crude protein lysates from U118MG cells incubated with Protein G magnetic bead-conjugated DUNP19. Pulldown-MS composition was compared to protein composition present in non-

specific IgG1 with U118MG lysates. LRRC15 is among the top proteins in complex with DUNP19.



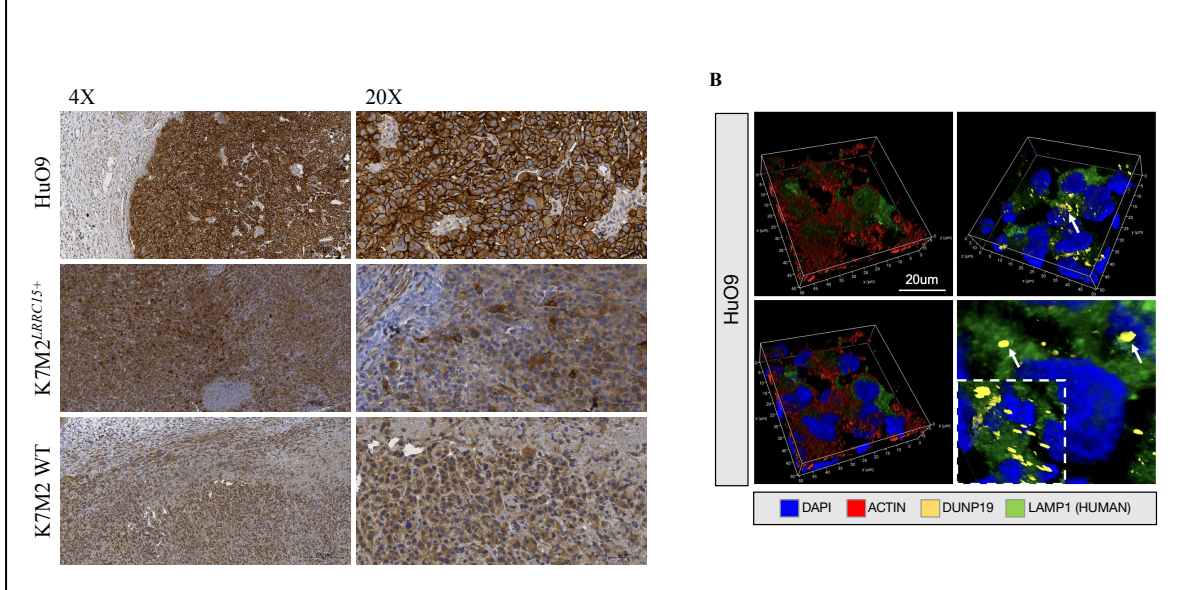
Supplemental Figure 2. Live confocal microscopy-based assays to determine internalization kinetics of DUNP19 after chelator conjugation and in various cell types. **A.** AF647-DUNP19 or AF647-DUNP19-DOTA conjugate internalize into U118MG cells at similar rates. To determine internalization rate, images were taken every hour across 12 h at 37C. Time to 50% internalization ($T_{1/2}$) of AF647-DUNP19 (measured by ratio of cytosolic intensity of AF647-DUNP19 compared to membrane integrated intensity) was 5.16 ± 0.83 h. The AF647-DUNP19-DOTA conjugate internalized at a similar rate, with a $T_{1/2}$ of 5.75 ± 0.93 h. **B.** Internalization of AF647-DUNP19 in fibroblast-derived Hs819.T cells compared to osteosarcoma SAOS2 cancer cells. To determine Internalization rate was determined by an 8 h microscopy-based assay with images were taken every 10m at 37C. Time to 50% internalization ($T_{1/2}$) of AF647-DUNP19 in SAOS2 cells was 1.31 ± 0.14 h. $T_{1/2}$ internalization of AF647-DUNP19 into Hs819.T cells was significantly slower with a $T_{1/2}$ of 1.66 ± 0.09 h.

Supplemental Figure S3



Supplemental Figure 3. Expanded tumor biodistribution of [¹⁷⁷Lu]-DUNP19 in U118MG, SAOS2, HuO9, K7M2^{LRRC15+} and HCC1954 xenograft models across 6 timepoints; 6h, 24h, 48h, 72h, 168h, and 336h. Tumor accumulation of [¹⁷⁷Lu]-DUNP19 peaks between 48-72 h for all models and is represented as %IA/g (percent injected activity per gram tissue). At 72h, tumoral accumulation is as follows; U118MG: 14.31 ± 2.01 %IA/g, SAOS2: 23.07 ± 2.90 %IA/g, HuO9: 43.93 ± 7.89 %IA/g, K7M2^{LRRC15+}: 13.60 ± 1.49 %IA/g, HCC1954: 11.83 ± 2.50 %IA/g.

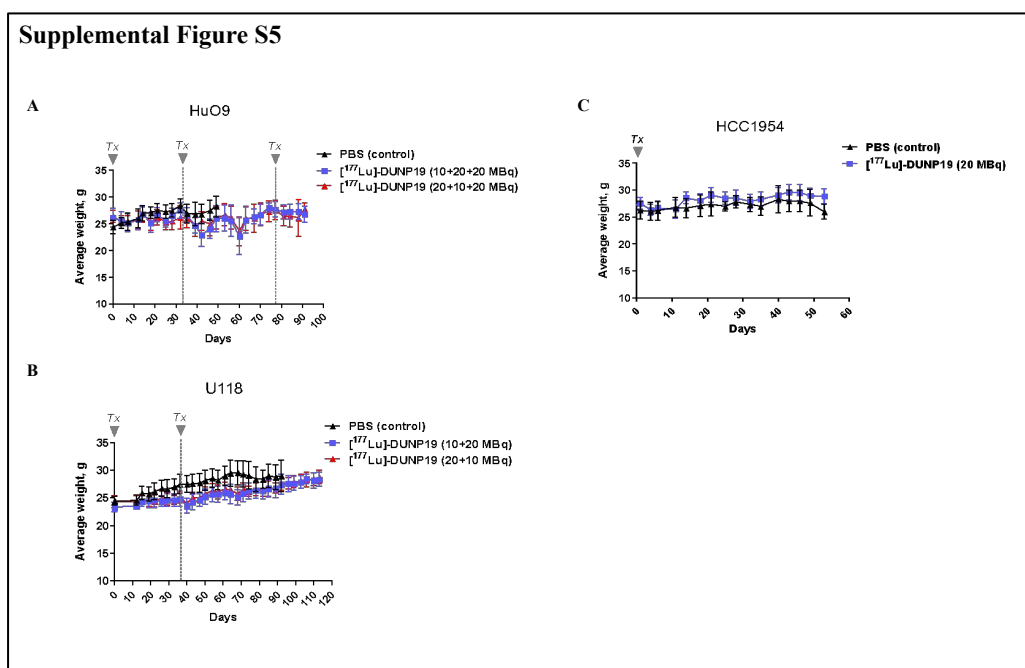
Supplemental Figure S4



Supplemental Figure 4. IHC and IF analysis of *ex vivo* LRRC15+ tumor models. **A.** *Ex vivo* immunohistochemistry analysis of HuO9, K7M2^{LRRC15+}, and K7M2 wildtype tumor sections

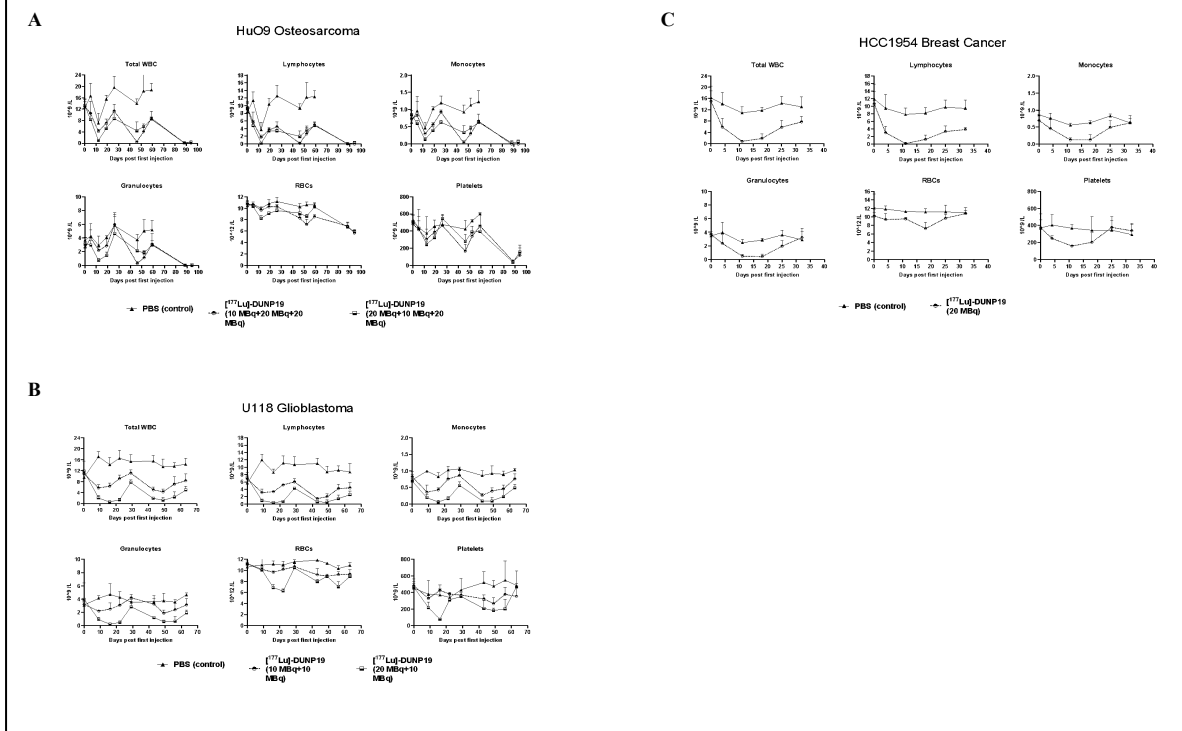
harvested from untreated animals. Images are stained for LRRC15 and counterstained with hematoxylin, shown at 4x and 20x.

B. Confocal microscopy of tumor tissues obtained from animals treated with fluorescently labeled DUNP19. Confocal images of s.c. HuO9 (LRRC15+ cancer cells / LRRC15+ CAF) tumors harvested at 72 h post- i.v. injection of AF594-DUNP19 (yellow). Tumor sections were co-stained for Actin (red), DNA (DAPI, blue) and LAMP1 (lysosomal marker, green). Images show that DUNP19 accumulates in the cellular cytoplasm and co-localized with LAMP1 indicating intracellular trafficking of the mAb to the lysosomal compartments (arrow) after binding to LRRC15.



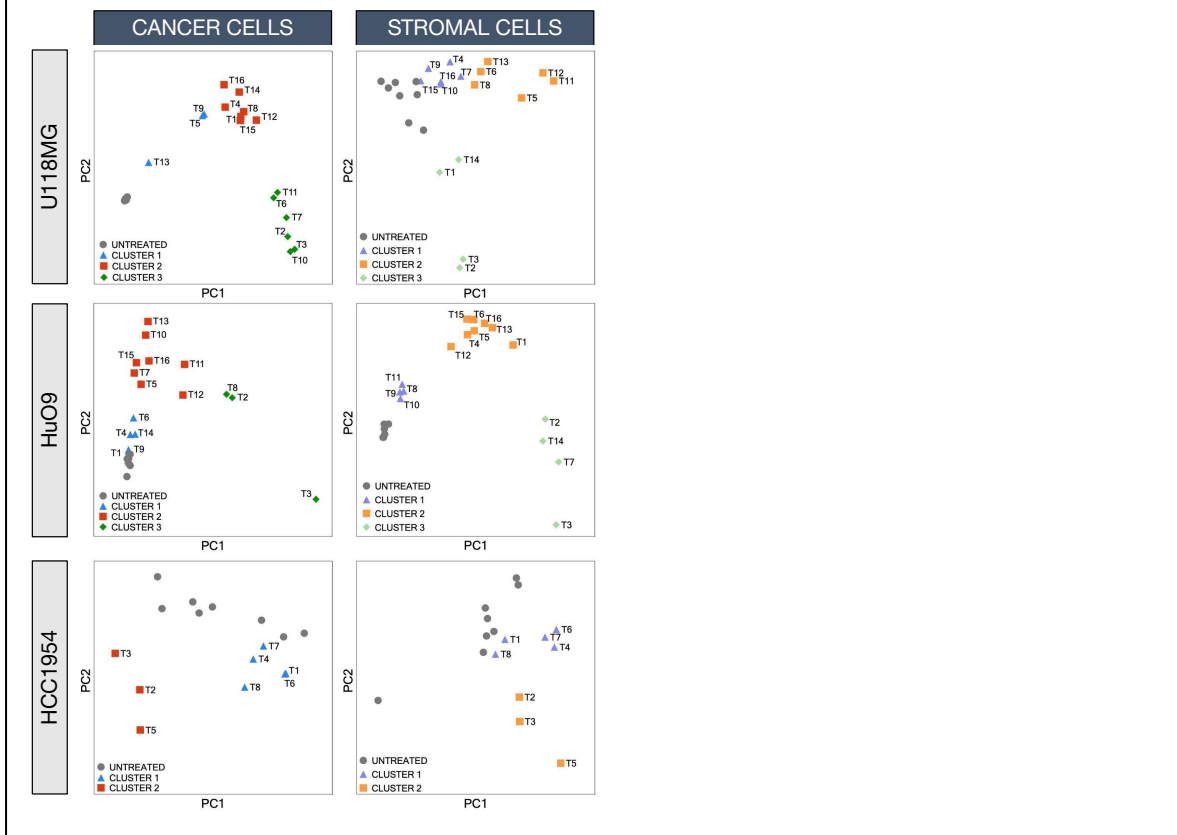
Supplemental Figure 5. Animal weights across tumor models (HuO9, U118MG, HCC1954) corresponding to therapy studies in Figure 3 (HuO9, top), and Figure 4 (U118MG, middle, and HCC1954, bottom). Gray arrows denote administration of [^{177}Lu]-DUNP19 or PBS. Overall, weight was stable throughout [^{177}Lu]-DUNP19 therapy studies across tumor models.

Supplemental Figure S6



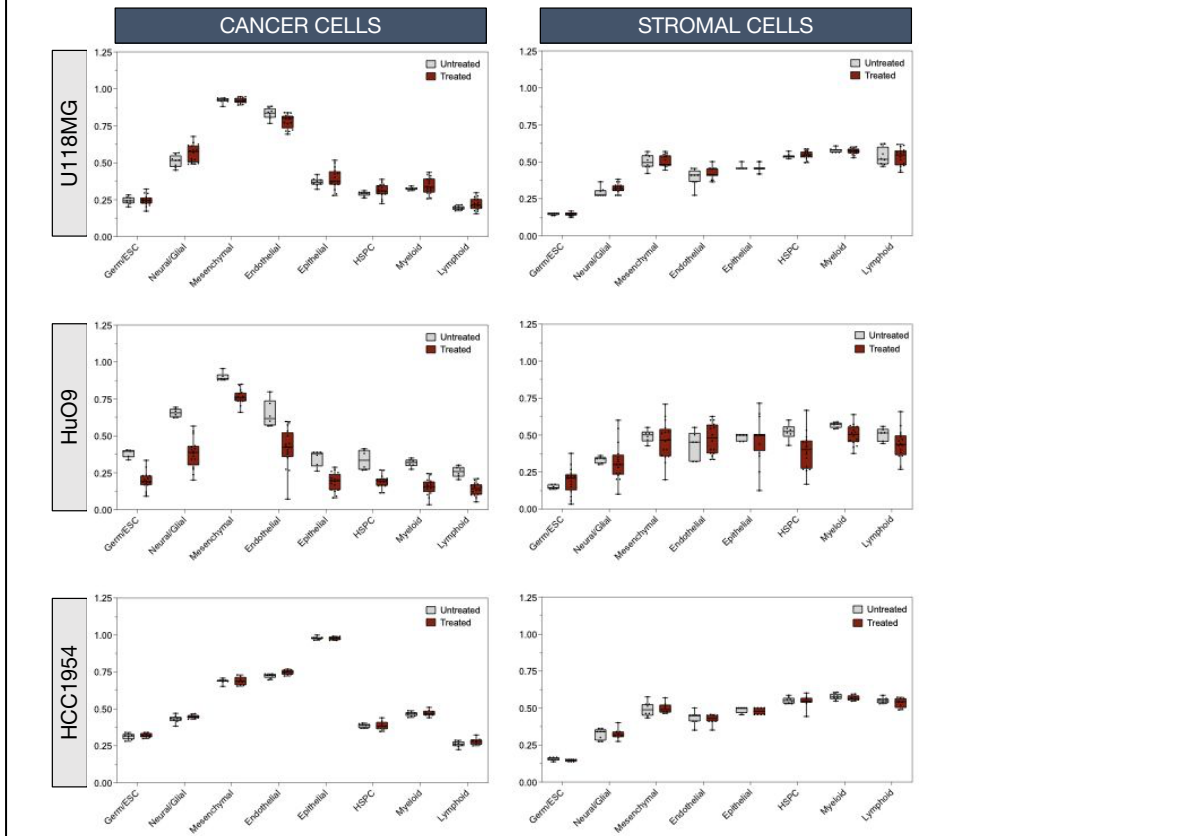
Supplemental Figure 6. Toxicity studies examining blood cell counts during treatment course across tumor models (HuO9, U118MG, HCC1954). HuO9 (top), U118MG (middle) and HCC1954 (bottom) exhibited transient reductions in lymphocytes and monocytes after administration of $[^{177}\text{Lu}]\text{-DUNP19}$, which recovered to baseline levels within 3 weeks, recapitulating toxicity profiles observed in clinical cases.

Supplemental Figure S7



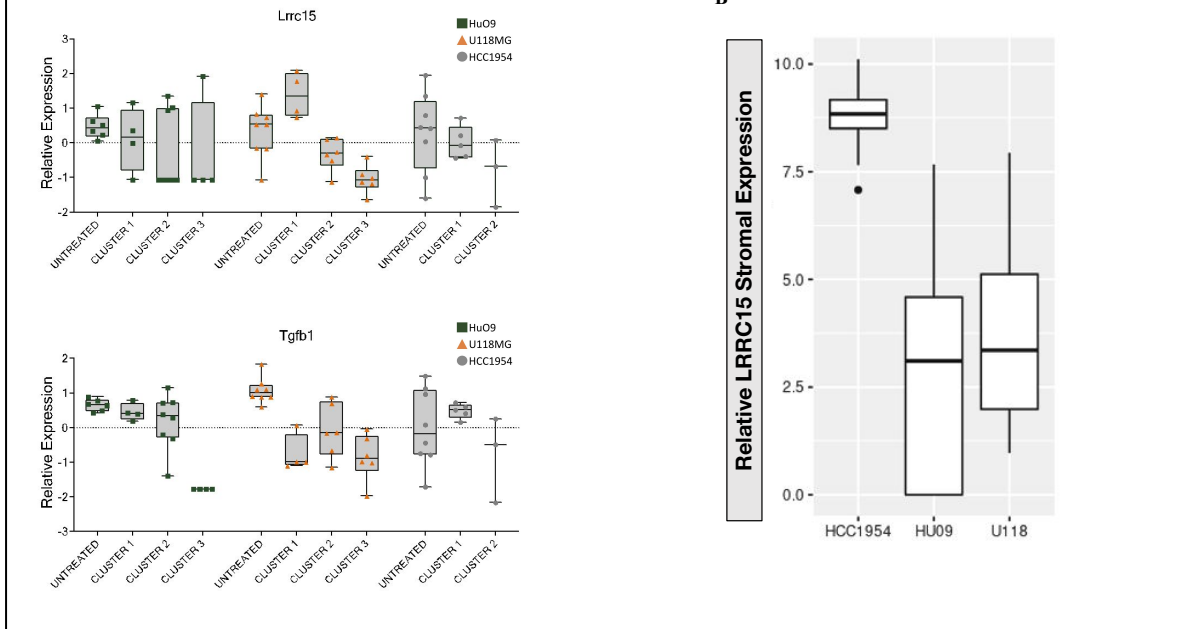
Supplemental Figure 7. Principal component analysis (PCA) plots of whole transcriptome cancer cell reads (left) and stromal cell reads (right). PC1 and PC2 show separation of treated samples in distinct clusters that were determined to correlate with LRRC15 transcript responses to [¹⁷⁷Lu]-DUNP19 RIT. In HuO9 and HCC1954 tumor models, treated cancer cells and stromal cells from the same sample clustered in similar patterns. U118MG and HuO9 treated tumors were grouped into three distinct clusters, whereas HCC1954 treated tumors formed two clusters that were differentiated from untreated mice.

Supplemental Figure S8



Supplemental Figure 8. Relative cell characterization of individual tumor samples using Syllogist. Overall, 43 cell types were analyzed and relative expression was averaged into seven summary cell types as shown (Germ/ESC, Neural/Glial, Mesenchymal, Endothelial, Epithelial, HSPC, Myeloid, Lymphoid). Normalized relative expression of cell types is presented on a scale of 0 (underrepresented cell type, not present in sample) to 1 (overrepresented cell type, present in sample). U118MG and HuO9 cancer cells were characterized as mesenchymal phenotypes, whereas HCC1954 cancer cells were majority epithelial (left plots), in line with relative LRR15 cancer cell expression between the three models. In stromal cells, no significant cell phenotype was observed in any of the three models (right plots).

Supplemental Figure S9



Supplemental Figure 9. Stromal cell expression of *Lrrc15* and *Tgfb1*. **A.** Transcript data from clustered (Supp. Fig.7) tumor stroma of *Lrrc15* (top) and *Tgfb1* (bottom) relative expression, represented by box-and-whisker plots. HuO9 transcripts are plotted in green (left), U118MG in orange (middle), and HCC1954 in grey (right). In HuO9 and U118MG stromal cells, expression of *Tgfb1* is significantly reduced in cluster 3 ($p < 0.05$). Across tumor models, changes in *Lrrc15* transcript expression were not significant between treated and untreated samples. **B.** Comparison of relative baseline transcript expression of *Lrrc15* in tumor stroma, comparing HCC1954 (right), HuO9 (middle) and U118MG (left). In HCC1954 tumors, median stromal *Lrrc15* expression is high (8.91) compared to moderate expression in HuO9 (3.02) and U118MG (3.48).

	6 h	24 h	48 h	72 h	168 h	336 h
Blood	18.84±1.12	11.86±1.67	9.31±0.66	8.74±1.08	5.07±1.02	2.58±0.63
Salivary gland	2.3±0.34	3.37±0.67	2.82±0.86	3.06±0.54	1.92±0.2	1.07±0.21
Heart	5.8±0.77	3.88±0.68	3.16±0.75	2.84±0.45	1.44±0.27	0.65±0.19
Lung	7.29±0.64	5.48±1.15	4.18±0.84	4.32±0.86	2.98±0.65	1.54±0.39
Liver	7.55±3.35	4.95±1.15	3.62±0.52	3.42±0.65	3.09±0.88	1.56±0.32
Spleen	4.99±1.05	4.41±0.68	4.54±1.19	3.76±0.7	2.79±0.77	2.02±0.28
Stomach	1.68±0.23	1.09±0.67	1.12±0.31	0.93±0.06	0.55±0.39	0.4±0.1
Small Intestine	2.2±0.38	1.58±0.32	1.42±0.51	1.31±0.25	0.74±0.25	0.37±0.12
Colon	1.94±0.54	1.13±0.2	0.75±0.14	0.91±0.2	0.5±0.08	0.27±0.09
Kidney	6.43±0.6	4.34±0.29	3.65±0.53	3.29±0.12	2.13±0.42	1.04±0.21
Tumor	3.86±0.86	18.09±1.41	17.87±3.04	23.1±2.9	20.55±6.19	15.64±4.1
Skin	3.07±1.06	6.07±1.1	6.2±0.73	7.64±1.23	4.65±1.63	2.5±0.48
Muscle	0.77±0.13	1.02±0.26	0.86±0.07	0.78±0.13	0.56±0.15	0.28±0.06
Bone	1.71±0.2	1.62±0.17	1.62±0.36	1.6±0.26	1.32±0.19	0.96±0.26
Brain	0.61±0.18	0.52±0.21	0.25±0.09	0.33±0.08	0.23±0.15	0.11±0.04

Table 1. Biodistribution of [¹⁷⁷Lu]-DUNP19 in male BALB/c-nu/nu mice bearing SAOS2 osteosarcoma xenografts 6-336 h after intravenous injection. The measured radioactivity of different organs is expressed as %ID/g and presented as an average value from 4 animals ± SD.

	6 h	24 h	48 h	72 h	168 h	336 h
Blood	23.81±3.1	14.69±2.7	13.68±1.1	11.56±1.1	4.49±1.4	1.74±0.52
Heart	6.6±1.3	4.31±1.14	4.36±0.97	3.9±0.34	1.51±0.45	0.67±0.19
Lung	10.58±0.9	7.69±1.21	6.6±0.67	5.89±0.67	2.62±0.41	1.43±0.33
Liver	9.83±2.58	6.52±0.81	6.15±0.17	5.78±0.58	2.95±0.12	2.62±0.96
Spleen	7.9±1.37	10.35±1.7	9.69±1.24	8.18±1.68	4.09±2.35	3.36±1.59
Stomach	2.34±0.31	1.75±0.41	1.53±0.25	1.43±0.1	0.7±0.33	0.31±0.15
Small Intestine	2.84±1.12	2.02±0.35	1.86±0.05	1.9±0.34	0.82±0.54	0.4±0.13
Colon	2.77±0.49	1.9±0.39	2.66±2	1.75±0.38	0.59±0.18	0.28±0.08
Kidney	9.25±1.25	6.68±1.32	4.65±2.21	5.35±0.84	2.48±0.27	0.9±0.13
Tumor	9.46±3.52	24.75±4.7	34.1±11.7	43.93±7.9	23.9±12.6	31.53±7.6
Skin	4.92±1.52	9.09±2.03	10.25±1.3	7.47±1.56	7.43±1.38	2.62±0.82
Muscle	1.39±0.13	1.52±0.35	1.39±0.28	1.26±0.2	0.83±0.2	0.45±0.1
Bone	2.35±0.38	2.57±0.39	2.36±0.09	2.63±0.7	1.38±0.51	0.91±0.23
Brain	0.78±0.34	0.4±0.09	0.44±0.11	0.29±0.09	0.13±0.03	0.06±0.02

Table 2. Biodistribution of [¹⁷⁷Lu]-DUNP19 in male BALB/c-nu/nu mice bearing HuO9 osteosarcoma xenografts 6-336 h after intravenous injection. The measured radioactivity of different organs is expressed as %ID/g and presented as an average value from 4 animals ± SD.

	24 h	48 h	72 h
Blood	9.63±0.77	7.57±1.39	5.75±0.73
Salivary gland	1.74±0.35	1.92±0.14	1.89±0.21
Heart	2.40±0.50	2.10±0.55	1.74±0.14
Lung	4.60±0.77	4.21±0.88	3.34±0.64
Liver	6.22±3.00	4.79±0.74	6.17±1.19
Spleen	4.61±1.83	4.79±1.22	4.03±1.13
Stomach	0.71±0.27	0.56±0.29	0.71±0.15
Kidney	3.82±0.54	2.92±0.37	2.40±0.24
Tumor	12.04±0.92	14.31±2.01	13.30±1.08
Muscle	0.65±0.27	1.14±0.25	0.96±0.32
Bone	0.44±0.30	1.35±0.63	0.97±0.23
Brain	0.12±0.06	0.18±0.03	0.28±0.07
GI tract*	2.63±0.34	2.24±0.26	2.33±0.31

Table 3. Biodistribution of [¹⁷⁷Lu]-DUNP19 in male BALB/c-nu/nu mice bearing U118MG glioblastoma xenografts 24, 48 and 72 h after intravenous injection. The measured radioactivity of different organs is expressed as %ID/g and presented as an average value from 4 animals ± SD. *GI tract uptake is presented as %ID only.

K7M2 ^{LRRCl5+}			HCC1954	
	48 h	72 h		72 h
Blood	7.62±0.76	6.98±1.13	Blood	6.95±1.67
Lung	3.80±0.37	4.55±1.19	Lung	4.01±1.03
Liver	4.67±1.21	4.88±1.22	Liver	4.37±0.72
Spleen	3.15±0.84	3.04±0.82	Spleen	3.97±0.49
Stomach	0.81±0.11	0.91±0.27	Stomach	0.81±0.08
Small Intestine	0.99±0.04	1.05±0.18	Small Intestine	N/A
Colon	0.72±0.14	0.98±0.24	Colon	N/A
Kidney	2.90±0.30	2.76±0.32	Kidney	2.77±0.35
Tumor	10.46±0.69	13.60±1.49	Tumor	11.83±2.5
Skin	4.88±0.52	6.43±1.45	Skin	6.04±1.06
Muscle	0.83±0.12	1.12±0.59	Muscle	0.95±0.36
Bone	1.21±0.28	1.17±0.40	Bone	1.16±0.12
Brain	N/A	0.26±0.07	Brain	2.29±0.31

Table 4. Biodistribution of [¹⁷⁷Lu]-DUNP19 in male BALB/c-nu/nu mice bearing murine K7M2^{LRRCl5+} osteosarcoma and human HCC1954 breast cancer xenografts after intravenous injection. The measured radioactivity of different organs is expressed as %ID/g and presented as an average value from 4 animals ± SD. *GI tract uptake is presented as %ID only.

Table S1. Gene set enrichment analysis of HuO9, U118MG, and HCC1954 cancer cells

	Pathway	Pval	Padj	Enrich Score	Norm Enrich Score
HuO9	HALLMARK_E2F_TARGETS	0.000	0.001	-0.380	-1.752
	HALLMARK_CHOLESTEROL_HOMEOSTASIS	0.001	0.015	-0.453	-1.700
	HALLMARK_FATTY_ACID_METABOLISM	0.002	0.015	-0.392	-1.643
	HALLMARK_OXIDATIVE_PHOSPHORYLATION	0.001	0.015	-0.351	-1.595
	HALLMARK_GLYCOLYSIS	0.001	0.015	-0.362	-1.584
U118MG	HALLMARK_MYC_TARGETS_V2	0.000	0.000	-0.583	-2.406
	HALLMARK_MYOGENESIS	0.000	0.000	0.664	1.745
	HALLMARK_TNFA_SIGNALING_VIA_NFKB	0.000	0.000	0.623	1.637
	HALLMARK_KRAS_SIGNALING_DN	0.000	0.000	0.666	1.698
	HALLMARK_KRAS_SIGNALING_UP	0.000	0.000	0.613	1.607
HCC1954	HALLMARK_INTERFERON_GAMMA_RESPONSE	0.000	0.000	-0.620	-2.186
	HALLMARK_INTERFERON_ALPHA_RESPONSE	0.000	0.000	-0.695	-2.286
	HALLMARK_OXIDATIVE_PHOSPHORYLATION	0.000	0.000	0.446	2.063
	HALLMARK_GLYCOLYSIS	0.000	0.000	0.425	1.945
	HALLMARK_INFLAMMATORY_RESPONSE	0.000	0.000	-0.554	-1.903

Table S2. Gene set enrichment analysis of HuO9, U118MG, and HCC1954 stromal cells

	Pathway	Pval	Padj	Enrich Score	Norm Enrich Score
HuO9	HALLMARK_G2M_CHECKPOINT	0.000	0.000	-0.546	-2.295
	HALLMARK_E2F_TARGETS	0.000	0.000	-0.524	-2.174
	HALLMARK_INTERFERON_ALPHA_RESPONSE	0.000	0.000	-0.510	-1.928
	HALLMARK_MYOGENESIS	0.000	0.000	-0.428	-1.782
	HALLMARK_MYC_TARGETS_V1	0.000	0.001	-0.404	-1.724
U118MG	HALLMARK_E2F_TARGETS	0.000	0.000	-0.725	-3.288
	HALLMARK_G2M_CHECKPOINT	0.000	0.000	-0.692	-3.154
	HALLMARK_ALLOGRAFT_REJECTION	0.000	0.000	-0.694	-3.046
	HALLMARK_INTERFERON_GAMMA_RESPONSE	0.000	0.000	-0.671	-2.987
	HALLMARK_ADIPOGENESIS	0.000	0.000	0.688	2.371
HCC1954	HALLMARK_MYOGENESIS	0.000	0.000	-0.688	-2.479
	HALLMARK_G2M_CHECKPOINT	0.000	0.000	-0.669	-2.424
	HALLMARK_E2F_TARGETS	0.000	0.000	-0.640	-2.317
	HALLMARK_ALLOGRAFT_REJECTION	0.000	0.000	-0.614	-2.182
	HALLMARK_COAGULATION	0.000	0.000	0.559	1.953

CHAPTER 4. KEY REGULATORY ELEMENTS OF THE TGF β -LRRC15 AXIS PREDICT DISEASE PROGRESSION AND IMMUNOTHERAPY RESISTANCE ACROSS CANCER TYPES

Transforming growth factor-beta (TGF β) has dual roles in cancer, initially suppressing tumors but later promoting metastasis and immune evasion. Efforts to inhibit TGF β have been largely unsuccessful due to significant toxicity and indiscriminate immunosuppression. Leucine-rich repeat-containing protein 15 (LRRC15) is a TGF β -regulated antigen expressed by mesenchymal-derived cancer cells and cancer-associated fibroblasts (CAFs). In preclinical studies, ablation of TGF β -driven LRRC15⁺ CAFs increased tumor infiltration of CD8⁺ T cells. However, the underlying pathobiological mechanisms prompting TGF β 's upregulation of LRRC15 expression are unclear. Using an integrated approach combining functional compound screening with single-cell RNA sequencing, we reveal key genomic features regulating TGF β 's ability to increase LRRC15 expression on cancer cells. Construction of gene regulatory networks converged our analyses on four key genes—MMP2, SPARC, TGF β R2, and WNT5B—central to TGF β -induced LRRC15 pathobiology. Validation of these genes in cell models and their use in predicting immunotherapy responses highlight their potential in refining immunotherapy strategies and personalizing co-treatment options.

Adapted from: “Key Regulatory Elements of the TGF β -LRRC15 Axis Predict Disease Progression and Immunotherapy Resistance Across Cancer Types”

Claire M. Storey, Michael Cheng, Mohamed Altai, Julie E. Park, Julie Tran, Smiths S. Lueong, Daniel Thorek, Liqun Mao, Wahed Zedan, Constance Yuen, Alexander Ridley, Marija Trajovic-

Arsic, Ken Herrmann, Sumit K. Subuhdi, Bilal A. Siddiqui, Katharina Lückerath, Jens Siveke, Robert Damoiseaux, Xia Yang, David Ulmert

CMS, MC: writing (original draft), writing (review and editing), data collection, formal analysis

MA: writing (original draft), writing (review and editing)

JEP, LM: data collection, formal analysis

JT, SSL, MTA: formal analysis

WZ, CY, AR: data collection

KH, KL, JTS: writing (review and editing)

SS, BS: formal analysis, writing (review and editing)

XY, DU: writing (original draft), writing (review and editing), conceptualization

4.1. INTRODUCTION

The transforming growth factor-beta (TGF β) signaling pathway, recognized for its dual role in cancer biology, acts as a tumor suppressor in early-stage malignancies but promotes progression, metastasis, and immune evasion in aggressive cancers and advanced stages of disease [1-3]. This paradoxical behavior complicates targeting of TGF β in oncology, as its functions vary widely from tumor suppression to the facilitation of epithelial-mesenchymal transition (EMT) and therapy resistance [4-6]. TGF β also plays a role in both primary and acquired resistance to treatment; signaling initially contributes to an immunosuppressive microenvironment that shields emerging tumors from immune surveillance. During acquired resistance, TGF β signaling intensifies, enabling cancer cells to evade ongoing therapies by promoting invasiveness, metastasis, and maintaining an immunosuppressive microenvironment [7-9].

Leucine-rich repeat-containing protein 15 (LRRC15) has been recognized for its role as surrogate marker for TGF β signaling and its association with immunosuppression and therapy resistance in aggressive TGF β -mediated malignancies, notably in treatment-resistant osteosarcoma [10]. Its predominant association with cancer-associated fibroblasts (CAFs) in the tumor microenvironment (TME) of immune-excluded, metastatic, and aggressive primary tumors further underscores its therapeutic relevance [11]. Investigations into the TGF β -driven TME have identified that LRRC15 is a part of an 11-gene signature that correlates to immune checkpoint therapy (ICT) resistance in patients [12-14]. Furthermore, recent data from engineered mouse models demonstrated that targeted depletion of LRRC15+ CAFs markedly diminishes tumor fibroblast content and augments CD8+ T cell efficacy [13]. Our previous independent verification using a novel radiotheranostic antibody-based approach confirmed that radioimmunotherapeutic targeting of LRRC15+ cells significantly decreased tumor burden and stopped disease progression, along with suppression of genes linked to TGF β -driven immunotherapy resistance [15].

In this study, we evaluated the complex interplay of TGF β signaling and LRRC15 expression within mesenchymal stem cell (MSC)-derived tumors. We show a bifurcated cellular response to TGF β activity; certain tumor cells undergo a rapid induction of LRRC15, while expression is unaltered in others. To further explore the transcriptional dynamics observed in TGF β -responsive LRRC15+ cell models, we comprehensively investigated how this differential expression of LRRC15 is indicative of TGF β -mediated tumor pathobiology. Integration of high-throughput screening (HTS) to identify small molecules that modulate TGF β -mediated LRRC15 induction, along with single-cell RNA sequencing (scRNAseq) to identify the gene networks

and key regulators of LRRC15 inducibility, identified four genes—*TGFβR2*, *SPARC*, *MMP2*, and *WNT5B*—that activate TGFβ-mediated LRRC15 expression. Further evaluation in patient tumor cohorts revealed that these activating genes, alongside LRRC15, are a prognostic determinant for patient response to immunotherapy and the progression of aggressive malignancies.

4.2. MATERIALS AND METHODS

Cell Lines

CALU1 (non-small-cell lung cancer), KASUMI-2 (leukemia), NCI-H196 (small cell lung cancer), RPMI7951 (melanoma), SAOS2 (osteosarcoma), U118-MG (glioblastoma), U2OS (osteosarcoma) and U87-MG (glioblastoma), were purchased from ATCC. HUO9 (osteosarcoma) was purchased from the Japanese Collection of Research BioSources (Tokyo, Japan). All cell lines were cultured according to the manufacturer's instructions (base media with 10% FBS) and frequently tested for Mycoplasma by PCR.

Flow Cytometry

Cells were serum-starved in appropriate base media + 0.3% FBS for 16 hours, followed by treatment with recombinant human TGFβ1 (0.001ng/mL-10ng/mL, Peprotech, #100-21C) for 24 hours. The LRRC15-binding antibody DUNP19 (<https://doi.org/10.1101/2024.01.30.577289>) was conjugated to Alexa Fluor 647 with an amine-reactive antibody labeling kit (ThermoFisher, #A20186) following manufacturer protocols for labeling. Cells were stained for LRRC15 expression with 100ng/mL DUNP19-AF647 for 45 minutes at room temperature and analyzed using the Attune NxT Flow Cytometer (Invitrogen)

in collaboration with UCLA's Jonsson Comprehensive Cancer Center Flow Cytometry Shared Resource. Data was analyzed using FlowJo (Version 10, BD Biosciences).

Confocal Microscopy

Cells (0.002×10^6 cells/well) were seeded in appropriate base media + 0.3% FBS for 16 hours in 384-well u-clear flat bottom black plates (Greiner, #781092) before treatment with recombinant human TGF β 1 (0.001ng/mL-10ng/mL) for 24 h. Cells were fixed with 3.7% PFA in PBS for 15 minutes at room temperature, washed, and stained with 100ng/mL DUNP19-AF647 and Hoechst 33342 at a 1:2000 dilution (Invitrogen, #H1399) for 2 hours at room temperature in the dark. Cells were washed with PBS and imaged using a ImageXpress Micro Confocal High-Content Imaging microscope (Molecular Devices). For each well, images were taken at 10x objective with 4 sites imaged per well. For TGF β inhibition, 0-100uM Galunisertib (MedChemExpress, #HY-13226) was added 16 h prior to addition of 0-10 ng/mL TGF β 1. After 24 h, cells were fixed and stained for LRRC15 as described above.

Small Molecule Screening

The LOPAC¹²⁸⁰ compound library (Sigma Aldrich) was used to identify inhibitors that could block TGF β 's induction of LRRC15 protein expression. Compounds were dissolved at 1 mM in DMSO, and 250 nL of each was transferred into 384-well u-clear flat-bottom black plates, resulting in a final concentration of 5 μ M. The liquid transfer was performed using a Biomek automated liquid handler (Beckman Coulter).

TGF β -responsive cells (0.04×10^6 cells/mL; HUO9, RPMI7951, or U118-MG) were resuspended in media containing 0.3% FBS, transferred to the prepared plates (50 μ L/well, 2000 cells), and incubated for 16 h. After incubation, plates were treated with a final concentration of 4 ng/mL TGF β 1 diluted in serum-starved media; this TGF β 1 concentration was chosen because it resulted in maximal LRRC15 induction in flow cytometry and confocal microscopy assays across cell lines. Columns 1-2 of the 384-well plates were treated with TGF β 1 without any compounds, serving as positive controls for LRRC15 induction. In contrast, columns 23-24 were left untreated to establish baseline LRRC15 expression.

After 24 h, cells were fixed with 3.7% PFA in PBS for 15 minutes at room temperature, washed with PBS, and stained with 100 ng/mL DUNP19-AF647 and Hoechst 33342 at a 1:2000 dilution (Invitrogen, #H1399) for 2 h at room temperature in the dark. After staining, cells were washed with PBS before imaging with a ImageXpress Micro Confocal High-Content Imaging microscope (Molecular Devices). For each well, images were taken at 10x objective with 4 sites imaged per well.

Image Analysis of Confocal Microscopy

Images from the plates were processed using a custom image analysis module in MetaXpress. Nuclei were first identified based on Hoechst 33342 staining, and nuclei count, integrated Hoechst 33342 intensity, and nucleus size were recorded. LRRC15+ cells were defined by staining intensity at or exceeding a threshold of 2000 above background. The number of LRRC15+ cells was normalized to total nuclei count, and the average %LRRC15+ cells per well was calculated by averaging values across all imaged sites within each well.

A standardized Z-score was calculated by subtracting the mean %LRRC15+ value of all wells within the plate and dividing by the standard deviation in %LRRC15+ scoring. Z-scores were similarly calculated for nuclei counts to identify toxic compounds, excluding control wells from all calculations. Hit compounds were defined as any non-toxic compounds (nuclei count Z-score > -1) that reduced LRRC15 staining to a Z-score of < -3.

Silencer RNA

Silencer RNAs targeting selected genes were obtained from ThermoFisher Scientific (catalog #4392420). For a complete description of siRNA transfection, see supplementary methods. 72 h after siRNA transfection, cells were treated with 0-8 ng/mL TGF β 1 for 24 h, followed by fixation and LRRC15 staining as described above. Successful transfection was confirmed by loss of LRRC15 expression in all three siLRRC15 conditions. Plates were imaged using a ImageXpress Micro Confocal High-Content microscope, and images were analyzed with a custom module in MetaXpress (see supplementary methods). Total LRRC15 expression for each siRNA condition was quantified by measuring the average integrated intensity of LRRC15 staining in each well, normalized to the staining intensity in non-transfected, TGF β 1-treated and untreated controls.

scRNAseq Analysis

scRNAseq datasets from all cell lines (6 cell lines, 2 replicate per cell line) were analyzed together using Seurat's library size normalization, log transformation, scaling, principal component analysis (PCA), K-nearest neighbor detection, and UMAP visualizations [44-45]. Standard quality control (QC) procedures were applied to filter out poor quality cells, keeping

only cells with mitochondrial gene percentage below 5% and gene count between 200 and 5000. We kept genes that were expressed in at least 100 cells. QC plots are reported in Supplemental Figure 3. In total, 57,771 cells passing QC across all cell lines were kept for downstream analysis. With hdWGCNA's metacell approach [46] cells with similar expression were aggregated and averaged within each cell line to reduce gene expression sparsity for differential gene expression analysis and network modeling. To identify DEGs associated with TGF β inducibility while considering the sample size (2 replicates per cell line), a one sample-vs-opposite group DEG analysis was performed consisting of 6 separate Wilcoxon rank sum tests comparing each cell line (e.g., one cell line in the TGF β inducible group) to all cell lines in the opposite comparison group (e.g., all cell lines in the non-inducible group). Only DEGs that were consistent across all comparisons were considered for downstream analysis to avoid cell line-specific variation that could heavily skew the gene counts distribution and produce false positives. All significant DEGs passing false discovery rate (FDR) <5% and large-effect DEGs with an absolute value log fold change of at least 0.5 were used as two DEG sets for downstream analysis.

Pathway Analysis of DEGs using GSEA

Pathway enrichment of DEGs and SCING and hdWGCNA modules and was conducted using the EnrichR R package for Gene Ontology Biological Process and Reactome databases separately [47]. Benjamini Hochberg (BH) correction was performed to control the false discovery rate.

Network Analysis

SCING regulatory network inference [21] was employed on scRNAseq data from all cell lines to assess gene regulatory relationships and to identify subnetworks specific to TGF β inducibility. When given scRNAseq data, SCING trains gradient boosting machines to predict target gene expression based on their co-expressed genes and extracts feature importance measures of the feature genes to weight directed network edges. To add robustness, SCING pseudo-bulks cells through Leiden clustering [22] to mitigate gene sparsity and implements a bootstrapping strategy to generate and aggregate gene regulatory networks to produce a consensus GRN across subsamples of the data [21]. With the final GRN, Leiden clustering was used to identify highly connected subnetworks, or modules, and generated module expression profiles for each cell line using the module eigengene approach from hdWGCNA [19].

As a complementary network approach, hdWGCNA was run to establish a correlation-based co-expression network method for single cell data [19]. Modules from this network were obtained through the method's topological overlap matrix and corresponding expression using the module eigengene approach [19]. We performed module-trait association analysis to correlate TGF β inducibility with the modules. To identify modules associated with TGF β responsiveness, the one sample-vs-opposite group approach mentioned in the DEG analysis was performed on the module expression data for SCING and hdWGCNA modules separately. Pathway enrichment for SCING and hdWGCNA modules was conducted using the EnrichR R package for Gene Ontology Biological Process and Reactome databases separately [47]. BH correction was performed to control the false discovery rate.

In Silico Drug Repositioning Analysis Using scRNAseq DEGs and Network Modules

To identify drug candidates matching the TGF β inducible gene sets from scRNAseq (two DEG sets, one with all significant DEGs and the other with upregulated DEGs with log fold change >0.5; two differential network module sets from SCING and hdWGCNA), we applied a one-tailed Fisher's exact test between each of the four TGF β inducible gene sets and curated drug target gene signatures from the L1000 forward drug signature database [23].

The L1000 database consists of drug signatures from a variety of in vitro and in vivo studies in various cell lines and tissues, drug dosages, and response times. We subset the L1000 drug signatures to focus on human datasets. BH FDR correction was applied to the overlap analysis to derive significant overlaps at FDR<5% and drugs with fewer than 5 gene overlaps with the scRNAseq signatures were eliminated from the significant results. Significant drugs from our in-silico drug repositioning analysis were overlaps with those from our in-vitro high throughput screening to identify consistent drugs. The scRNAseq-based TGF β inducible gene sets targeted by these replicated drugs were used for candidate regulatory gene prioritization, where gene signatures were overlapped across the four TGF β inducible gene sets targeted by replicated drugs to identify consistent target genes with potential relationships to the TGF β -LRRC15 axis.

Key Driver Analysis to Identify Potential Regulators of TGF β -LRRC15 Axis

Potential regulators of the TGF β -LRRC15 axis were identified using Key Driver Analysis (KDA) on the SCING GRN [46]. KDA uses the GRN topology to identify hub genes with high connectivity to gene sets of interest. It identifies hub gene neighborhoods enriched for the gene sets through a chi-like statistic, and measures significance of the enrichment based on the null distribution of enrichment scores generated from permuted networks. The significant hub genes

are proposed as the key drivers of the gene sets of interest. We performed KDA on SCING GRN modules to detect key drivers within each module.

Network Visualization

Network visualization was performed on the SCING network using Cytoscape [48]. The network visualized in Figure 4C include the top drug target candidates from the in-silico drug screen and their direct paths to LRRC15 and TGFB. All neighbors of the drug targets are found in Supplemental Figure 2B. Because these networks focus on the drug targets, some key drivers' connections are not visualized and thus show little connectivity.

In silico analysis

Gene expression data from the different tumor entities were obtained from publicly available repositories for the following entities (breast cancer GSE25066), glioblastoma multiform (PRJNA482620) and skin cutaneous melanoma (phs00452) or in-house generated (pancreatic cancer). The expression data for all genes constituting the LRRC15 signature was extracted. A regression model with time-to-event outcome was performed and the regression coefficients were used to compute the LRRC15 signature as previously described [14]. Kaplan-Meier survival analysis was performed for the LRRC15 signature for all entities after an optimal-cutoff was determined using the Survminer package with R version 4.4.1 environment.

4.3. TGF β 1 induces LRRC15 expression in cancer cells

Previous studies have shown that TGF β 1 induced LRRC15 expression in MSCs under supraphysiological conditions over extended periods of time [16]. In this study, we investigated

the response of LRRC15 expression in cancer cells to physiologically relevant TGF β 1 concentrations, simulating conditions within the TME [17]. Nine LRRC15+ cancer cell lines (CALU1, KASUMI2, SAOS2, U2OS, HUUO9, NCI-H196, U118, U87, RPMI7951) [15] underwent 24-hour incubation in reduced-serum media prior to reintroduction of TGF β 1 at concentrations from 0 to 10 ng/mL (Figure 1A). Subsequently, plasma membrane-associated LRRC15 was detected via flow cytometry using the AlexaFluor-647 labeled anti-LRRC15 IgG1 antibody (DUNP19).

These assessments revealed variable responses to TGF β , with minimal changes in LRRC15 expression levels in CALU1 (percent change in LRRC15 staining = -21.94%, $p = 0.2805$), KASUMI2 (-8.16%, $p = <0.0005$), SAOS2 (+4.89%, $p = 0.0517$) and U2OS (+18.98%, $p = 0.0008$), while pronounced increases were noted in HUUO9 (+210.26%, $p = 0.0220$), NCI-H196 (+70.82%, $p = <0.0005$), U118 (+173.06%, $p = <0.0005$), U87 (+53.65%, $p = <0.0005$), and RPMI7951 (+76.45%, $p = 0.0038$), (Figure 1A). For subsequent analyses, the latter cell lines were deemed “TGF β -responsive” for their ability to upregulate LRRC15 after treatment with exogenous TGF β 1. Among the TGF β -responsive cell lines, we focused on three models representing aggressively growing malignant tissues from different anatomical origins: HUUO9 (osteosarcoma), RPMI7951 (malignant melanoma), and U118 (glioblastoma multiforme). Using a confocal microscopy-based approach with an AlexaFluor-647-conjugated DUNP19, we confirmed a significant increase in LRRC15 expression in cells treated with TGF β compared to controls as shown for the RPMI7951 cell line (Figure 1B). Furthermore, pretreatment with the TGF β receptor inhibitor galunisertib before addition of TGF β 1 effectively suppressed LRRC15

induction in HUO9, RPMI7951, and U118 cells, demonstrating the role of TGF β in modulating LRRC15 expression (Figure 1C).

Next, we sought to annotate the molecular mechanisms impacting TGF β 's regulation of LRRC15 (Figure 1D_{i-iii}). We conducted a high-throughput screen using the LOPAC1280 library, which comprises 1,280 well-annotated small molecules spanning various mechanisms of action and drug classes (Figure 1D_{ii-iii}). LRRC15⁺ cells were incubated in reduced-serum media to deplete endogenous cytokines before treatment with the compound library and TGF β (Figure 1D_i). Following compound incubation, cells were treated with TGF β and assessed for LRRC15 expression via confocal microscopy (Figure 1D_i). All screened compounds were categorized by class and mechanism, and the normalized results were presented as their average effect on LRRC15 expression (Figure 1E_i). Compounds that significantly inhibited TGF β -driven LRRC15 expression, defined as those reducing the integrated intensity of LRRC15 by more than three standard deviations (SD) from the plate mean, were identified as hits (Figure 1E_{ii}). In addition, compounds were assessed for toxicity; those reducing cell viability >3 SD from the mean were excluded from subsequent analyses. Ultimately, we identified 26, 22, and 24 hits in the HUO9, RPMI7951, and U118 cell lines, respectively (Supplemental Table 1).

Established TGF β R2 antagonists such as SB-525334 and RepSox further validated the specificity of the assay and the mechanism by which LRRC15 is upregulated (Supplemental Table 1). Notably, various histaminergics, antivirals, and hormone modulators, for example chloroquine, Tenidap, and hydrocortisone, also reduced TGF β -induced LRRC15 expression, underscoring the diverse roles of TGF β in inflammation and immune modulation via diverse

biological pathways (Figure 1E). Other compound classes, including potassium channel inhibitors and angiotensin inhibitors, increased LRRC15 expression above baseline (Figure 1E). These compound hits were particularly intriguing given LRRC15's previously reported role in SARS-CoV-2 infection and structural similarity to the angiotensin-converting enzyme ACE2 [18], suggesting some utility in preventing viral infection. All gene targets from the effective compounds within our screen were compiled for further analysis.

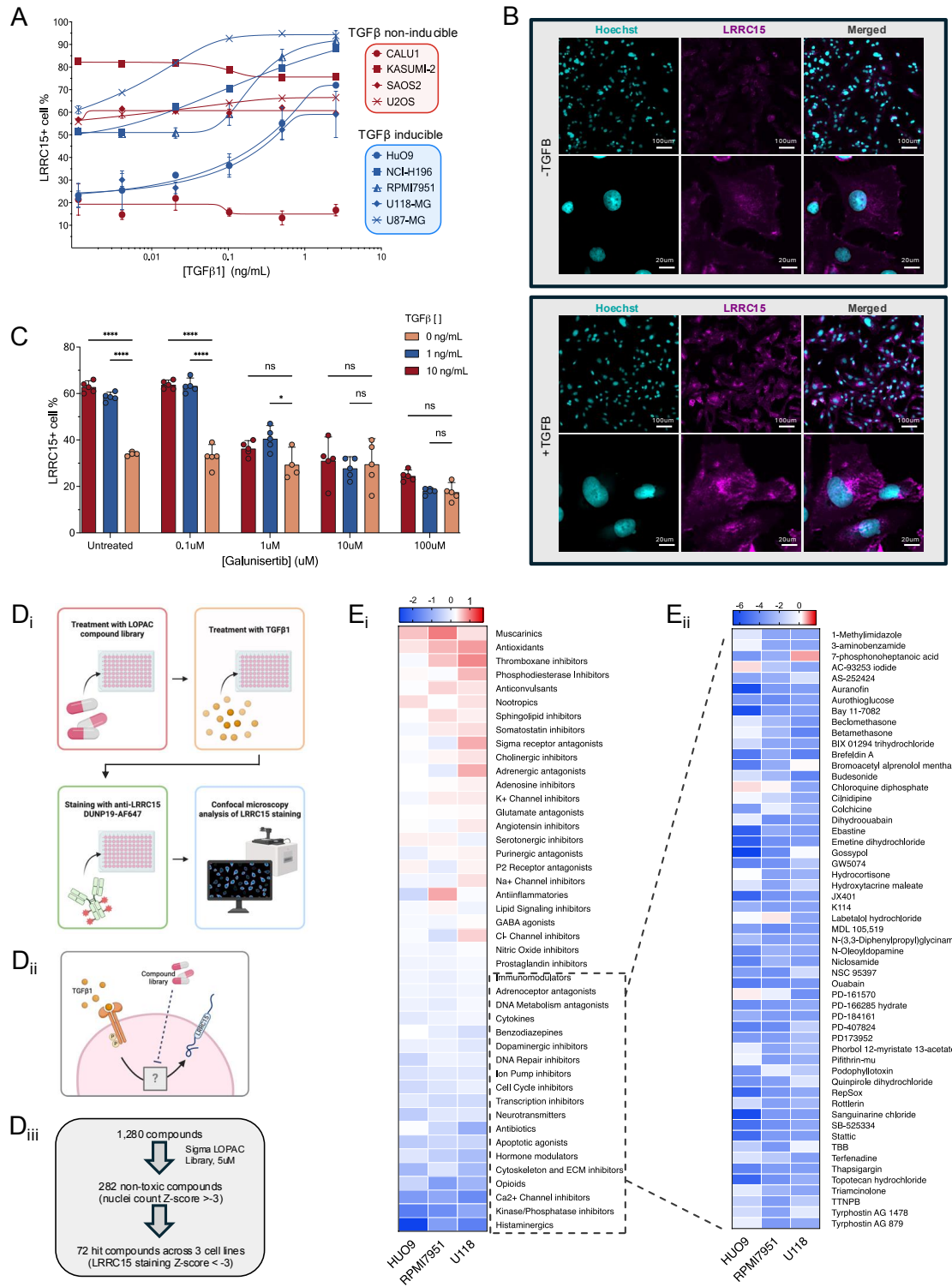


FIGURE 1. Dissection and modulation of the TGFβ-LRRRC15 axis in select cancer cell lines. (A) LRRRC15⁺ cancer cell lines were exposed to TGFβ1 concentrations from 0 to 10

ng/mL following 24 hours of cytokine starvation to simulate physiological conditions. Flow cytometry analysis shows variable LRRC15 expression responses across cell lines, with minimal changes observed in CALU1, KASUMI-2, SAOS2, and U2OS (TGF β non-inducible, red), and significant upregulation in HUO9, NCI-H196, RPMI7951, U118, and U87 (TGF β inducible, blue) ($P < 0.0001$). LRRC15 staining is represented as mean \pm SD. **(B)** Confocal microscopy of LRRC15 expression in TGF β -responsive cell line RPMI7951 after treatment with or without TGF β . Cells were stained with Hoechst (nuclei, cyan) and anti-LRRC15 IgG1-AlexaFluor-647 (magenta). **(C)** Pretreatment with the TGF β receptor inhibitor Galunisertib significantly suppressed TGF β -induced LRRC15 expression in a dose-dependent manner ($p < 0.0001$), confirming pathway specificity. Data is expressed as average LRRC15 expression across U118, RPMI7951, and HUO9 cells. **(D)** Schematic of high-throughput screening workflow. **(i)** LRRC15+ cells were pre-treated with the LOPAC1280 compound library, followed by TGF β 1 reintroduction and analysis of LRRC15 expression using confocal microscopy. **(ii)** Compounds were classified based on mechanism of action, and the effects on LRRC15 expression were recorded. **(iii)** 1,280 compounds were screened, and 282 non-toxic compounds were identified (cell count Z-score > -3). Of these, 72 compounds were hits, reducing LRRC15 expression below 3 standard deviations from the plate mean. **(E)** Heatmap (red = increase, blue = decrease) of LRRC15 staining Z-scores across compound classes (left heat map) and all hit compounds (right heat map) after screening with LOPAC1280 compound library.

4.4. Single-cell sequencing of TGF β -responsive cell lines reveals distinct LRRC15-related signatures

After identifying compounds that could disrupt the TGF β -LRRC15 pathway, we performed scRNAseq on the cell lines utilized in the compound screen. In addition to the screened cell lines, three TGF β non-responsive cell lines (CALU1, KASUMI2, SAOS2) were also sequenced and used in subsequent differential gene and pathway analyses (Figure 2A). To reduce gene expression sparsity, we used a high-dimensional weighted gene co-expression network analysis (hdWGCNA) metacell aggregation approach [19], which aggregates neighboring cells based on gene expression similarity and averages their expression to create metacells that are robust to scRNAseq dropouts Figure 2A. This enabled us to identify individual differentially expressed genes (DEGs) and transcriptomic pathways that were exclusive to TGF β -responsive cells. While the lower dimension representation of the gene expression data did not separate the six cell lines by TGF β inducibility (Figure 2B), we identified sets of DEGs with consistent effects in TGF β -responsive cells (Figure 2C). Key cell proliferation and non-canonical TGF β signaling genes, including TGF β activator *LTBPI* (latent-transforming growth factor beta-binding protein 1) and Wnt ligand *WNT5B*, were upregulated in TGF β -responsive cells. Interestingly, T-cell modulators and inflammatory driver genes such as *IL-7R* (interleukin-7 receptor) [20] were downregulated in TGF β -inducible cell lines, providing insights into the potential immunoregulatory mechanisms within the TGF β -LRRC15 pathway (Figure 2C). Gene set enrichment analysis of upregulated genes in the TGF β -responsive cells showed enrichment of apoptotic processes and cytokine signaling within immune pathways, while downregulated DEGs were associated with translation and ribosomal function (Figure 2D). Furthermore, the DEG effect, calculated using metacell expression, followed a similar pattern in single cell expression UMAP plots. Several genes such as *SPARC*, *WNT5B*, *MMP2*, and *EIDI*, showed a stark upregulation of expression within TGF β -responsive cells (Figure 2E).

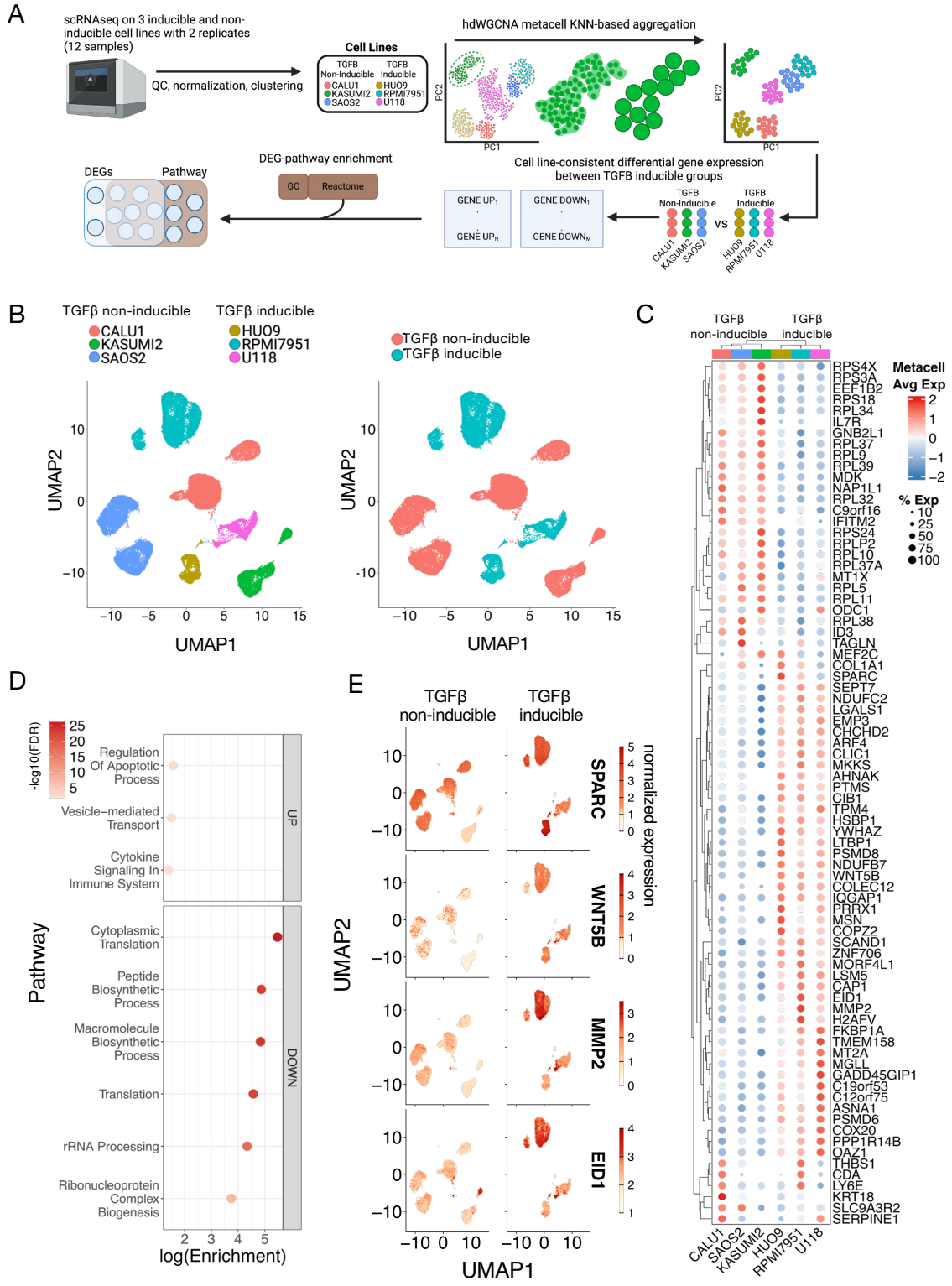


FIGURE 2. ScRNAseq reveals distinct transcriptional signatures in TGF β -inducible cancer cell lines. (A) Schematic overview of the scRNAseq workflow. TGF β -inducible (HUO9, RPMI7951, U118) and TGF β non-inducible (CALU1, KASUMI2, SAOS2) cell lines were sequenced after TGF β stimulation. Gene expression data were subjected to quality control, normalization, and clustering, followed by hdWGCNA metacell aggregation. DEGs between TGF β -inducible and non-inducible cell lines were identified and enriched for pathways in Gene Ontology (GO) and Reactome databases using hypergeometric tests implemented in Enrichr. (B) UMAP visualization of scRNAseq data from TGF β -inducible (blue) and non-inducible (red) cell lines. Cell lines did not cluster by TGF β -inducibility. (C) Heatmap of metacell-level expression of large-effect DEGs ($|\log_2FC| > 0.5$) across TGF β -inducible (blue) and non-inducible (red) cell lines, represented by average expression (high = red, low = blue) and percent metacell expression by dot size. (D) Pathway enrichment analysis of DEGs between TGF β -inducible and non-inducible cells. Upregulated DEGs were enriched in apoptotic processes and cytokine signaling, while downregulated genes were associated with translation and ribosomal function. (E) UMAP plots showing single-cell expression patterns of key upregulated genes in TGF β -inducible cells, including *SPARC*, *WNT5B*, *MMP2*, and *EID1*. These genes demonstrated a marked increase in expression in TGF β -inducible cells compared to non-inducible cells, consistent with metacell analysis.

4.5. Network analysis of TGF β -responsive transcriptional signatures

To further elucidate molecular mechanisms involved in the TGF β -LRRC15 axis, and to better understand the biological role of the DEGs within LRRC15's regulation, we employed

scRNAseq-based gene network modeling approaches to capture both gene regulatory networks (GRNs) and gene coexpression signatures that distinguished the TGF β -responsive cell lines (Figure 3A). GRNs consist of nodes and edges representing genes and regulatory interactions, respectively. To construct a GRN for the TGF β -LRRC15 axis, we used SCING [21], a bagging gradient-boosting machine learning approach to predict regulatory relationships between genes. This method was previously shown to effectively predict gene perturbation effects and uncover key driver genes for disease [21]. We incorporated all samples to build an aggregate GRN and identified 41 highly connected SCING GRN modules through Leiden clustering [22]. We also constructed a gene co-expression network across samples using hdWGCNA based on gene correlation [19], identifying 25 co-expression modules. The expression levels of individual gene regulatory or coexpression modules from both SCING and hdWGCNA networks were computed for each cell and subsequently for each metacell using hdWGCNA's module eigengene calculation [19]. Modules associated with TGF β inducibility were identified (Figure 3A).

We identified differential expression in SCING modules S1, S3, and S4, and hdWGCNA modules H1 and H3 (Figure 3B) that consistently differentiated TGF β -inducible from non-inducible cell lines, and 11 other modules with consensus across 5 cell lines (Supplemental Figure 2A). Gene Ontology and Reactome pathway analysis revealed upregulation of biological pathways related to apoptotic processes and cytokine and immune signaling, with a downregulation of translation (consistent with DEG analysis in Figure 2D), cell motility regulation and DNA damage response in TGF β -inducible cell lines. UMAP visualization of the cellular expression of the modules and their associated pathways confirmed these patterns

(Figure 3C). Surprisingly, cell motility pathways were also downregulated in TGFβ-inducible cell lines (Figure 3C), which contrasted LRRC15's proposed role as a driver of invasiveness and cell migration in tumor cells.

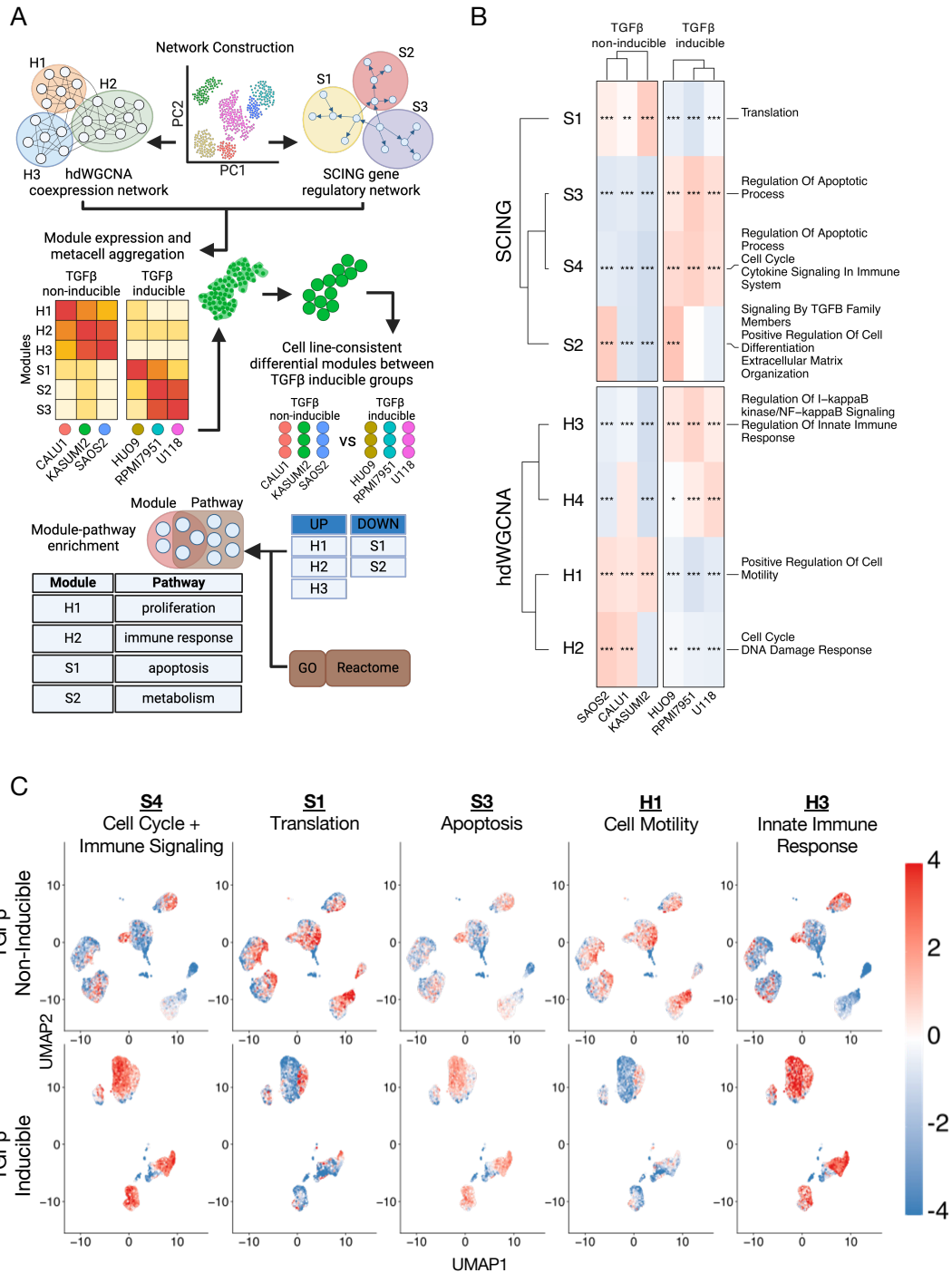


FIGURE 3. Network analysis of TGF β -responsive transcriptional signatures. (A) SCING and hdWGCNA were used to model gene regulatory networks and coexpression networks, respectively, in TGF β -responsive and non-responsive cell lines. SCING GRNs were constructed to predict regulatory relationships between genes and identify SCING modules containing genes with regulatory relationship. hdWGCNA co-expression networks were built to capture gene coexpression relations and identify coexpression modules. Expression patterns of SCING and hdWGCNA modules in metacells were compared between TGF β -inducible and non-inducible cell lines to identify differential modules. (B) Heatmap showing expression patterns in SCING and hdWGCNA network modules across cell lines. Modules upregulated and associated with TGF β responsiveness (in red) included pathways related to cell cycle, cytokine signaling, immune response, and apoptosis. (C) UMAP plots displaying single-cell expression patterns of key biological processes of network modules in TGF β -inducible (top) and non-inducible (bottom) cell lines, confirming the patterns seen in (B).

4.6. Integrated high-throughput drug screening and scRNAseq data reveals converging molecular pathways involved in LRRC15's regulation

After identifying modules and DEGs associated with TGF β inducibility from scRNAseq analysis, we combined these results to carry out an in-silico drug screen to identify the top candidate drugs and genes within the TGF β -LRRC15 axis (Figure 4A) and further integrated the results with those from the in-vitro drug screen (Figure 1). The L1000 database is a curated library of thousands of compounds and their corresponding affected genes, based on in-vitro screening assays across different organisms, tissues, drug dosages, and timepoints [23]. After

filtering the database for all human drug signatures, we performed a Fisher's exact test against hdWGCNA- and SCING-derived network modules, all significant (adjusted p-value < 0.05) DEGs, and all large-effect DEGs ($|\log_2FC| > 0.5$) to identify L1000 compounds that, upon treatment, displayed gene signatures that overlapped with our scRNAseq findings (Figure 4A). This in-silico drug screening identified 26 compounds whose gene signatures matched our scRNAseq results, and that were also present in our in-vitro drug screen (Figure 1D). We also identified 14 gene targets shared across all analyses (Figure 4B, Table 1). Visualizing these gene targets around *TGF β 1* and *LRRC15* in the SCING GRN revealed interconnected subnetworks with potential regulators of the TGF β -LRRC15 axis (Figure 4C).

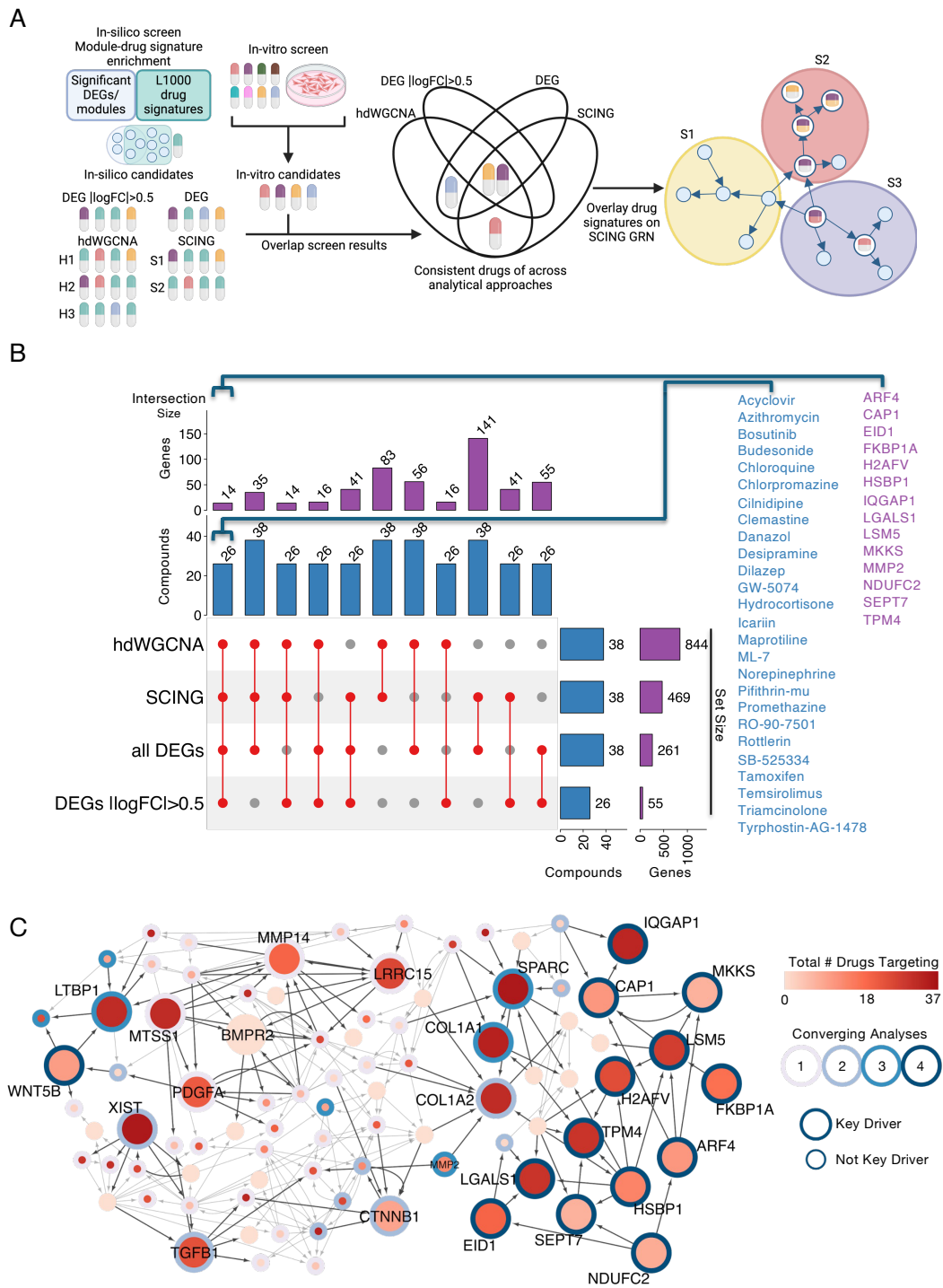


FIGURE 4. Integration of high-throughput drug screening and scRNAseq reveals converging molecular pathways regulating LRRRC15 in TGF β -inducible cells. (A) In-silico

and in-vitro drug screening approaches were combined to identify candidate compounds targeting the TGF β -LRRC15 axis. The in-silico screen utilized the L1000 drug database to map compounds against DEGs and differential hdWGCNA and SCING modules, identifying drug and corresponding genes signatures consistent across analyses. Overlap between the in-silico and in-vitro drug screens against scRNAseq results highlighted 26 compounds as top candidates for targeting LRRC15 regulation. **(B)** Illustration of the overlap between hdWGCNA, SCING, and DEG datasets, highlighting 26 candidate compounds hits from screening (Figure 1) and 14 gene targets shared across analyses. **(C)** Visualization of gene targets in a gene regulatory network. Key driver analysis revealed potential regulators (larger nodes) of the TGF β -LRRC15 pathway. Circle fill indicates the total number of compounds targeting each gene, and the number of overlapping analyses identifying the gene as significant is denoted by outline color intensity.

Gene	Average Expression Log2 Fold Change	Significant Modules	Compounds
<i>LGALS1</i>	2.63	S3, S4, H1, ALL_DEG, DEG_0.5	Danazol, GW-5074, Hydrocortisone, RO-90-7501, Rottlerin, Bosutinib, Budesonide, Cilnidipine, Dilazep, Perphenazine, Pifithrin-mu, Pimozide, SB-525334, Tamoxifen, Tamsulosin, Tyrphostin-AG-1478, Chlorpromazine, Clemastine, Desipramine, Triamcinolone, Acyclovir, Azithromycin, BW-723C86, Chloroquine, Clomipramine, Maprotiline, Mibefradil, Norepinephrine, TTNPB
<i>SPARC</i>	1.96	S4, ALL_DEG, DEG_0.5	Bosutinib, Budesonide, Chlorpromazine, Danazol, Desipramine, GW-5074, Hydrocortisone, Maprotiline, Promethazine, Rottlerin, SB-525334, Tamoxifen, Tamsulosin, Triamcinolone, Tyrphostin-AG-1478, Acyclovir, Bexarotene, Chloroquine, Cilnidipine, Clemastine, Desmethyldiazepam, Dilazep, Mibefradil, Perphenazine, RO-90-7501, TTNPB, Arvanil,

			Azithromycin, BW-723C86, Clomipramine, Flupentixol, Icarin, Pifithrin-mu, Pimozide, Tenidap
<i>FKBP1A</i>	1.74	S3, S4, H1, ALL_DEG, DEG_0.5	Tyrphostin-AG-1478, Chlorpromazine, Danazol, Hydrocortisone, Budesonide, Chloroquine, Mibefradil, Tamoxifen, Temsirolimus, TTNPB, Cilnidipine, GW-5074, Pifithrin-mu, Pimozide, Rottlerin, Tenidap, Triamcinolone
<i>TPM4</i>	1.51	S3, S4, H1, ALL_DEG, DEG_0.5	Chlorpromazine, Promethazine, RO-90-7501, Rottlerin, Budesonide, Dilazep, Hydrocortisone, Tamoxifen, Temsirolimus, Tyrphostin-AG-1478, Acyclovir, Azithromycin, Bosutinib, Cilnidipine, GW-5074, ML-7, Norepinephrine, Perphenazine, Pimozide, Triamcinolone, BW-723C86, Chloroquine, Clomipramine, Danazol, Flupentixol, Maprotiline, Pifithrin-mu, SB-525334, TTNPB
<i>MMP2</i>	1.48	H1, ALL_DEG, DEG_0.5	Cilnidipine, Desipramine, GW-5074, Norepinephrine, Perphenazine, Clemastine, Hydrocortisone, Maprotiline, Pifithrin-mu, Pimozide, RO-90-7501, Triamcinolone, Tyrphostin-AG-1478
<i>HSBP1</i>	1.24	S3, S4, H1, ALL_DEG, DEG_0.5	Promethazine, GW-5074, Rottlerin, Tamoxifen, Bexarotene, Hydrocortisone, Azithromycin, Budesonide, Chloroquine, Chlorpromazine, Cilnidipine, ML-7, Pifithrin-mu, Triamcinolone
<i>H2AFV</i>	1.13	S3, S4, H1, ALL_DEG, DEG_0.5	Danazol, Hydrocortisone, Promethazine, Rottlerin, Budesonide, Chlorpromazine, Desipramine, Dilazep, GW-5074, Icarin, Perphenazine, Tamoxifen, Tyrphostin-AG-1478, Acyclovir, Cilnidipine, Clomipramine, RO-90-7501, SB-525334, Triamcinolone, Chloroquine, Mibefradil, Pimozide, Tenidap, TTNPB
<i>ARF4</i>	1.04	S3, S4, H1, ALL_DEG, DEG_0.5	Danazol, Tyrphostin-AG-1478, Chlorpromazine, Cilnidipine, Rottlerin, Chloroquine, GW-5074, Hydrocortisone, Mibefradil, Pimozide, Tamoxifen
<i>LSM5</i>	1.01	S3, S4, H1, ALL_DEG, DEG_0.5	Chlorpromazine, Danazol, GW-5074, RO-90-7501, Rottlerin, Bosutinib, Budesonide, Cilnidipine, Desipramine, Hydrocortisone, Perphenazine, Pifithrin-mu, Pimozide, Temsirolimus, Acyclovir, Chloroquine, Clemastine, Dilazep, Norepinephrine, Tamoxifen, TTNPB, Tyrphostin-AG-1478, Arvanil, BW-723C86, Maprotiline, SB-525334, Triamcinolone
<i>EID1</i>	0.97	S3, S4, H1, ALL_DEG, DEG_0.5	Cilnidipine, Budesonide, Desipramine, GW-5074, Hydrocortisone, Perphenazine, RO-90-7501, TTNPB, Acyclovir, Arvanil, Azithromycin, Bosutinib, Chlorpromazine, Clemastine, Desmethylclozapine, Rottlerin, SB-525334, Tamoxifen, Triamcinolone
<i>SEPT7</i>	0.9	S3, S4, H1, ALL_DEG, DEG_0.5	Danazol, Desipramine, Pimozide, GW-5074, Tyrphostin-AG-1478, Bosutinib, Chloroquine

<i>MKKS</i>	0.87	S3, S4, H1, ALL_DEG, DEG_0.5	Danazol, Maprotiline, Chlorpromazine, Rottlerin, Tyrphostin-AG-1478, Mibefradil, Tenidap
<i>NDUFC2</i>	0.82	S3, S4, H1, ALL_DEG, DEG_0.5	Budesonide, Danazol, GW-5074, Bosutinib, SB-525334, Pimozide, Triamcinolone, TTNPB
<i>CAP1</i>	0.77	S3, S4, H1, ALL_DEG, DEG_0.5	GW-5074, Promethazine, Budesonide, Rottlerin, Bosutinib, Tamoxifen, Maprotiline, Pifithrin-mu, Pimozide, Triamcinolone, Tyrphostin-AG-1478
<i>IQGAP1</i>	0.64	S3, S4, H1, ALL_DEG, DEG_0.5	GW-5074, Hydrocortisone, RO-90-7501, Rottlerin, Tamoxifen, Tyrphostin-AG-1478, Budesonide, Chlorpromazine, Norepinephrine, Perphenazine, Pimozide, Temsirolimus, Acyclovir, Azithromycin, Chloroquine, Cilnidipine, Clemastine, Clomipramine, Desmethylozapine, Dilazep, Mibefradil, SB-525334, TTNPB, Arvanil, Bosutinib, BW-723C86, Desipramine, Flupentixol, Icarin, Maprotiline, Tenidap, Triamcinolone
<i>WNT5B</i>	0.6	S2, H1, ALL_DEG, DEG_0.5	Budesonide, Tamoxifen, Temsirolimus, Bosutinib, Chloroquine, GW-5074, Hydrocortisone, Pifithrin-mu, RO- 90-7501, Rottlerin

TABLE 1. Top gene candidates for modulating the TGF β -LRRC15 axis.

4.7. TGF β -induced LRRC15 expression can be modulated by siRNA knockdown of candidate genes

To test the functional relevance of genes identified in overlapping analyses (Figure 4) within the TGF β -LRRC15 pathway, candidate genes were knocked down in TGF β -responsive cell lines via small interfering RNA (siRNA). Following a similar protocol to our compound screening approach (Figure 1), cells were incubated in low-serum media before transfection with the siRNA construct. After transfection, cells were treated with TGF β and assessed for LRRC15 expression via confocal microscopy. As a positive control, we validated siRNA transfection and knockdown using three LRRC15-targeting siRNAs (Figure 5A). Transfection with siLRRC15 reduced LRRC15 protein levels by an average of $98.61 \pm 0.47\%$ in untreated cells, and $94.21 \pm$

2.02% in TGF β -treated cells. As an additional control in subsequent siRNA experiments, we also utilized siRNAs targeting *TGF β 2*, given the receptor's established role in LRRC15 CAFs [13].

We then tested siRNAs targeting various genes identified as potential nodes within the TGF β -LRRC15 axis, including *EIDI*, *H2AFV*, *IQGAP1*, *LGALS1*, *MMP2*, *SPARC*, *TGF β 2*, *TPM4*, and *WNT5B* (Figure 5B). Among these, *EIDI* (EP300 interacting inhibitor of differentiation 1), significantly induced LRRC15 expression upon *EIDI* knockdown ($p = 0.0059$). As a known inhibitor of p300-mediated transcription and differentiation in fibroblast cell populations [24], the inhibition of *EIDI* may lead to upregulated p300 activity, possibly explaining the increased LRRC15 expression observed in our studies. While this finding presented an intriguing avenue for further exploration, our primary focus remained on genes whose knockdown led to reduced LRRC15 expression. In addition, we sought to focus solely on genes that were co-expressed with *LRRC15* to improve the feasibility of targeting the TGF β -LRRC15 pharmacologically. Of the genes tested, *MMP2*, *SPARC* and *WNT5B*, as well as *TGF β 2*, significantly impacted TGF β -induced LRRC15 expression in two or more cell lines, with *TGF β 2* and *SPARC* knockdown significantly reducing LRRC15 expression across multiple concentrations of TGF β treatment (Figure 5B, C). These results support the regulatory role of 4 out of the 9 tested candidate genes in activating the TGF β -LRRC15 axis and promoting *LRRC15* expression. Notably, the genes that were experimentally validated tended to be the ones with outgoing edges to other genes in the network (Figure 5C); outgoing network edges indicate that the gene likely functions as an upstream regulator.

4.8. Activators of LRRC15 expression correlate to immunotherapy response and tumor progression

The four genes whose knockdown consistently inhibited LRRC15 expression (*MMP2*, *SPARC*, *TGF β 2*, *WNT5B*), along with *LRRC15*, became the basis for further exploration into clinical tumor databases. Given the significant impacts of knockdown on TGF β -induced LRRC15, we reasoned that high expression these 5 genes were indicative of an active TGF β -LRRC15 axis. We first performed an independent prognostic analysis of the LRRC15 activating genes in cohorts of patients from different tumor entities including breast cancer, glioblastoma, and skin cutaneous melanoma to better understand how our tumor models translated to clinical analyses. Of the three tumor types, our signature acted as a prognostic marker only in breast cancer patients (HR: 2.50, 95% CI 1.66-3.77, $p = < 0.001$) (Supplemental Figure 6). We instead explored The Cancer Genome Atlas (TCGA) to analyze each gene's correlation to *LRRC15* across TCGA tumor types to better understand whether *LRRC15* and the potential activators of *LRRC15* were co-expressed in patient tumors [25].

Of the TCGA datasets, *LRRC15* was highly correlated with *MMP2* ($r = 0.77$, $p < 0.0005$) and *SPARC* ($r = 0.79$, $p < 0.0005$), and moderately correlated with *TGF β 2* ($r = 0.35$, $p < 0.0005$) in lung squamous cell carcinoma (LUSC) (Figure 5D). Given the strong correlation of 3 out of 4 genes within LUSC tumors, along with LRRC15's known role in anti-PD1 immunotherapy resistance, we applied our signature to an anti-PD1 immunotherapy trial involving LUSC patients to evaluate whether it could predict immunotherapy resistance. When the genes were assigned weights using an eigenvector principal component weighted analysis, and patients were stratified based on the median expression of the signature, we found that *LRRC15* plus the four

LRRC15 activating genes significantly predicted survival outcomes in LUSC ($p = 0.044$, 13 patients) (Figure 5E). To validate these findings further, we investigated the role of these genes in additional anti-PD1 patient cohorts across other tumor types. We next tested our *LRRC15* expression activators in a clear cell renal cell carcinoma (ccRCC) anti-PD1 cohort. Similarly, high expression of *WNT5B*, *TGF β R2*, *SPARC*, *MMP2*, and *LRRC15* significantly predicted 2-year survival outcomes ($p = 0.035$, 24 patients). Notably, when *LRRC15* was removed from analysis, the remaining four genes (*MMP2*, *SPARC*, *WNT5B*, *TGF β R2*) failed to predict outcomes (Supplemental Figure 8). However, using *LRRC15* alone did not have the predictive power (Supplemental Figure 8A), emphasizing the importance of the cooperation and co-expression of the 5 genes in contributing to prognostic accuracy.

We evaluated a third cohort from a metastatic bladder cancer trial where patients received atezolizumab (anti-PD1) immunotherapy and were profiled for immune phenotypes based on CD8+ T-cell infiltration within the tumor and surrounding peritumoral region [26]. Before undergoing treatment, patients were categorized as “infiltrated” (CD8+ T-cells present within the tumor), “excluded” (CD8+ T-cells confined to the tumor stroma), or “desert” (absence of CD8+ T-cells). Given previous studies implicating *LRRC15*+ cancer-associated fibroblasts (CAFs) in T-cell exclusion and exhaustion, we tested the predictive power of the *LRRC15*-activating genes using transcriptomic data from immune-excluded tumors prior to anti-PD1 therapy. Our analysis demonstrated that high expression of the 5 genes was significantly predictive of patient prognosis ($p = 0.012$, 113 patients) in immune-excluded tumors (Figure 5F). In contrast, gene expression showed no significant predictive power in tumors classified as immune-infiltrated or desert, or with *LRRC15* alone (Supplemental Figure 7B, 8C). These

findings indicate that expression of *MMP2*, *SPARC*, *WNT5B* and *TGFβR2*, alongside *LRRC15*, can predict patient prognosis and overall response immunotherapy in immune-excluded tumors, and can accurately reflect the pathobiological consequences of TGFβ-LRRC15 axis signaling. While further analysis is needed, it is likely that immune-excluded tumors harbor large populations of LRRC15+ CAFs and tumor cells, which may contribute to the poor therapeutic response observed by creating a physical barrier as well as imposing immunomodulatory effects. Together, these findings underscore the critical role of LRRC15, along with several key genes within the TGFβ-LRRC15 axis, in shaping the immune-excluded tumor microenvironment. This gene set not only offers a potential biomarker for predicting immunotherapy resistance but also highlights novel therapeutic avenues for targeting LRRC15+ cell populations in resistant cancers.

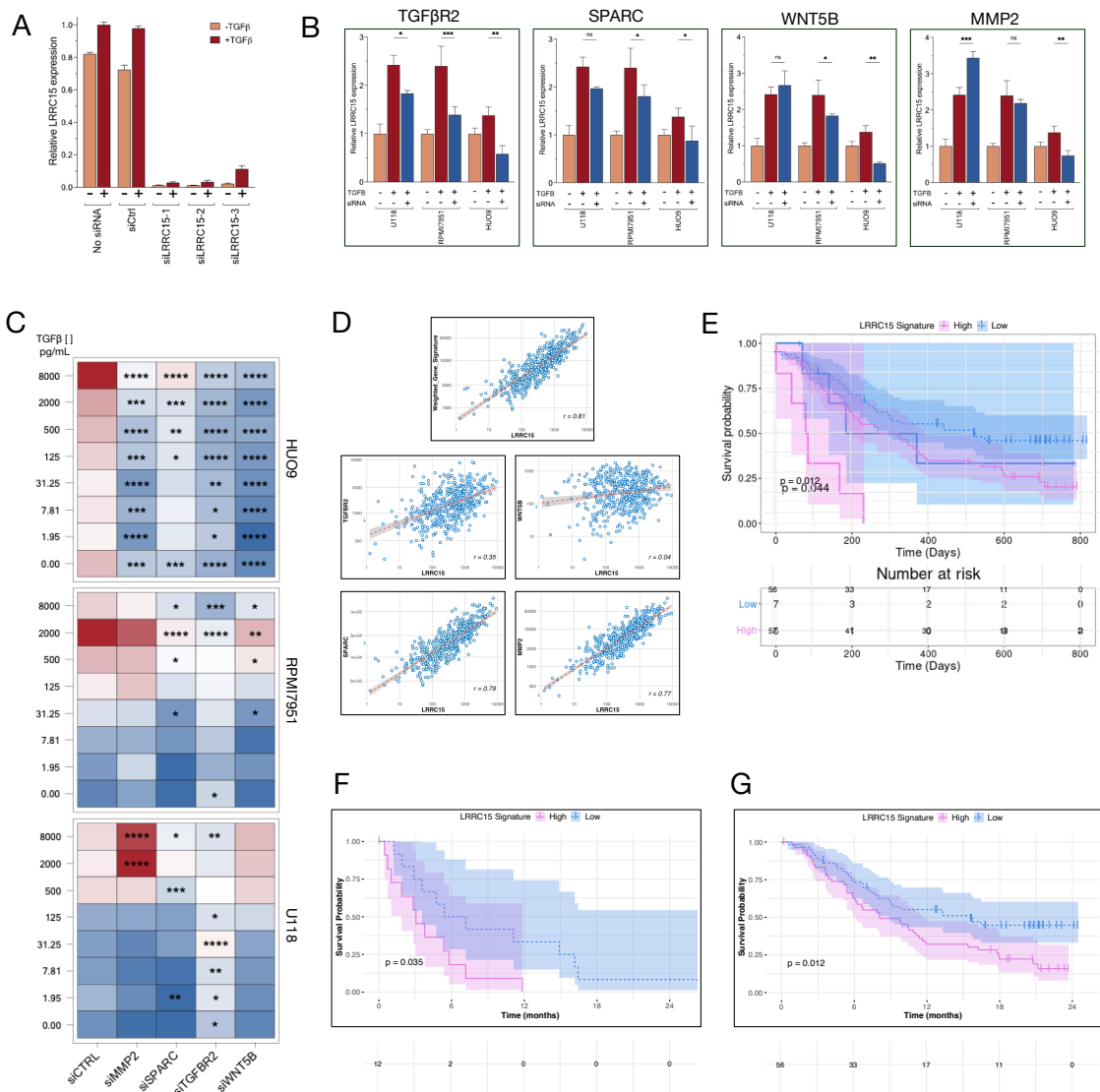


FIGURE 5. High expression of LRRC15 activating genes predicts immunotherapy resistance and tumor progression. (A) Control experiments using LRRC15-targeted siRNA in TGFβ-responsive cancer cell lines significantly reduced LRRC15 expression, overcoming TGFβ-induced upregulation ($p < 0.0005$). **(B)** Response to siRNA knockdown of target genes identified within the TGFβ-LRRC15 axis from integrated analysis of scRNAseq and compound screening is not consistent across cell lines, highlighting the importance of genetic background within the TGFβ-LRRC15 pathway. **(C)** Heatmap of LRRC15 staining intensity after siRNA

gene knockdown across increasing TGF β concentrations. Significant reductions in LRRC15 expression were observed for *TGF β 2*, *SPARC*, *WNT5B*, and *MMP2* in osteosarcoma (HUO9), while effects gene knockdown in melanoma (RPMI7951), and glioblastoma (U118) cells were less ubiquitous. **(D)** Correlation plots of LUSC tumor expression from the TCGA database reveal a strong correlation between *LRRC15* and *MMP2* ($r = 0.77$) and *SPARC* ($r = 0.79$), but weak correlations between *LRRC15*, *WNT5B*, and *TGF β 2*. There is also a strong correlation between the four genes and *LRRC15* ($r = 0.81$). **(E)** Kaplan-Meier survival curve demonstrating the predictive power of the 5 genes (including LRRC15) in LUSC patients treated with anti-PD1 immunotherapy. Patients stratified by high (red) vs. low (blue) gene expression had significantly different survival outcomes ($p = 0.044$). **(F)** Kaplan-Meier survival analysis in metastatic clear cell renal cell carcinoma patients receiving anti-PD1 therapy. The *LRRC15*-related genes significantly predicted 2-year survival outcomes in ccRCC patients ($p = 0.035$). **(G)** Finally, in metastatic bladder cancer patients receiving atezolizumab (anti-PD1) immunotherapy, high expression of *LRRC15*-related genes was significantly predictive of poorer prognosis in immune-excluded tumors ($p = 0.012$), with no significant predictive power in immune-infiltrated or desert tumors (Supplemental Figure 8B).

4.9. Discussion

Deciphering the intricate molecular pathways, genomic determinants, and tumor microenvironmental factors that regulate biomarker dynamics is pivotal for refining targeted diagnostic and therapeutic approaches in oncology. Detailed knowledge of these factors enables the stratification of patient populations most likely to respond to specific treatments, thereby

enhancing clinical efficacy [27-28]. The absence of pathobiological understanding is a major contributor to the substantial attrition rates in clinical oncology trials, where nearly half of failures are attributed to lack of established relevance of the target to the disease phenotype [27]. With the surge in oncology target and biomarker discovery, the translation of these findings into clinically beneficial entities remains elusive, highlighting the critical need for comprehensive molecular profiling to fully realize the promise of personalized medicine in cancer care.

The initial identification of LRRC15's regulation by TGF β in MSCs under prolonged supraphysiological cytokine levels [16] prompted a reevaluation of its translational relevance. To address this, our study aimed to investigate LRRC15 regulation under shorter durations and physiologically relevant concentrations of TGF β . As tumors progress, CAFs and cancer cells increasingly exhibit similar behaviors and interactions, enhancing tumor complexity and resilience. Both cell types are responsive to extracellular molecules such as growth factors and cytokines and are subject to frequent genetic alterations, with cancer cells commonly inducing expression changes in CAFs via paracrine signaling, which can lead to selective CAF expansion [29-30]. Furthermore, CAFs can maintain tumor-promoting properties independent of direct interactions with cancer cells [31]. This convergence of characteristics guided our focus to LRRC15+ MSC-derived cancer cells for deeper insights.

Our investigation revealed two distinct cellular responses to TGF β following cytokine withdrawal: one subset of cell lines demonstrated LRRC15 upregulation, suggesting an adaptive mechanism, while another remained unaffected. Integrative analysis using scRNAseq, chemical compound screening, and siRNA knockdown pinpointed *TGF β R2*, *WNT5B*, *SPARC*, and *MMP2* as key mediators inducing TGF β -LRRC15 activity. In patient tissue databases, the impact of

these genes on TGF β -LRRC15 activity was observed across a wide range of solid tumors (Supplemental Figure 5), including those demonstrating expression exclusively in CAFs but not in cancer cells. Moreover, a significant correlation emerged with a previously identified *LRRC15*-containing 11-gene panel (Supplemental Figure 9), which was obtained by screening of CAFs in TGF β -driven tumor microenvironments in PDAC patients [14].

LRRC15, together with the four genes regulating its expression, differentiated survival rates and disease progression in tumor settings that were characterized by the exclusion of CD8⁺ T cells and resistance to ICTs. However, we did not find significant prognostic value in tumors categorized as immune-infiltrated or immune-desert. It could be speculated that these variations may be attributed to immunological mechanisms driven by non-*LRRC15* related mechanisms.

Among the four genes within the TGF β -LRRC15 axis, *TGF β R2* has previously been established as a regulator of LRRC15⁺ CAF formation in GEMM models [13]. Tumor fibrosis is a common consequence of aberrant TGF β signaling, contributing to immune cell exclusion in the stroma-rich ECM and poor drug delivery [32]. Several of these ECM components were significantly co-expressed with LRRC15, such as matrix metalloproteinases (*MMP2*, *MMP14*) and collagen genes (*COL1A1*, *COL1A2*). Further, *MMP2* plays a critical role in cancer cells by promoting angiogenesis and cell growth, and by facilitating collagen degradation in the TME, thereby aiding tumor invasion. This highlights its dual function in promoting cancer progression and supporting CAF populations. In parallel, *SPARC*, a secreted protein of the extracellular matrix, has been shown to synergize with TGF β signaling to boost collagen production and induce canonical TGF β signaling pathways, such as SMAD2 activation [33]. While further research is

necessary to fully delineate *SPARC*'s function in tumor tissues, existing studies indicate that its knockdown in pterygium fibroblasts diminishes TGF β signaling and *MMP2* expression [34], potentially leading to a similar effect on LRRC15+ CAF and cancer cell interactions.

In the current study, we identified a broad spectrum of potential regulatory genes, however, siRNA knockdown of certain genes, such as *H2AFV*, did not significantly affect TGF β -induced LRRC15 expression in our cancer cell models. The lack of significant effects on TGF β -induced LRRC15 expression could stem from several main factors. First, these genes tend to have more incoming edges (i.e., receivers of regulation by other genes) than outgoing edges (i.e., acting as upstream regulators) in the networks. Second, although *H2AFV* is upregulated in various cancers, it primarily operates through epigenetic mechanisms such as DNA methylation reprogramming [35]. The epigenetic influence of H2A and its variants, which often have overlapping functions, adds a layer of complexity to gene regulation [36]. Lastly, even with effective siRNA transfection, residual protein expression might maintain *H2AFV*'s role within the TGF β -LRRC15 axis [37]. Further investigations, possibly employing CRISPR/Cas9 gene editing for more complete gene disruption, are necessary to fully understand these genes' involvement in LRRC15 expression [38].

Our pioneering small molecule screens identified a multitude of compounds capable of disrupting the TGF β -LRRC15 pathway (Figure 1), potentially providing alternative strategies to overcome the pro-tumorigenic effects of TGF β without direct inhibition of the pathway itself. This is especially important given the clinical challenges associated with TGF β receptor inhibitors, where inhibition often leads to adverse off-target effects. For example, bosutinib, a

Bcr-Abl tyrosine-kinase inhibitor, is actively studied in chronic myeloid leukemia (CML) as a combination therapy with anti-PD1 immunotherapy [39]. In solid tumors, bosutinib may be able to play a similar complementary role to immune checkpoint blockade by inhibition of TGF β -related immunosuppressive pathways. In addition, the significant downregulation of DNA damage response processes in TGF β -inducible cell lines may expose a potential therapeutic vulnerability in these cell populations. The positive hits identified from our drug screening, particularly those supported by both in-vitro and in-silico screens, could be further explored for such applications in the future.

Upon exploring LRRC15 as a biomarker for therapeutic resistance, our analysis of TCGA sarcoma datasets suggested that *LRRC15* alone is insufficient as a prognostic biomarker for aggressive disease and overall survival and is not predictive of therapeutic outcomes in immunotherapy trials (Supplemental Figure 7C). Our *in vitro* observations diverge from both prior preclinical data and clinical findings, as our CRISPR-mediated knockout of LRRC15 did not yield significant changes in aggressive cellular growth patterns associated with LRRC15 expression in clinical contexts (data not shown). This discrepancy highlights that LRRC15 alone may not solely drive tumor aggressiveness. Integrating the results of this study, we hypothesize that LRRC15 functions primarily as a bystander protein, indicative of an extensive network of TGF β -driven pathobiological processes prevalent in the microenvironment of aggressive, immunoresistant tumors.

We have previously demonstrated that LRRC15-targeted PET and SPECT imaging is applicable for non-invasive detection, quantification, and monitoring of lesion-specific LRRC15 [15].

LRRC15, with its low expression in non-cancerous and healthy tissues and high expression in aggressive tumors, serves as an ideal therapeutic target for RIT. This strategy facilitates the selective delivery of cytotoxic radionuclides to specifically target and ablate both cancer cells and CAFs that contribute to treatment resistance and metastatic growth. In addition to the ablation of LRRC15+ cell populations, tumors treated with ¹⁷⁷Lu-LRRC15-RIT exhibited downregulation of *SPARC*, *MMP2*, *TGFβR2*, and *WNT5B* (Supplemental Figure 4). These findings partially confirm that *LRRC15* is co-expressed with other crucial factors involved in driving tumor progression and resistance.

Finally, with the integration of next-generation sequencing and comprehensive genomic profiling in clinical decision making, it has become possible to stratify patients more accurately based on tumor molecular profiles [40]. Large-scale studies like NCI-MATCH have successfully matched patients to treatment options, with 38% of patients having tumor molecular profiles that were actionable by currently available clinical trials [41-42]. Other molecular sequencing studies such as ComboMATCH have expanded beyond simple biomarker analysis to incorporate circulating tumor DNA (ctDNA), histology, and RNA sequencing of patient tumors [43], highlighting the feasibility of applying assessment of LRRC15-related profiles to guide decision-making and individualized treatment in a clinical setting.

In summary, by computationally integrating high-throughput small molecule screening data with scRNA sequencing, we identified *TGFβR2*, *MMP2*, *SPARC*, and *WNT5B* as key mediators driving LRRC15 upregulation in response to TGFβ signaling. These molecules, secreted by both cancer cells and fibroblasts, are critical in promoting EMT, during which LRRC15 expression

is significantly elevated. Their coordinated activity shapes a fibrotic and immunosuppressive tumor microenvironment, predicting resistance to immune checkpoint inhibitors and correlating with aggressive cancer phenotypes. These findings elucidate the molecular architecture of the TGF β -LRRC15 axis, revealing a cascade of effector molecules that present potential targets for the development of inhibitors and modulators to disrupt these pathways. This improved understanding may also provide insight into the mechanisms underlying immunoresistance, offering a basis for exploring novel diagnostic and therapeutic strategies to enhance the efficacy of immunotherapy.

4.10. References

1. Bierie, B. & Moses, H. L. Tumour microenvironment: TGFbeta: the molecular Jekyll and Hyde of cancer. *Nat Rev Cancer* 6, 506–520 (2006).
2. Biswas, T., Gu, X., Yang, J., Ellies, L. G. & Sun, L.-Z. Attenuation of TGF- β signaling supports tumor progression of a mesenchymal-like mammary tumor cell line in a syngeneic murine model. *Cancer Lett* 346, 129–138 (2014).
3. Massagué, J. TGF β signalling in context. *Nat Rev Mol Cell Biol* 13, 616–630 (2012).
4. Tolcher, A. W. et al. A phase 1 study of anti-TGF β receptor type-II monoclonal antibody LY3022859 in patients with advanced solid tumors. *Cancer Chemother Pharmacol* 79, 673–680 (2017).
5. Hezel, A. F. et al. TGF- β and α v β 6 integrin act in a common pathway to suppress pancreatic cancer progression. *Cancer Res* 72, 4840–4845 (2012).

6. Brandes, A. A. et al. A Phase II randomized study of galunisertib monotherapy or galunisertib plus lomustine compared with lomustine monotherapy in patients with recurrent glioblastoma. *Neuro Oncol* 18, 1146–1156 (2016).
7. Yang, Y. et al. The Outcome of TGF β Antagonism in Metastatic Breast Cancer Models In Vivo Reflects a Complex Balance between Tumor-Suppressive and Proprogression Activities of TGF β . *Clin Cancer Res* 26, 643–656 (2020).
8. Connolly, E. C. et al. Outgrowth of drug-resistant carcinomas expressing markers of tumor aggression after long-term T β RI/II kinase inhibition with LY2109761. *Cancer Res* 71, 2339–2349 (2011).
9. Derynck, R., Turley, S. J. & Akhurst, R. J. TGF β biology in cancer progression and immunotherapy. *Nat Rev Clin Oncol* 18, 9–34 (2021).
10. Cui, J. et al. Expression and clinical implications of leucine-rich repeat containing 15 (LRRC15) in osteosarcoma. *J Orthop Res* 38, 2362–2372 (2020).
11. Ray, U. et al. Exploiting LRRC15 as a Novel Therapeutic Target in Cancer. *Cancer Res* 82, 1675–1681 (2022).
12. Ray, U. et al. Targeting LRRC15 Inhibits Metastatic Dissemination of Ovarian Cancer. *Cancer Res* 82, 1038–1054 (2022).
13. Krishnamurty, A. T. et al. LRRC15(+) myofibroblasts dictate the stromal setpoint to suppress tumour immunity. *Nature* 611, 148–154 (2022).
14. Dominguez, C. X. et al. Single-Cell RNA Sequencing Reveals Stromal Evolution into LRRC15(+) Myofibroblasts as a Determinant of Patient Response to Cancer Immunotherapy. *Cancer Discov* 10, 232–253 (2020).

15. Storey, C. M. *et al.* Development of a LRRC15-Targeted Radio-Immunotheanostic Approach to Deplete Pro-tumorigenic Mechanisms and Immunotherapy Resistance. Preprint at <https://www.biorxiv.org/content/10.1101/2024.01.30.577289v1> (2024).
16. Purcell, J. W. *et al.* LRRC15 Is a Novel Mesenchymal Protein and Stromal Target for Antibody-Drug Conjugates. *Cancer Res* 78, 4059–4072 (2018).
17. Wakefield, L. M. *et al.* Transforming growth factor-beta1 circulates in normal human plasma and is unchanged in advanced metastatic breast cancer. *Clin Cancer Res* 1, 129–136 (1995).
18. Shilts, J. *et al.* LRRC15 mediates an accessory interaction with the SARS-CoV-2 spike protein. *PLoS Biol* 21, e3001959 (2023).
19. Morabito, S., Reese, F., Rahimzadeh, N., Miyoshi, E. & Swarup, V. hdWGCNA identifies co-expression networks in high-dimensional transcriptomics data. *Cell Rep Methods* 3, 100498 (2023).
20. Barata, J. T., Durum, S. K. & Seddon, B. Flip the coin: IL-7 and IL-7R in health and disease. *Nat Immunol* 20, 1584–1593 (2019).
21. Littman, R., Cheng, M., Wang, N., Peng, C. & Yang, X. SCING: Inference of robust, interpretable gene regulatory networks from single cell and spatial transcriptomics. *iScience* 26, 107124 (2023).
22. Traag, V. A., Waltman, L. & van Eck, N. J. From Louvain to Leiden: guaranteeing well-connected communities. *Sci Rep* 9, 5233 (2019).
23. Subramanian, A. *et al.* A Next Generation Connectivity Map: L1000 Platform and the First 1,000,000 Profiles. *Cell* 171, 1437-1452.e17 (2017).

24. Ghosh, A. K. & Varga, J. The transcriptional coactivator and acetyltransferase p300 in fibroblast biology and fibrosis. *J Cell Physiol* **213**, 663–671 (2007).
25. Cerami, E. et al. The cBio cancer genomics portal: an open platform for exploring multidimensional cancer genomics data. *Cancer Discov* **2**, 401–404 (2012).
26. A Study of Atezolizumab in Participants With Locally Advanced or Metastatic Urothelial Bladder Cancer (Cohort 2). Clinicaltrials.gov identifier: NCT02108652
27. Cook, D. et al. Lessons learned from the fate of AstraZeneca’s drug pipeline: a five-dimensional framework. *Nat Rev Drug Discov* **13**, 419–431 (2014).
28. Emmerich, C. H. et al. Improving target assessment in biomedical research: the GOT-IT recommendations. *Nat Rev Drug Discov* **20**, 64–81 (2021).
29. Tselou, E. & Kiaris, H. Fibroblast independency in tumors: implications in cancer therapy. *Future Oncol* **4**, 427–432 (2008).
30. Hill, R., Song, Y., Cardiff, R. D. & Van Dyke, T. Selective evolution of stromal mesenchyme with p53 loss in response to epithelial tumorigenesis. *Cell* **123**, 1001–1011 (2005).
31. Littlepage, L. E., Egeblad, M. & Werb, Z. Coevolution of cancer and stromal cellular responses. *Cancer Cell* **7**, 499–500 (2005).
32. Olive, K. P. et al. Inhibition of Hedgehog signaling enhances delivery of chemotherapy in a mouse model of pancreatic cancer. *Science* **324**, 1457–1461 (2009).
33. Carneiro, T. et al. Extracellular SPARC cooperates with TGF- β signalling to induce pro-fibrotic activation of systemic sclerosis patient dermal fibroblasts. *Rheumatology (Oxford)* **59**, 2258–2263 (2020).

34. Fan, J. *et al.* SPARC knockdown attenuated TGF- β 1-induced fibrotic effects through Smad2/3 pathways in human pterygium fibroblasts. *Arch Biochem Biophys* **713**, 109049 (2021).
35. Chew, G.-L. *et al.* Short H2A histone variants are expressed in cancer. *Nat Commun* **12**, 490 (2021).
36. Lamaa, A. *et al.* Integrated analysis of H2A.Z isoforms function reveals a complex interplay in gene regulation. *Elife* **9**, (2020).
37. Leung, J. W. C., Emery, L. E. & Miller, K. M. CRISPR/Cas9 Gene Editing of Human Histone H2A Variant H2AX and MacroH2A. *Methods Mol Biol* **1832**, 255–269 (2018).
38. Boettcher, M. & McManus, M. T. Choosing the Right Tool for the Job: RNAi, TALEN, or CRISPR. *Mol Cell* **58**, 575–585 (2015).
39. Pembrolizumab and Dasatinib, Imatinib Mesylate, or Nilotinib in Treating Patients With Chronic Myeloid Leukemia and Persistently Detectable Minimal Residual Disease. Clinicaltrials.gov identifier: NCT03516279
40. Xuan, J., Yu, Y., Qing, T., Guo, L. & Shi, L. Next-generation sequencing in the clinic: promises and challenges. *Cancer Lett* **340**, 284–295 (2013).
41. Flaherty, K. T. *et al.* The Molecular Analysis for Therapy Choice (NCI-MATCH) Trial: Lessons for Genomic Trial Design. *J Natl Cancer Inst* **112**, 1021–1029 (2020).
42. Flaherty, K. T. *et al.* Molecular Landscape and Actionable Alterations in a Genomically Guided Cancer Clinical Trial: National Cancer Institute Molecular Analysis for Therapy Choice (NCI-MATCH). *J Clin Oncol* **38**, 3883–3894 (2020).

43. Meric-Bernstam, F. *et al.* National Cancer Institute Combination Therapy Platform Trial with Molecular Analysis for Therapy Choice (ComboMATCH). *Clin Cancer Res* **29**, 1412–1422 (2023).
44. Hao, Y. *et al.* Integrated analysis of multimodal single-cell data. *Cell* **184**, 3573–3587.e29 (2021).
45. Satija, R., Farrell, J. A., Gennert, D., Schier, A. F. & Regev, A. Spatial reconstruction of single-cell gene expression data. *Nat Biotechnol* **33**, 495–502 (2015).
46. Shu, L. *et al.* Mergeomics: multidimensional data integration to identify pathogenic perturbations to biological systems. *BMC Genomics* **17**, 874 (2016).
47. Kuleshov MV, Jones MR, Rouillard AD, *et al.* Enrichr: a comprehensive gene set enrichment analysis web server 2016 update. *Nucleic Acids Res.* 2016;44(W1):W90-W97.
48. Shannon P, Markiel A, Ozier O, *et al.* Cytoscape: a software environment for integrated models of biomolecular interaction networks. *Genome Res.* 2003;13(11):2498-2504.

4.11. Supplementary figures

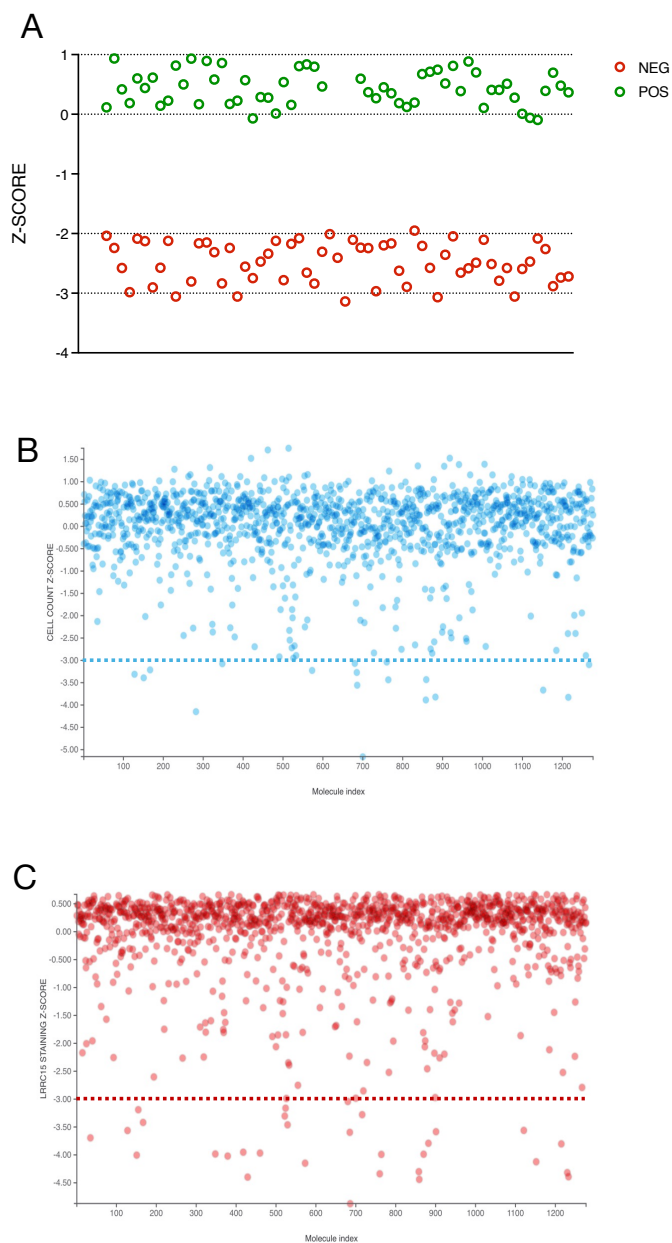


FIGURE 1. Compound screening controls. (A) Summary of TGF β -treated (POS, green) or non-treated (NEG, red) LRRC15 staining controls, represented by Z-score. (B) Cell count per well across 1,280 screened compounds, represented by Z-score. Dotted blue line represents compound toxicity cutoff where compounds were omitted due to cytotoxic effects (Z-score < -

3). (C) LRRC15 staining per well across 1,280 screened compounds, represented by Z-score. Dotted red line represents a LRRC15 staining Z-score of < -3 , which was determined to be a hit within compound screens.

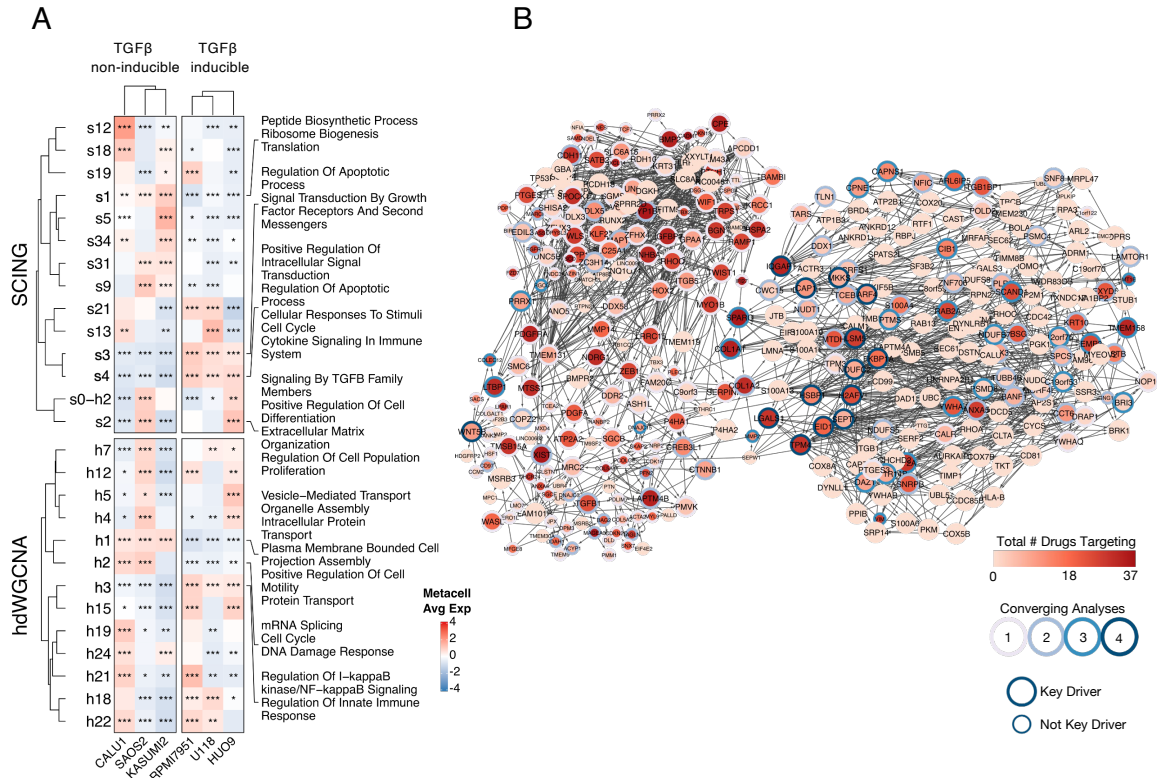


FIGURE 2. Network Analysis. (A) Differential module expression heatmap. Cell lines are grouped by TGFβ inducibility. Significance measured by one-vs-opposite group (* <0.05 , ** <0.01 , *** <0.001). (B) GRN of top drug targets.

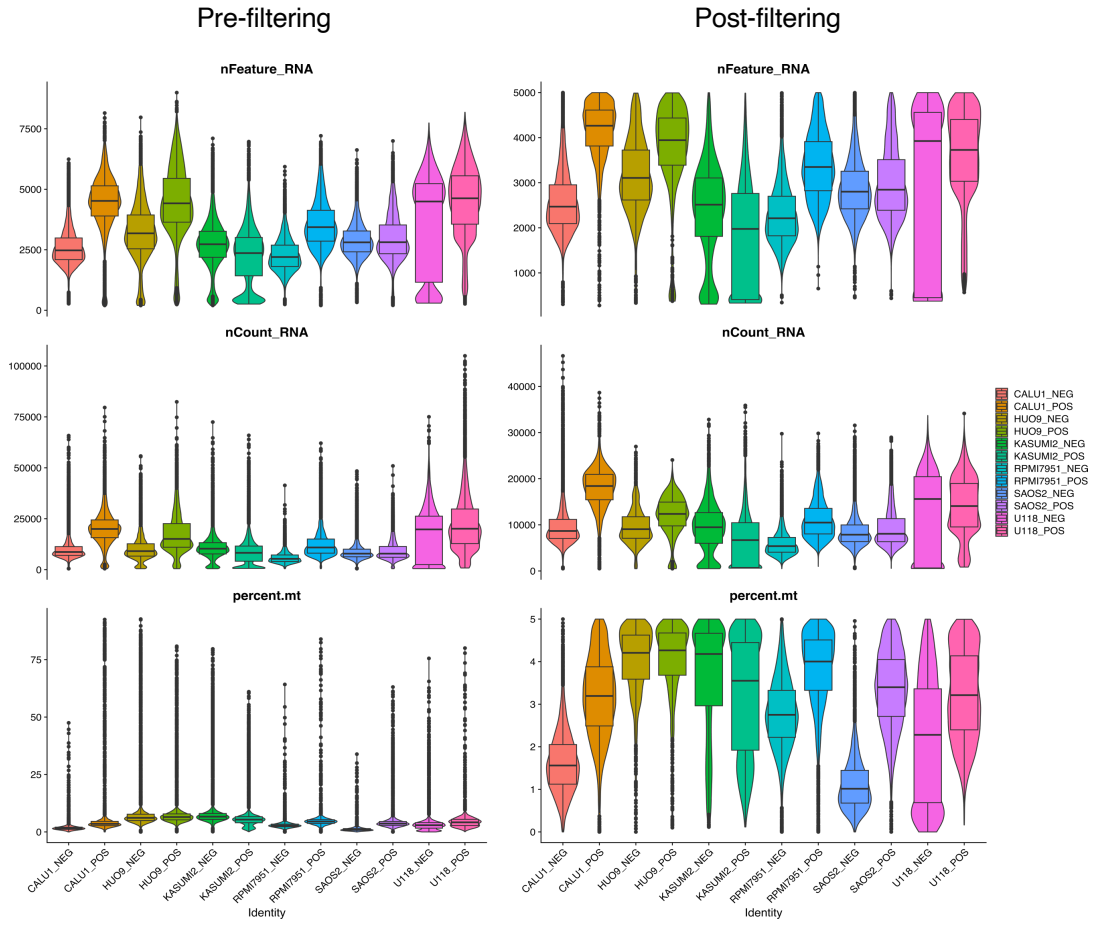


FIGURE 3. scRNAseq quality control plots pre-filtering (left) and post-filtering (right).

Top box plots are the number of genes per cell. Middle box plots are the number of UMI counts per cell. Bottom box plots are the percentage of counts mapping to mitochondrial genes per cell.

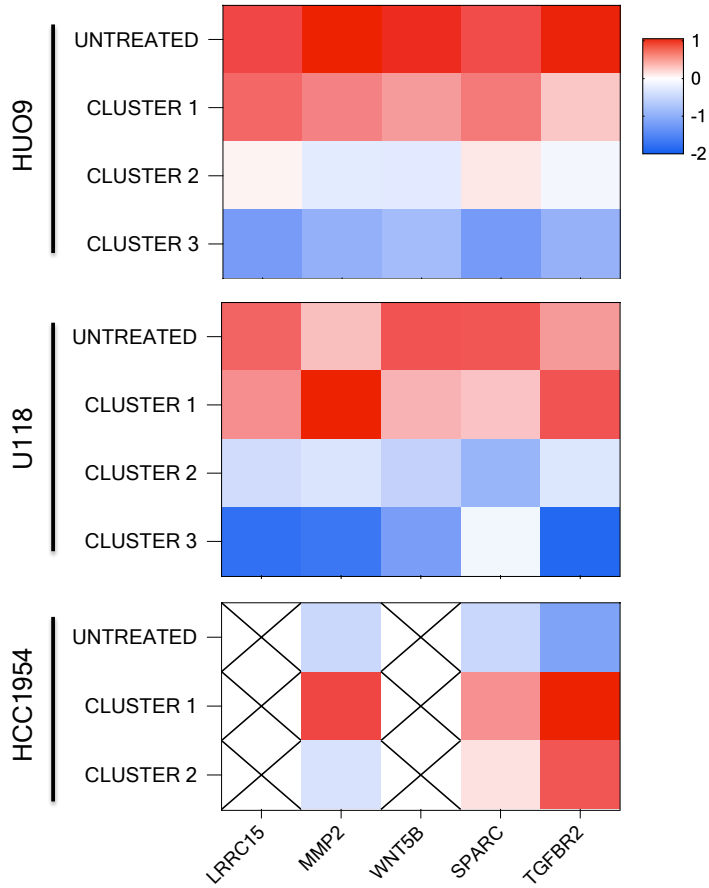


FIGURE 4. Loss of gene expression in LRRC15 activators after LRRC15-targeted radioimmunotherapy. Z-score normalized transcriptomic expression of *LRRC15*, *MMP2*, *WNT5B*, *SPARC*, and *TGFBR2* across [¹⁷⁷Lu]-DUNP19-treated HUU09 (osteosarcoma), U118 (glioblastoma), and HCC1954 (breast carcinoma) tumors. High expression (red = high) is observed in untreated tumors, while progressive loss of gene expression is observed in treated tumors (blue = low). Tumors were clustered based on principal component analysis.

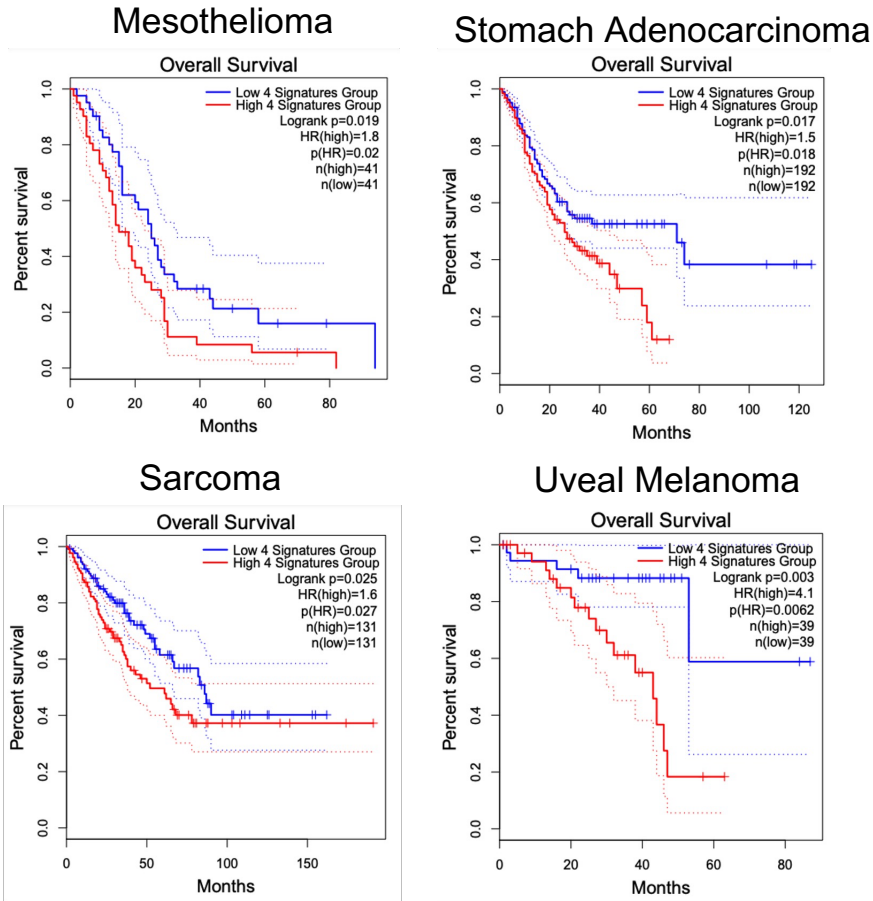
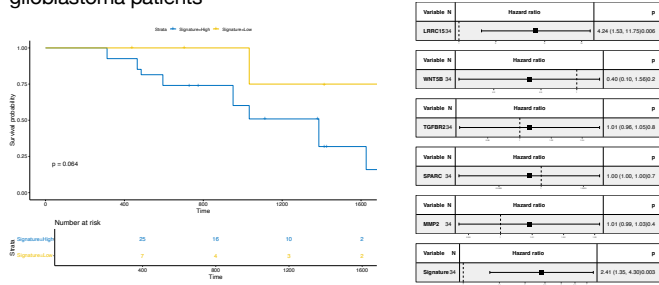
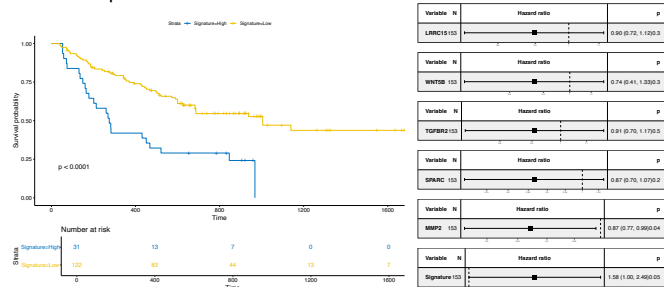


FIGURE 5. *LRRC15* expression activators predict survival in TCGA mesenchymal-derived tumors. TCGA overall survival data comparing patient survival, with high *LRRC15*, *MMP2*, *WNT5B*, *SPARC*, and *TGF β 2* gene expression (red) significantly decreasing survival probability across mesenchymal-derived tumor types.

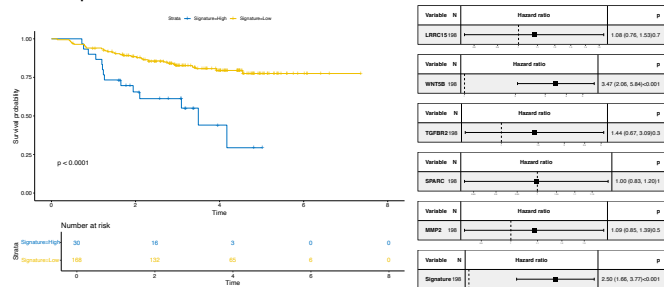
A. Progression free survival and hazard ratios of gene expression in glioblastoma patients



B. Progression free survival and hazard ratios of gene expression in melanoma patients



C. Progression free survival and hazard ratios of gene expression in breast cancer patients



D. Progression free survival and hazard ratios of gene expression in pancreatic adenocarcinoma patients

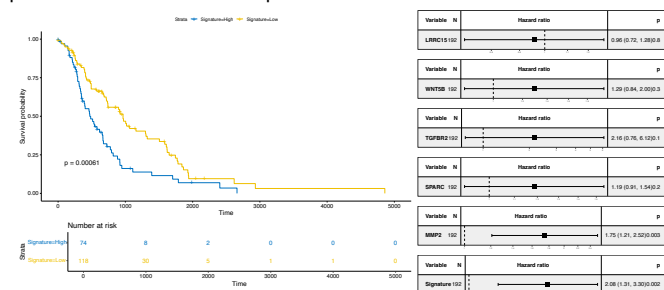
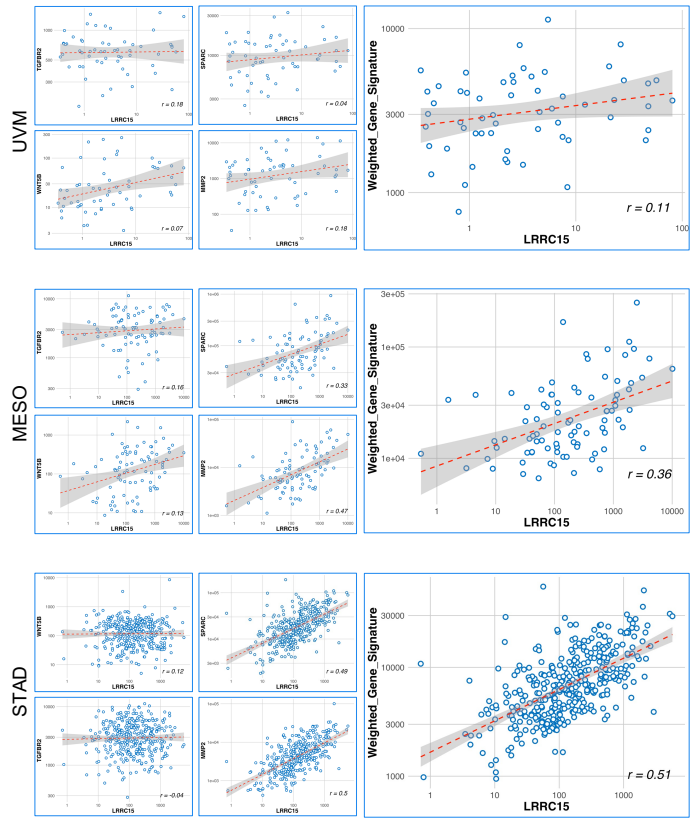


FIGURE 6. Survival and hazard ratios in tumors based on cell line models. Progression-free survival probability and hazard ratios for individual genes, as well as overall gene expression for *LRRC15*, *MMP2*, *WNT5B*, *SPARC*, and *TGFβR2*. For glioblastoma, melanoma,

and pancreatic adenocarcinoma patient cohorts, patients were not differentiated by treatment received. Within the breast cancer patient cohort, patients received taxane therapy.



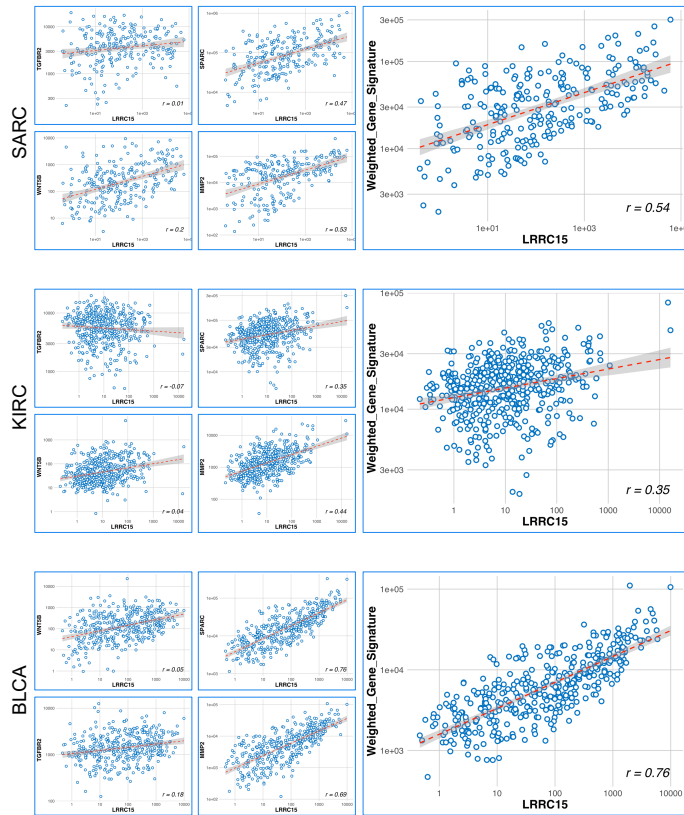
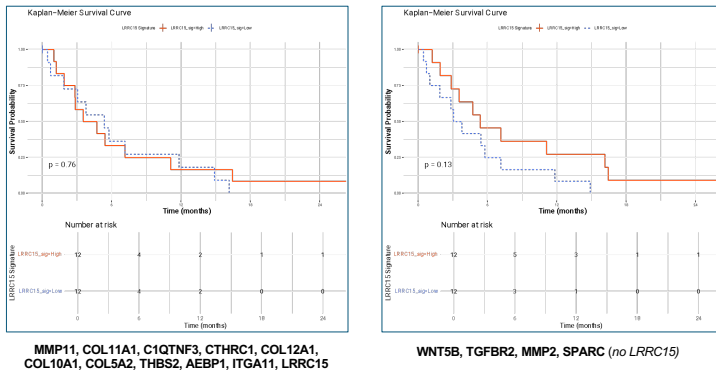
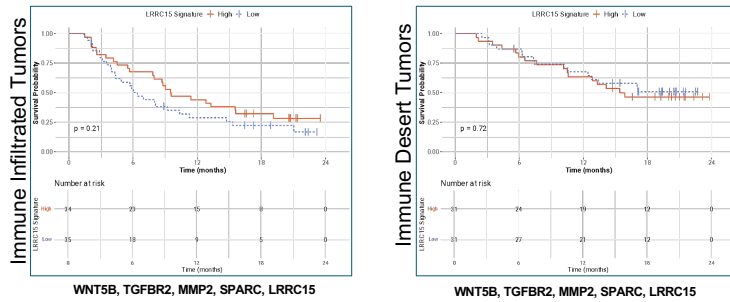


FIGURE 7. Correlation of LRRRC15-associated genes with LRRRC15 expression in TCGA tumor cohorts. Correlation plots of uveal melanoma (UVM), mesothelioma (MESO), stomach adenocarcinoma (STAD), sarcoma (SARC), kidney renal cell carcinoma (KIRC) and bladder cancer (BLCA) comparing *MMP2*, *WNT5B*, *SPARC*, and *TGFBR2* gene expression to *LRRRC15*, either individually (left plots, smaller) or together (right plot, larger). Overall, LRRRC15-related genes demonstrate a positive correlation with *LRRRC15* expression across tumor types.

A. Progression free survival in ccRCC patients treated with PD1 blockade



B. Progression free survival in bladder cancer patients treated with PD1 blockade (IMVIGOR210 trial) - segmented by immune phenotype



C. Progression free survival in bladder cancer patients treated with PD1 blockade (IMVIGOR210 trial) - segmented by immune phenotype

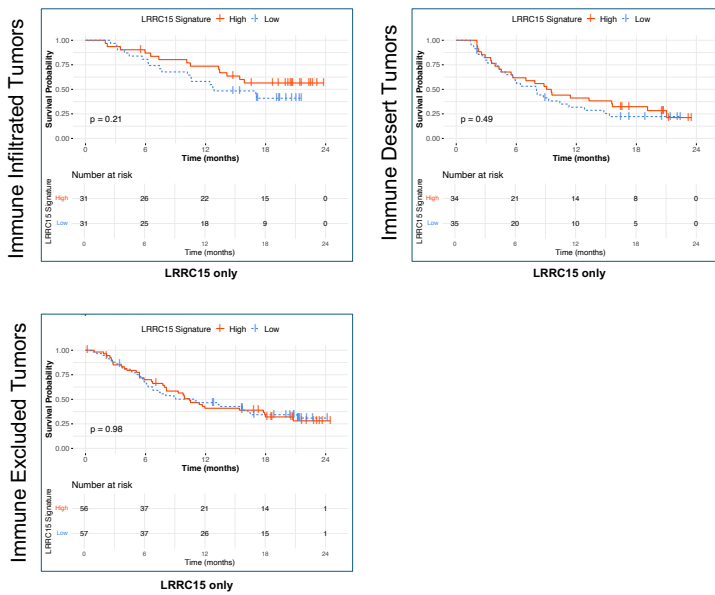


FIGURE 8. LRRC15 expression activators predict survival in patients with PD1 blockade.

(A) Progression-free survival in clear cell renal cell carcinoma patients treated with PD1 blockade. Left Kaplan-Meier plot shows no significant predictive ability in signature expression (red = high, blue = low) of a previously identified TGFβ CAF signature that includes LRRC15. Excluding LRRC15 (right plot) decreases predictive power of the LRRC15-related genes *MMP2*, *WNT5B*, *SPARC*, and *TGFβR2*.

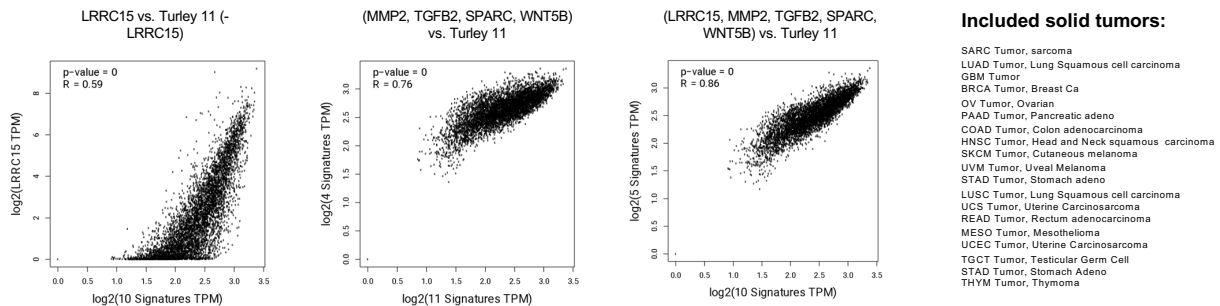


FIGURE 9. Correlation between previously identified CAF LRRC15 signatures and our

LRRC15 gene signatures. (Left) Correlation plots of solid tumor expression of previously identified TGFβ-driven CAF signature by Turley et al. (Turley-11) to LRRC15 expression (left plot). **(Middle)** Plot demonstrates a strong correlation between LRRC15-related genes *MMP2*, *WNT5B*, *SPARC*, and *TGFβR2* and the TGFβ-CAF Turley-11 signature. **(Right)** Strong correlation between *MMP2*, *WNT5B*, *SPARC*, and *TGFβR2* plus *LRRC15* and the TGFβ-CAF Turley-11 signature.

	HUO9	RPMI7951	U118
(±)-2-Amino-7-phosphonoheptanoic acid	-3.586		

(±)-Quinpirole dihydrochloride	-3.769	-3.308	-3.335
1-Methylimidazole		-3.028	-3.842
3-aminobenzamide		-3.007	-4.256
AC-93253 iodide			
AS-252424	-3.093		
Auranofin	-6.344	-3.479	-3.23
Aurothioglucose	-3.53		
Bay 11-7082			
Beclomethasone			
Betamethasone			
BIX 01294 trihydrochloride hydrate			
Brefeldin A	-4.692		
Bromoacetyl alprenolol menthane	-4.534		
Budesonide			
Chloroquine diphosphate			
Cilnidipine			
Colchicine	-3.414		
Dihydroouabain		-3.85	-3.016
Ebastine	-5.693		
Emetine dihydrochloride hydrate	-5.796		-4.387
Gossypol	-6.687		-4.296
GW5074	-4.242	-3.774	-3.025
Hydrocortisone		-3.204	-3.34
Hydroxytacrine maleate		-3.142	-3.38
JX401	-5.488		
K114			

Labetalol hydrochloride			
MDL 105,519	-3.254		
N-(3,3-Diphenylpropyl)glycinamide		-3.309	-3.326
N-Oleoyldopamine	-3.976		
Niclosamide			
NSC 95397	-3.324		
Ouabain	-4.537		
PD-161570			
PD-166285 hydrate	-3.965		
PD-184161		-3.425	-3.244
PD-407824	-4.41	-4.001	-3.015
PD173952	-3.436		
Phorbol 12-myristate 13-acetate		-3.114	-3.569
Pifithrin-mu		-3.376	-3.311
Podophyllotoxin	-3.571		
RepSox	-5.36	-3.603	-3.035
Rottlerin		-3.262	-3.34
Sanguinarine chloride		-3.491	-3.171
SB-525334	-5.045	-3.803	-3.022
Stattic	-5.231		
TBB		-3.577	-3.038
Terfenadine			
Thapsigargin	-4.334	-3.413	-3.257
Topotecan hydrochloride hydrate	-5.435		
Triamcinolone			
TTNPB		-3.399	-3.278
Tyrphostin AG 1478		-3.179	-3.354

Tyrphostin AG 879		-3.494	-3.12
Total Compound Hits	26	22	24

SUPPLEMENTAL TABLE 1. Compound hits from LOPAC1280 screen across three cell lines. Hits are represented as normalized effect on LRRC15 expression.

CHAPTER 5. CONCLUSION

5.1. Future Directions

Targeting Tumor-Stroma Interactions

While our study establishes foundational insights into TGF β -LRRC15 signaling, the limitations posed by *in vitro* models and selected cell lines underscore the need for expanded validation. Future studies should integrate syngeneic models to better replicate the tumor heterogeneity and cancer cell-stromal interactions that are a hallmark of TGF β -driven cancers. Additionally, examining variations in TGF β signaling across cancer subtypes will provide a nuanced understanding of the pathway's role in immunosuppression and metastasis, potentially identifying subtype-specific therapeutic targets.

Our study identified promising compounds, including GW-5074 and Rottlerin, which disrupt LRRC15 expression via the TGF β -LRRC15 pathway. These compounds act on key signaling nodes such as the Raf pathway and protein kinase C. These study findings also emphasize the roles of the bone microenvironment and stromal components, such as collagen and extracellular matrix proteins, which may support metastatic growth. Future research could focus on elucidating specific interactions between tumor cells and the stroma that sustain the aggressive phenotype of TGF β -driven cancers. This could involve dual targeting of stromal biomarkers (LRRC15, SPARC, MMP2) with non-canonical TGF β signaling mechanisms (for example, Raf kinase) known to remodel the CAF microenvironment and make tumors more responsive to immunotherapy [1]. In addition, other compounds targeting pathways such as autophagy (Chloroquine) and anti-inflammatory agents (Budesonide) could alleviate TGF β -induced immunosuppression. In vivo testing of these compounds in conjunction with immunotherapies

may reveal approaches to overcome resistance mediated by LRRC15 expression and enhance patient response rates.

Our scRNAseq and high-content screening analyses identified a set of genes with potential roles in modulating the TGF β -LRRC15 axis, including ARF4, IQGAP1, LGALS1, LSM5, SEPT7, TPM4, and H2AFV. Notably, WNT5B, SPARC, and MMP2 appear central to facilitating TGF β 's immunosuppressive effects by contributing to immune evasion. Future work should investigate these genes' roles in creating an immunosuppressive tumor microenvironment and their potential as co-targets for immunotherapy. For instance, LGALS1, which encodes Galectin-1, may aid tumor immune evasion by inducing T-cell apoptosis; targeting this pathway alongside LRRC15 could enhance T-cell efficacy.

To confirm the roles of key regulatory genes in the TGF β -LRRC15 pathway, CRISPR-mediated knockout studies targeting LRRC15, MMP2, SPARC, TGF β R2, and WNT5B should be prioritized. Knockouts in TGF β -responsive cancer models will allow us to observe the effects of complete gene disruption, advancing beyond siRNA limitations. Given the observed roles of MMP2 and SPARC in extracellular matrix remodeling, these genes are particularly relevant to understanding TGF β -mediated immune exclusion. Validation studies using CRISPR-engineered cell lines and organoid models may uncover mechanisms through which these genes influence tumor invasiveness, immune cell infiltration, and response to RIT. Similarly, high-throughput CRISPR screens or siRNA libraries targeting these identified proteins may help delineate their functional roles and therapeutic potential in androgen-independent prostate cancer models.

LRRC15-Targeted Radioimmunotherapy in Metastatic Prostate Cancer

Prostate cancer metastases present unique therapeutic challenges in advanced androgen-independent stages, with the most common metastases occurring in lymph node and bone. Bone metastatic lesions, notably enriched in extracellular matrix proteins and factors facilitating tumor-stroma interactions, provide a microenvironment conducive to treatment resistance. Genes like MMP9, WNT5A, and LRRC15 are highly expressed in bone-metastatic androgen-independent prostate cancers, reinforcing the tumor-supportive microenvironment by enhancing matrix remodeling and signaling pathways that promote cell survival and invasion [2].

LRRC15-targeted radioimmunotherapy could target therapeutic resistance in bone metastases, particularly with the most recent Phase I/II clinical trials using Actinium-225 RIT therapeutics [3,4]. Given LRRC15's amplified expression in metastatic prostate cancers of the bone [2], coupling LRRC15-RIT to Actinium-225 could direct radionuclide-induced cytotoxicity to micrometastases, and with the short path length of the radionuclide, minimize damage to surrounding healthy tissue and bone marrow. Preclinical syngeneic models [5] focusing on LRRC15-targeted therapies in bone-metastatic prostate cancer could provide insights into how such treatments affect both the tumor cells and the surrounding stroma, as well as reactivate the immune system. While combined targeting of LRRC15 and TME interactions holds promise, there is a risk that prostate cancer cells may adaptively upregulate compensatory pathways, leading to treatment resistance. For instance, the upregulation of alternative growth or survival pathways such as PI3K/AKT, MAPK, or DNA damage response pathways, could counteract the efficacy of AR inhibitors and RIT [1]. Regular monitoring of pathway activation through biomarkers such as KLK2 and adaptive treatment protocols that modify the therapeutic regimen

based on real-time data could mitigate this risk. Future research could focus on preemptive strategies that anticipate resistance mechanisms, enabling dynamic therapy adjustments in clinical trials. The current clinical trials examining KLK2-targeted therapies [4] in prostate cancer offer a valuable context for testing our findings on the TGF β -LRRC15 axis. In clinical settings, stratifying patients based on LRRC15 and KLK2 expression, and correlating these biomarkers with therapeutic response, could provide a pathway for personalizing treatments for advanced disease.

5.2. References

1. Liu X, Baer JM, Stone ML, et al. Stromal reprogramming overcomes resistance to RAS-MAPK inhibition to improve pancreas cancer responses to cytotoxic and immune therapy. *Science Translational Medicine*. 2024;16(770).
2. Stanbrough M, Bubley GJ, Ross K, et al. Increased Expression of Genes Converting Adrenal Androgens to Testosterone in Androgen-Independent Prostate Cancer. *Cancer Research*. 2006;66(5):2815-2825.
3. Garg R, Allen KJH, Dawicki W, Geoghegan EM, Ludwig DL, Dadachova E. 225Ac-labeled CD33-targeting antibody reverses resistance to Bcl-2 inhibitor venetoclax in acute myeloid leukemia models. *Cancer Med*. 2021;10(3):1128-1140.
4. Morris MJ, Sartor AO, Wong JYC, et al. Phase 1 study of JNJ-69086420, an actinium-225-labeled antibody targeting human kallikrein-2, for advanced prostate cancer. *Journal of Clinical Oncology*. 2022;40(6_suppl):TPS206-TPS206.

5. Simons BW, Kothari V, Benzon B, et al. A mouse model of prostate cancer bone metastasis in a syngeneic immunocompetent host. *Oncotarget*. 2019;10(64):6845-6854.

Published 2019 Dec 3.